

# A First Study of the Structure of the Virtual Photon at HERA.

Martin Lawrence Utley <sup>1</sup>

Department of Physics and Astronomy  
The University of Glasgow  
Glasgow, Scotland

*Thesis submitted for the degree of  
Doctor of Philosophy*

11th October 1996

© M.L. Utley 1996

---

<sup>1</sup>Supported by a Research Studentship from the Particle Physics and Astronomy Research Council, UK.

ProQuest Number: 11007820

All rights reserved

INFORMATION TO ALL USERS

The quality of this reproduction is dependent upon the quality of the copy submitted.

In the unlikely event that the author did not send a complete manuscript and there are missing pages, these will be noted. Also, if material had to be removed, a note will indicate the deletion.



ProQuest 11007820

Published by ProQuest LLC (2018). Copyright of the Dissertation is held by the Author.

All rights reserved.

This work is protected against unauthorized copying under Title 17, United States Code  
Microform Edition © ProQuest LLC.

ProQuest LLC.  
789 East Eisenhower Parkway  
P.O. Box 1346  
Ann Arbor, MI 48106 – 1346

Theris  
10664  
Copy 1

## Abstract

The production of two or more jets of hadrons in photoproduction events at the HERA  $e^+p$  collider has been studied using the ZEUS detector. By tagging the final state positron, two samples of event have been isolated where the photon exchanged between proton and positron is quasi-real (of virtuality  $P^2 \ll 0.02 \text{ GeV}^2$ ) and virtual ( $0.1 < P^2 < 0.55 \text{ GeV}^2$ ) respectively.

It is shown that photons in both  $P^2$  ranges show resolved structure. The  $P^2$  evolution of the structure of the photon is studied by measuring the relative contribution of direct and resolved photon processes to the cross-section for the production of two or more jets. Events have been classified as direct or resolved based upon the value of the final state observable  $x_\gamma^{obs}$ . The data suggest that the contribution from resolved photon processes is suppressed relative to that from direct photon processes as  $P^2$  rises and are in general agreement with leading order calculations. Limited statistics in the data prevent a more quantitative study.

# Preface

There has recently been much theoretical interest in the  $P^2$  evolution of the structure of the photon. Some of this interest has been generated by recent development of the ZEUS detector that has made possible the study of the structure of virtual photons at the HERA electron(positron)-proton collider. This thesis constitutes the first such study. The contribution of resolved photon processes (those where the photon acts as a source of partons) to the cross-section for the production of two or more jets has been measured relative to the contribution from direct photon processes where the entire photon momentum enters the hard scatter. This has been done at two separate photon virtualities.

Chapters 1 and 2 attempt to place this measurement in the context of HERA physics and in the context of past measurements of and the current theoretical understanding of the structure of the photon.

The detector development which enabled this measurement was the installation for the 1994 HERA running period of the ZEUS beam pipe calorimeter (BPC). This device and the other components of the ZEUS detector used for the purposes of this thesis are discussed in Chapter 3.

An account of work done by myself regarding the calibration of the ZEUS TRD chambers is given in chapter 4; the TRD chambers were not used in the measurement presented and the reading of chapter 4 is hence not essential to the understanding of the rest of the thesis.

The Monte Carlo simulation of jet photoproduction events is described in chapter 5. This includes an introduction to the concept of “multiple interactions”

in  $\gamma p$  processes and a brief discussion of the possible effect of photon virtuality on the level of multiple interactions. Also discussed is the use of parametrizations of the structure of the photon in recent leading order calculations relevant to this thesis.

Chapter 6 describes both the online selection of genuine  $ep$  events of interest to those studying jet photoproduction and the criteria applied by myself in order to select the events that have contributed to the measurement presented. My analysis of those events, including the corrections applied to account for the effects of the acceptance, response and resolution of the ZEUS detector, is detailed in chapter 7. The results of this study are discussed in chapter 8 with reference to recent leading order calculations by de Florian *et al.*

These calculations were prompted by the presentation at the European Physical Society conference on high energy physics in Brussels in 1995 of the preliminary and uncorrected results of a parallel and independent study of the data performed by Costas Foudas of the University of Wisconsin. My contribution to the proceedings of that conference constitutes appendix A.

## Acknowledgements

There are a number of people whom I would like to thank for their help, advice and support over the last three years. Foremost are my supervisor Professor David Saxon and Dr Nick Brook. The encouragement and advice that David has supplied over the last year has been essential to the preparation of this thesis; Nick's criticism of my analysis has been equally important. I consider myself very fortunate to have worked with them both.

Drs Bussey, Doyle and Sinclair have also provided many useful comments and much insight for which I am grateful. I am indebted to Daniel de Florian for figure 8.1 and for information regarding his work.

At DESY I have benefitted from working within the Hard Photoproduction

Working Group, particularly from discussions with Jon Butterworth and Costas Foudas. Martin L $\ddot{o}$ ewe's Herculean efforts regarding the 1994 BPC should also be acknowledged.

The Moscow and Bonn groups made me a welcome member of the FDET working group for the duration of my TRD studies. In particular, I would like to thank Stefan, Vladimir and Alexei for their patience in answering my numerous questions.

The efforts of Dave Gilkinson and the rest of the ZEUS offline team are essential to any analysis and should be valued accordingly, as should the efforts of the innumerable physicists and technicians that keep the ZEUS detector and DAQ system ticking over.

The support and encouragement provided by my family and by people in Glasgow, London and at DESY has preserved me this past year. They are too numerous to list. However, I would like to thank Jane, Val, Laurel, Esther and Allan for being superb office mates and for their forbearance. Along with Richard, Robert D, Simon, Fiona, Jason, Drew, Ben, Nick and his family, they have made life in Glasgow and Hamburg largely enjoyable. Susan Ketels and Catherine MacIntyre are two of the finest people I know and I thank them for their endeavours on my behalf.

I would also like to take this opportunity to apologize to anyone with whom I've been curt, brusque or downright rude over the last six months. Before that time I meant it.

Martin Utley

# Contents

<b>1</b>	<b>QCD Processes at HERA</b>	<b>1</b>
1.1	HERA Kinematics . . . . .	2
1.1.1	Kinematic Variables . . . . .	2
1.1.2	Reconstruction of Kinematics . . . . .	4
1.2	Hard Scattering Processes . . . . .	8
1.2.1	Deep Inelastic Scattering . . . . .	8
1.2.2	Jet Photoproduction . . . . .	8
1.2.3	Hard Colour Singlet Exchange . . . . .	11
1.3	Proton Structure . . . . .	14
1.3.1	The Proton Structure Function $F_2$ . . . . .	15
1.3.2	Hadronic Final States . . . . .	16
1.4	Photon Structure . . . . .	17
1.4.1	Direct and Resolved Processes . . . . .	17
1.4.2	$x_\gamma^{obs}$ . . . . .	18
1.4.3	Jet Cross-Sections . . . . .	19
<b>2</b>	<b>Direct and Resolved Processes</b>	<b>20</b>
2.1	Photon Structure Before HERA . . . . .	20
2.1.1	$F_2^\gamma$ . . . . .	20
2.1.2	QED $\rightarrow$ QCD Photon Structure . . . . .	21
2.1.3	Measurements of $F_2^\gamma$ . . . . .	23
2.2	Classification of $\gamma p$ Interactions . . . . .	24
2.2.1	Two Classes of Resolved Photon Process . . . . .	24
2.2.2	Separating “Direct” and “Resolved” Processes . . . . .	25
2.3	The $P^2$ Evolution of Photon Structure . . . . .	28
2.3.1	Existing Data . . . . .	28
2.3.2	A New Kinematic Regime . . . . .	28
2.3.3	Suppression of Resolved Component with $P^2$ . . . . .	29
<b>3</b>	<b>ZEUS Detector</b>	<b>30</b>
3.1	HERA . . . . .	30
3.2	Overview of the ZEUS Detector . . . . .	30
3.3	Calorimeter . . . . .	32

3.3.1	Design . . . . .	32
3.3.2	Response and Resolution . . . . .	34
3.4	Positron Taggers . . . . .	36
3.4.1	LUMI tagger . . . . .	36
3.4.2	Beampipe Calorimeter . . . . .	39
3.5	Central Tracking Detector . . . . .	41
3.5.1	CTD overview . . . . .	41
3.5.2	Vertex Reconstruction . . . . .	42
3.5.3	“Bad-Vertex” Tracks . . . . .	43
<b>4</b>	<b>ZEUS TRD Chambers</b>	<b>45</b>
4.1	The ZEUS Transition Radiation Detectors . . . . .	45
4.2	Mapping the Response of the TRD . . . . .	48
4.2.1	Preliminary Considerations . . . . .	50
4.2.2	Constructing the “Gain Maps” . . . . .	52
4.3	The Effect of the Magnetic Field on TRD Data . . . . .	61
4.4	Conclusions . . . . .	62
<b>5</b>	<b>Event Simulation</b>	<b>65</b>
5.1	Event Generators . . . . .	66
5.2	Predictions Using Models of the Virtual Photon . . . . .	69
5.3	Jet Profiles and Multiple Interactions . . . . .	70
5.3.1	$P^2$ Dependence of MI . . . . .	72
<b>6</b>	<b>Event Selection</b>	<b>76</b>
6.1	The ZEUS Pipeline and Trigger System . . . . .	76
6.1.1	Overview . . . . .	76
6.1.2	Backgrounds to be Removed . . . . .	77
6.1.3	First Level Trigger . . . . .	79
6.1.4	Second Level Trigger . . . . .	80
6.1.5	Third Level Trigger . . . . .	81
6.1.6	Jet Finding - Cone Algorithm . . . . .	81
6.2	Selecting Tagged Hard $\gamma p$ Events . . . . .	83
<b>7</b>	<b>Analysis</b>	<b>89</b>
7.1	The Data . . . . .	89
7.2	Resolutions . . . . .	90
7.3	Jet Profiles . . . . .	98
7.4	$x_\gamma^{obs}$ Distributions . . . . .	100
7.4.1	Preliminary Considerations . . . . .	103
7.5	Bin Purities . . . . .	103
7.6	Correction Techniques . . . . .	106
7.6.1	Migrations from Below $E_T^{jet}$ Cut . . . . .	107
7.6.2	Migrations Across $x_\gamma^{obs}$ Cut . . . . .	107

7.7	$y$ Acceptance . . . . .	110
7.8	The Correction Factors and the Corrected Data . . . . .	110
7.9	Systematic Errors . . . . .	113
<b>8</b>	<b>Interpretation of Results</b>	<b>117</b>
8.1	Leading Order Calculations . . . . .	117
8.2	Conclusions . . . . .	118
<b>A</b>	<b>Contribution to Brussels EPS Conference</b>	<b>121</b>
A.1	Abstract . . . . .	121
A.2	Introduction . . . . .	122
A.3	The Data . . . . .	123
A.4	Results . . . . .	124

# List of Figures

1.1	Diagrams showing processes that are a) leading order in $\alpha_s$ and b) next to leading order in $\alpha_s$ . . . . .	2
1.2	The process $e^\pm p \rightarrow lX$ showing the four-momenta used to define the kinematic variables $x$ , $Q^2$ and $y$ . Note that the forces within the proton prevent the struck quark being observed directly; a system of hadrons is produced in the final state. . . . .	3
1.3	The kinematic regime at HERA in $x$ and $Q^2$ space shown with isolines of $y$ , $E'$ , $E_j$ , $\theta_e$ and $\theta_j$ . . . . .	6
1.4	Isolines of $\theta_e$ and $\theta_j$ superimposed to show the efficacy of the double angle method of reconstructing $x$ and $Q^2$ . . . . .	7
1.5	Neutral current deep inelastic scattering. The hard scale in this process is provided by the virtuality of the exchanged $\gamma$ or $Z$ boson.	9
1.6	A neutral current DIS event. . . . .	9
1.7	Charged current deep inelastic scattering . . . . .	10
1.8	A charged current DIS event. . . . .	10
1.9	The two direct photon processes a) boson gluon fusion and b) QCD Compton. In jet photoproduction, the hard scale is provided by the transverse energy of the two outgoing partons. . . . .	12
1.10	A direct photoproduction candidate seen in the ZEUS detector. . . . .	12
1.11	Two examples of resolved photon processes. . . . .	13
1.12	A resolved photoproduction candidate seen in the ZEUS detector. Note the hadronic activity in the rear (electron direction) region of the detector suggesting a photon remnant. . . . .	13
1.13	An event with a large rapidity gap between jets. The rate of such events suggests the possible exchange of a strongly interacting colour singlet. . . . .	14
1.14	A resolved photon process where a colour singlet is exchanged, leading to a rapidity gap between the two outgoing jets. . . . .	15
2.1	$e\gamma$ DIS showing the four-momenta used to define the kinematic variables $x$ , $y$ and $Q^2$ . . . . .	21

2.2	The scattering of a highly virtual photon off a quasi real target photon showing the QED contribution (a), the QPM contribution (b) and perturbative and non-perturbative QCD contributions (c) and (d) respectively. . . . .	22
2.3	Possible diagrams for the perturbative “anomalous” resolved photon process (a) and the non-perturbative “VMD” resolved photon process (b). . . . .	26
2.4	The similarity of the hadronic final states in (a) LO resolved and (b) NLO direct photoproduction illustrates that the separation of direct and resolved processes is unambiguous only at leading order. . . . .	27
3.1	A longitudinal section of the ZEUS detector. . . . .	32
3.2	A diagram of a ZEUS FCAL module. . . . .	33
3.3	Scatter plots of $\phi_{rec}^{jet}$ vs $\phi_{had}^{jet}$ (left) and $\eta_{rec}^{jet}$ vs $\eta_{had}^{jet}$ (right) in simulated events (see chapter 5) displaying the excellent $\eta$ and $\phi$ resolution of the main ZEUS calorimeter. . . . .	35
3.4	The ZEUS luminosity detector showing the LUMI positron (electron) detector. . . . .	37
3.5	The measurements of $y_e$ of the LUMI tagger and the BPC compared to $y_{jb}$ and, for simulated events, to $y_{tru}$ . . . . .	38
3.6	The position of the BPC relative to the rest of the ZEUS detector. . . . .	39
3.7	The composition of the BPC. . . . .	40
3.8	A comparison of the BPC reconstructed $P^2$ and $P_{tru}^2$ (both in $\text{GeV}^2$ ) for simulated events. . . . .	41
3.9	An octant of the CTD showing the arrangement of wires in “superlayers”. . . . .	43
4.1	A section of a ZEUS TRD chamber viewed from above . . . . .	46
4.2	An end on view of a TRD chamber showing anode wire plane. To bypass the beamhole, the two halves of the wire are connected by a printed circuit board allowing it to be read out from one end only. . . . .	49
4.3	A typical TRD anode pulse showing clusters of ionization. . . . .	49
4.4	The number of wires showing clusters within 1cm of an extrapolated track. Only groups of adjacent wires contribute to bins 2 and 3. . . . .	53
4.5	The distribution of $\Delta$ for adjacent pulses (left) compared to a randomly generated distribution of the same quantity for remote wires (right), chambers one and four. . . . .	54
4.6	Average total charge (avtc) against $y$ bin for each $x$ bin TRD1. . . . .	56
4.7	Average total charge (avtc) against $y$ bin for each $x$ bin TRD2. . . . .	57
4.8	Average total charge (avtc) against $y$ bin for each $x$ bin TRD3. . . . .	58
4.9	Average total charge (avtc) against $y$ bin for each $x$ bin TRD4. . . . .	59
4.10	$\delta\text{avtc}/\delta y$ plotted against $x$ bin for each chamber. . . . .	60

4.11	Diagram showing how the varying $x$ component of the drift velocity of ionization electrons leads to a variation in the “effective length of ionization” and hence the collected total charge over the surface of a TRD chamber. . . . .	63
4.12	The “effective length of ionization” (in mm) against $y$ bin for each $x$ bin calculated for TRD1 using the model described in section 4.3.	64
5.1	A schematic diagram showing distinct stages in the generation of Monte Carlo events. . . . .	67
5.2	$xP(i, x)$ where $i =$ gluon, valence quark, sea quark vs momentum fraction $x$ for the MRSA proton pdf at a $Q^2$ of 25 GeV <sup>2</sup> . . . . .	69
5.3	$xP(i, x)$ where $i =$ gluon, quark vs momentum fraction $x$ for the GRV photon pdf at a $Q^2$ of 25 GeV <sup>2</sup> . . . . .	70
5.4	$xP(i, x)$ where $i =$ gluon or quark vs momentum fraction $x$ for the SAS1D photon pdf at a $Q^2$ of 25 GeV <sup>2</sup> for 3 different photon virtualities. . . . .	71
5.5	In resolved photoproduction events, additional hard scatters can take place between partons from the photon and proton remnants.	72
5.6	The distribution of transverse energy in $\eta\phi$ space for a two jet event.	73
5.7	A representation of the distribution of hadrons within a two jet event in $\eta\phi$ space. The black squares represent the jet centre and the hadrons/cells used to define $\Delta\eta$ and $\Delta\phi$ . The dotted lines show the bands in $\eta$ and $\phi$ within which hadrons/cells contribute to the profile in $\phi$ or $\eta$ respectively. . . . .	74
5.8	Hadron level jet profiles in both a) $\eta$ and b) $\phi$ for events generated by PYTHIA both with (dashed) and without (dotted) multiple interactions. . . . .	75
6.1	A schematic diagram showing the flow of event information through the ZEUS trigger system. For the sake of simplicity, only two subcomponents (CTD and CAL) are shown as contributing to the process. The values on the right hand side of the diagram are approximate rates at which events are processed at that particular stage. . . . .	78
6.2	A schematic diagram of the hard photoproduction trigger filter. Note that each of the SLT branches can contribute to the TLT jet branches labelled “1 jet” and “2 jet”. Higher $E_T^{jet}$ thresholds are applied at $\eta^{jet} > 2$ . . . . .	82
6.3	The $E_T$ distribution of jets within $-1.125 < \eta^{jet} < 1.875$ for LUMI tagged and BPC tagged data before the application of the final analysis cuts. The line shows the cut of 4 GeV applied to $E_T^{jet}$ . . . . .	85

6.4	The distributions of $y_e$ and $y_{jb}$ for both LUMI tagged and BPC tagged data. The lines show the cuts applied to provide the final event sample. . . . .	86
6.5	The distributions of $(t_f - t_r)$ , $(t_u - t_d)$ , $z_{vertex}$ and $2E_e y_{jb} + 2E'_e$ for the combined LUMI tagged and BPC tagged data. Once more, the lines show the cuts applied to provide the final event sample. . . . .	87
6.6	The $P^2$ ( $\text{GeV}^2$ ) distribution of the BPC tagged data before the application of the final analysis cuts. . . . .	88
7.1	The $E_T^{jet}$ and $\eta^{jet}$ distributions for the LUMI tagged and BPC tagged data samples. . . . .	91
7.2	The distributions of $y_e$ and $y_{jb}$ for the data samples tagged by the LUMI and the BPC. . . . .	92
7.3	Scatter plots of $y_{jb}$ vs $y_e$ ((a) and (b)) and the distributions of the quantity $2E_e y_{jb} + 2E'_e$ ((c) and (d)) for both LUMI and BPC data samples. . . . .	93
7.4	The (a) $t_f - t_r$ , (b) $t_u - t_d$ , and (c) $z_{vertex}$ distributions for the final event sample. (d) shows the measured $P^2$ distribution of the BPC tagged data. . . . .	94
7.5	Distributions showing the resolutions of the measurements of $y$ and $P^2$ . Note that energy losses in the calorimeter and losses down the rear beam pipe mean that $y_{jb}$ is systematically lower than $y_{tru}$ . . . . .	96
7.6	The resolutions of measurements of jet quantities: the distance $r$ in $\eta\phi$ space between a hadron level jet and any reconstructed level jet in the same event (a); the (b) $\eta$ , (c) $\phi$ and (d) $E_T$ resolutions of jet measurements. . . . .	97
7.7	The efficiency of matching $E_T > 5$ GeV hadron level jets with $E_T > 4$ GeV reconstructed level jets, as a function of $\eta_{had}^{jet}$ . . . . .	98
7.8	The resolutions for the measurement of $x_\gamma^{obs}$ determined from simulated LUMI and BPC tagged events using $y_{jb}$ (above) and $y_e$ (below) to measure the photon energy $E_\gamma = 2yE_e$ . . . . .	99
7.9	Jet profiles in $\eta$ for both LUMI tagged (solid) and BPC tagged (dotted) events in the kinematic regimes defined by $x_\gamma^{obs} < 0.4$ and $0.4 < x_\gamma^{obs} < 0.75$ . . . . .	101
7.10	LUMI tagged (solid) and BPC tagged (dotted) jet profiles: in $\eta$ for events with $x_\gamma^{obs} > 0.75$ and in $\phi$ for $x_\gamma^{obs} < 0.75$ and $x_\gamma^{obs} > 0.75$ . . . . .	102
7.11	The uncorrected $x_\gamma^{obs}$ distribution for the BPC tagged sample (above) and the LUMI tagged sample (below). . . . .	104
7.12	The uncorrected ratio $N_{res}/N_{dir}$ plotted as a function of $P^2$ ( $\text{GeV}^2$ ) (above) and as a function of $y$ for both LUMI (triangles) and BPC (circles) data (below). In the lower plot it should be mentioned that the error on the LUMI point (obscured by the error bar on the BPC point) is negligible. . . . .	105

7.13	The $E_T^{jet}$ spectrum for events generated as (a) resolved and (b) direct. To show that the resolved sample has a softer $E_T^{jet}$ spectrum, the two have been area normalized and superimposed in (c) where the solid line is the resolved sample and the dashed line is the direct sample. . . . .	108
7.14	The $x_\gamma^{obs}$ distribution for Monte Carlo events where the hadron level and reconstructed level classification of the event as direct or resolved differs (a) and a comparison of the Monte Carlo (histogram) and BPC data $x_\gamma^{obs}$ distributions (b). To compare the shapes of the data and Monte Carlo distributions near the cut of 0.75, the histograms are area normalized in the shaded region. The agreement is adequate to correct the ratio $N_{res}/N_{dir}$ for migrations in $x_\gamma^{obs}$ . . . . .	109
7.15	The ratio of the resolved and direct contributions at: (a) hadron level Monte Carlo, (b) reconstructed level Monte Carlo and (c) in the LUMI tagged data. . . . .	111
7.16	The $y$ distributions for dijet events at hadron level ((a) and (b)). (c) and (d) show the agreement between the reconstructed level Monte Carlo (shaded histogram) and the data points for both LUMI tagged and BPC tagged. The data and Monte Carlo presented in figures (c) and (d) are area normalized. . . . .	112
7.17	The corrected ratio of the resolved and direct contributions to the dijet cross-section as determined by a cut at 0.75 on the quantity $x_\gamma^{obs}$ as a function of the photon virtuality $P^2$ ( $\text{GeV}^2$ ). The vertical error bars show the statistical errors (inner) and the statistical and systematic errors added in quadrature (outer). . . . .	114
7.18	The systematic errors on the corrected result introduced by the choice of cuts applied to the data and reconstructed level Monte Carlo for real photons (above) and virtual photons (below). The continuous lines show the statistical errors associated with the central values of the corrected results. . . . .	116
8.1	The corrected results obtained for this thesis compared to LO calculations by de Florian <i>et al.</i> using four different parametrizations of the structure of the virtual photon (see text). . . . .	119
A.1	Diagrams showing a) direct and b) resolved photon processes. In both cases the photon of virtuality $P^2$ carries a fraction $y$ of the positron momentum. . . . .	123
A.2	Uncorrected $x_\gamma^{obs}$ distributions for a) virtual and b) quasi-real photons	125
A.3	The uncorrected ratio $N_{res}/N_{dir}$ as a function of photon virtuality $P^2$ ( $\text{GeV}^2$ ) . . . . .	126

# Chapter 1

## QCD Processes at HERA

The HERA electron - proton collider is an ideal place to study many aspects of Quantum Chromo-Dynamics (QCD), the theory of the “strong” force that binds the quarks in the proton.

The strong coupling constant,  $\alpha_s$ , that determines the strength of the  $q \rightarrow qg$  process (see figure 1.1 (a) ) decreases with the energy, or scale, at which the process occurs [1]. Diagrams with one large energy, or hard, low  $\alpha_s$  interaction are said to be leading order processes. Calculations within perturbative QCD rely on the contributions from higher order processes with many hard interactions (figure 1.1 (b)) being smaller than those from leading order processes. This condition requires a low value of  $\alpha_s$  and hence requires a hard scale to be present in the interaction. In multi-legged Feynman diagrams such as those shown in figure 1.9, the hard scale can come from a variety of sources; the hard scale can be provided by the virtuality of the photon, the transverse momentum of the propagator or by the masses or transverse momenta of the outgoing quarks.

This chapter describes the kinematic regime at HERA and discusses some of the hard processes through which QCD can be tested with particular reference to the structure of both the proton and the photon.

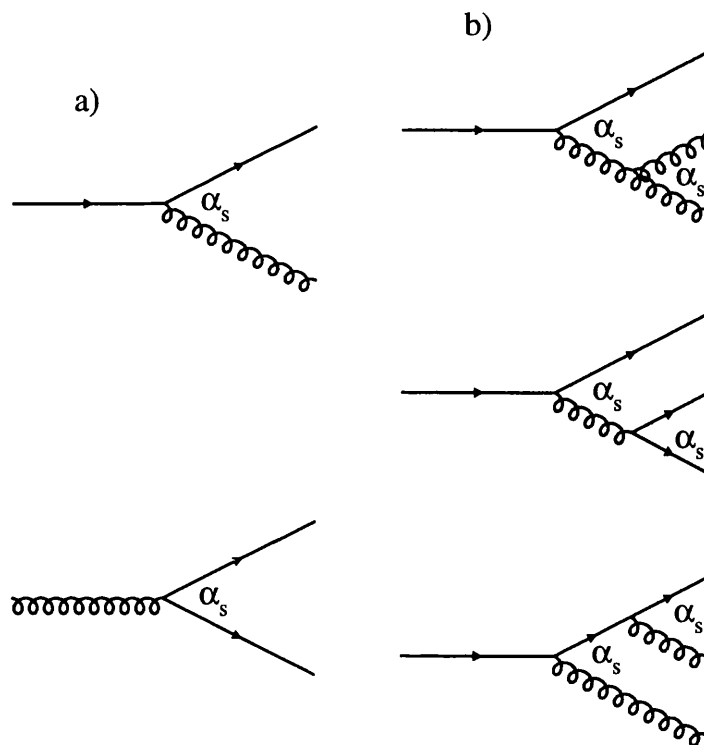


Figure 1.1: Diagrams showing processes that are a) leading order in  $\alpha_s$ , and b) next to leading order in  $\alpha_s$ .

## 1.1 HERA Kinematics

### 1.1.1 Kinematic Variables

During the 1994 running period the HERA accelerator at DESY in Hamburg collided 27.5 GeV positrons with 820.0 GeV protons. and  $E_e$  being the two beam energies. The kinematic variables commonly used to describe the interaction  $e^\pm p \rightarrow lX$  are the Bjorken scaling variables  $x$  and  $y$  and the squared momentum transfer  $Q^2$ . In terms of the four-momenta  $k$  and  $k'$  of the incoming and outgoing electron,  $Q^2$  is given by equation 1.1,  $q$  being the four-momentum of the exchanged boson.

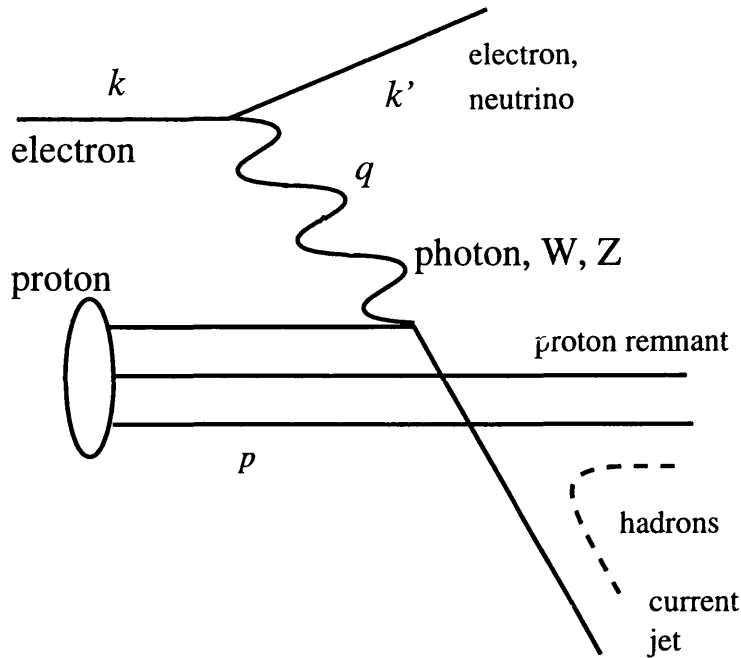


Figure 1.2: The process  $e^\pm p \rightarrow lX$  showing the four-momenta used to define the kinematic variables  $x$ ,  $Q^2$  and  $y$ . Note that the forces within the proton prevent the struck quark being observed directly; a system of hadrons is produced in the final state.

$$Q^2 = -q^2 = -(k - k')^2 \quad (1.1)$$

$Q^2$  can be thought of as the negative mass squared, or the virtuality, of the exchanged boson. At HERA,  $Q^2$  varies by over ten orders of magnitude from  $10^5$  to  $10^{-5}$   $\text{GeV}^2$ . The total  $e^\pm p$  cross-section is proportional to  $1/Q^4$  and hence is dominated by photoproduction events where the interaction proceeds via the exchange of quasi-real  $Q^2 \approx 0$  photons.

Bjorken  $x$  and  $y$  are defined by equations 1.2 and 1.3 respectively, where  $p$  is the incoming proton four-momentum. In the limit of massless partons,  $x$  can be considered as the fraction of the proton momentum carried by the struck parton;  $y$  is the fraction of the electron energy carried by the exchanged boson in the proton rest frame and in any frame where the photon and the electron are collinear, *ie* in photoproduction.

$$x = \frac{Q^2}{2p \cdot q} \quad (1.2)$$

$$y = \frac{p \cdot q}{p \cdot k} \quad (1.3)$$

These variables are related through the expression for the electron-proton centre of mass energy  $s$  shown in equation 1.4 where, in the last step, the assumption is made that the masses of the proton and electron can be ignored.

$$s = (p + k)^2 = 2p \cdot k + m_p^2 + m_e^2 = \frac{Q^2}{xy} + m_p^2 + m_e^2 \approx \frac{Q^2}{xy} \quad (1.4)$$

### 1.1.2 Reconstruction of Kinematics

The reconstruction of the kinematic variables defined in the foregoing is essential for any analysis of HERA physics. Three methods are used for this reconstruction. One can use information from the scattered positron (electron) alone, from the hadronic final state alone or from a mixture of the two. Using the scattered electron energy  $E'_e$  and the scattered electron angle  $\theta_e$ , defined with respect to the initial proton direction,  $y$ ,  $Q^2$  and  $x$  are given by equations 1.5 to 1.7.

$$y_e = 1 - \frac{E'_e}{E_e}(1 - \cos \theta_e) \quad (1.5)$$

$$Q_e^2 = 2E_e E'_e (1 + \cos \theta_e) \quad (1.6)$$

$$x_e = \frac{E_e E'_e (1 + \cos \theta_e)}{P(2E_e - E'_e(1 - \cos \theta_e))} \quad (1.7)$$

The strong forces within the proton prevent the struck quark from being observed directly; a hadronic system is produced in the final state, labelled the current jet. To reconstruct the event kinematics from the hadronic final state, an angle  $\theta_j$  is attributed to the current jet. This is calculated using an energy

weighted algorithm that minimizes the contribution from the proton remnant, the hadrons resulting from the partons in the proton which did not participate in the hard scatter. The expressions for  $x$  and  $Q^2$  and  $y$  using final state hadrons ( $i$ ) associated with the struck parton are shown in equations 1.10 to 1.8.

$$y_{jb} = \frac{\sum_i (E - p_z)}{2E_e} \quad (1.8)$$

$$Q_{jb}^2 = \frac{(\sum_i p_x)^2 + (\sum_i p_y)^2}{1 - y_{jb}} \quad (1.9)$$

$$x_{jb} = \frac{Q_{jb}^2}{sy_{jb}} \quad (1.10)$$

Figure 1.3 presents graphs of  $Q^2$  vs  $x$  showing isolines of the measurable quantities  $E'_e$ ,  $\theta_e$ ,  $E_j$  and  $\theta_j$ . It can be seen that for large regions of  $Q^2x$  space, particularly near the kinematic peak  $E'_e \approx E_e$ , small errors in the measurement of  $E'_e$  or  $E'_j$  can lead to large uncertainty in the reconstruction of  $x$  and  $Q^2$ . Due to this fact, a reconstruction method utilizing the two angular variables  $\theta_e$  and  $\theta_j$  is commonly used. Figure 1.4 shows a graph of  $Q^2$  vs  $x$  with isolines of both  $\theta_e$  and  $\theta_j$  superimposed. The density of the isolines and the large angles at which the lines intersect make this combination of variables particularly useful. This “double angle” method gives the expressions shown in equations 1.13 to 1.11.

$$y_{DA} = \frac{\sin \theta_e (1 - \cos \theta_j)}{\sin \theta_j + \sin \theta_e - \sin(\theta_e + \theta_j)} \quad (1.11)$$

$$Q_{DA}^2 = 4E_e^2 \frac{\sin \theta_j (1 + \cos \theta_e)}{\sin \theta_j + \sin \theta_e - \sin(\theta_e + \theta_j)} \quad (1.12)$$

$$x = \frac{Q_{DA}^2}{sy_{DA}} \quad (1.13)$$

Two other variables useful in describing HERA physics are pseudorapidity  $\eta = -\ln(\tan(\theta/2))$  and azimuth  $\phi$ .

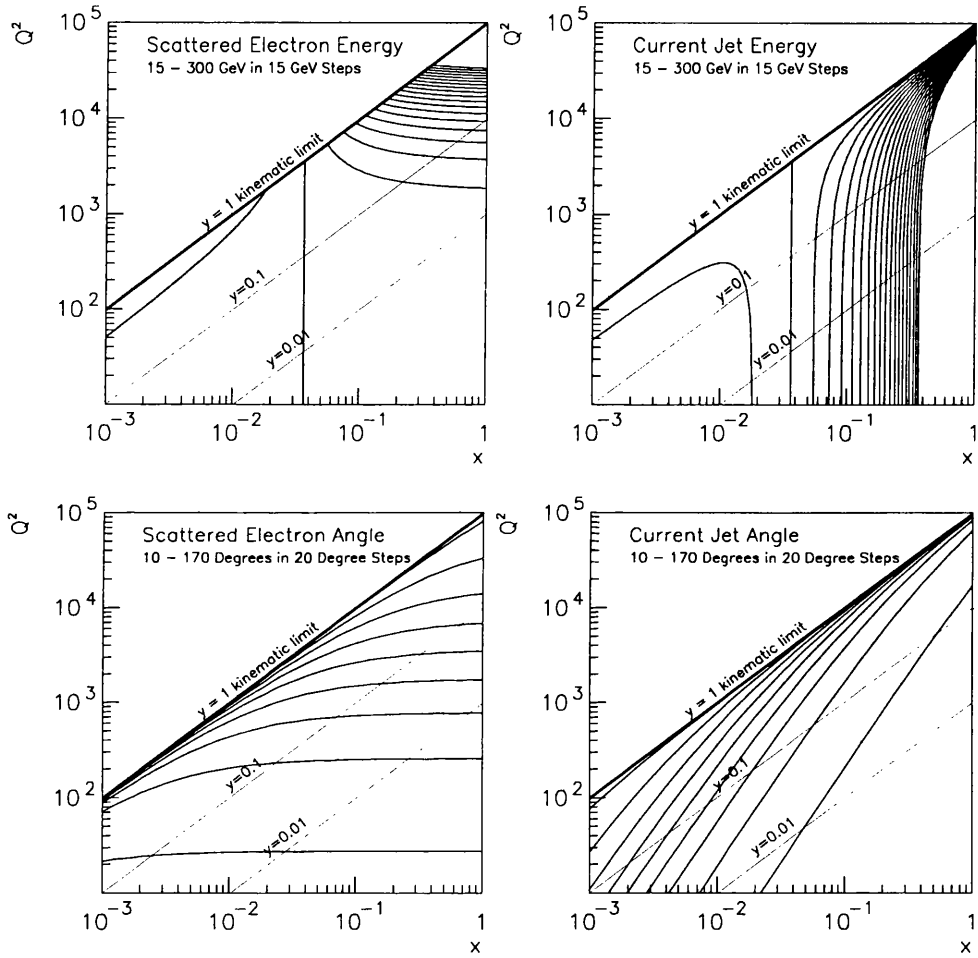


Figure 1.3: The kinematic regime at HERA in  $x$  and  $Q^2$  space shown with isolines of  $y$ ,  $E'$ ,  $E_j$ ,  $\theta_e$  and  $\theta_j$ .

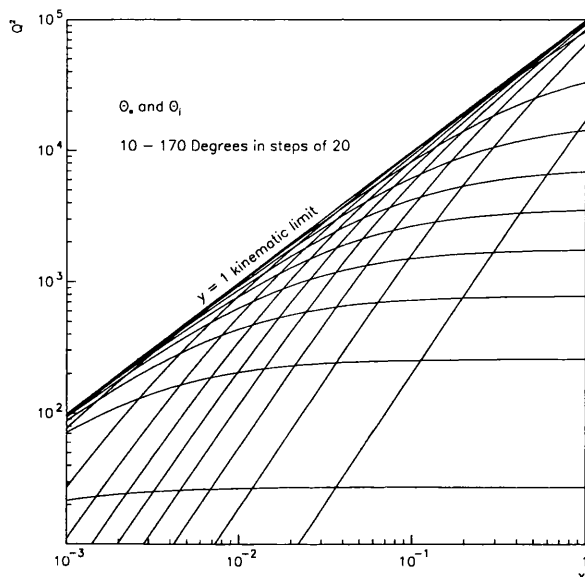


Figure 1.4: Isolines of  $\theta_e$  and  $\theta_j$  superimposed to show the efficacy of the double angle method of reconstructing  $x$  and  $Q^2$ .

Many distinct physical processes contribute to the total cross-section at HERA. The relative contribution of each process varies over the kinematic region represented in figure 1.3 and defined by equation 1.14.

$$\frac{Q^2}{x} \leq 4E_p E_e \leq 90200 \text{GeV}^2 \quad (1.14)$$

The focus of this thesis is on the transitional region between “high  $Q^2$ ” deep inelastic scattering processes and photoproduction processes where the exchanged photon virtuality is low, with particular reference to the changing behaviour of the virtual photon. There follows a short discussion of some of the processes at HERA that have a hard scale through which various aspects of QCD can be tested.

## 1.2 Hard Scattering Processes

### 1.2.1 Deep Inelastic Scattering

In deep inelastic scattering the hard scale is provided by the virtuality of the exchanged boson. The exchanged boson is typically a virtual photon but at very high  $Q^2$  ( $> M_{Z,W}^2$ ) there is a contribution from  $Z^0$  and  $W^\pm$  exchange. Feynman graphs for neutral current (NC) and charged current (CC) deep inelastic scattering are shown in figures 1.5 and 1.7.

Figures 1.6 and 1.8 show how these processes manifest themselves in the ZEUS detector. Figure 1.6 shows an NC DIS event with a 12.0 GeV electron detected in the main calorimeter. The electron deposit is labelled in the section along the beamline (right of figure 1.6). In such “event displays” the proton travels from right to left. The proton remnant is identified as the energy deposits in the forward (proton direction) region of the detector. The end-on view of this event (left of figure 1.6) shows the scattered electron balanced in energy transverse to the beam line by the spray of hadrons that constitutes the current jet. This balance of transverse energy ( $E_T$ ) is not present in the event shown in figure 1.8. Such events are candidates for CC DIS where the missing  $E_T$  is carried by the final state neutrino. Again the section along the beamline shows the forward energy deposits associated with the proton remnant.

A more detailed discussion of deep inelastic scattering is presented in section 1.3.

### 1.2.2 Jet Photoproduction

Events where the exchanged photon is almost real are labelled photoproduction events. A subsample of these events are characterized by the production of jets of hadrons with considerable momentum transverse to the incoming beams, suggesting a hard parton-parton scattering process. There are several possible

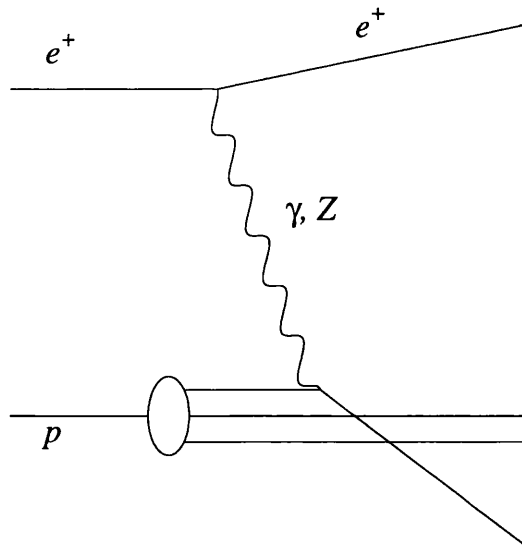


Figure 1.5: Neutral current deep inelastic scattering. The hard scale in this process is provided by the virtuality of the exchanged  $\gamma$  or  $Z$  boson.

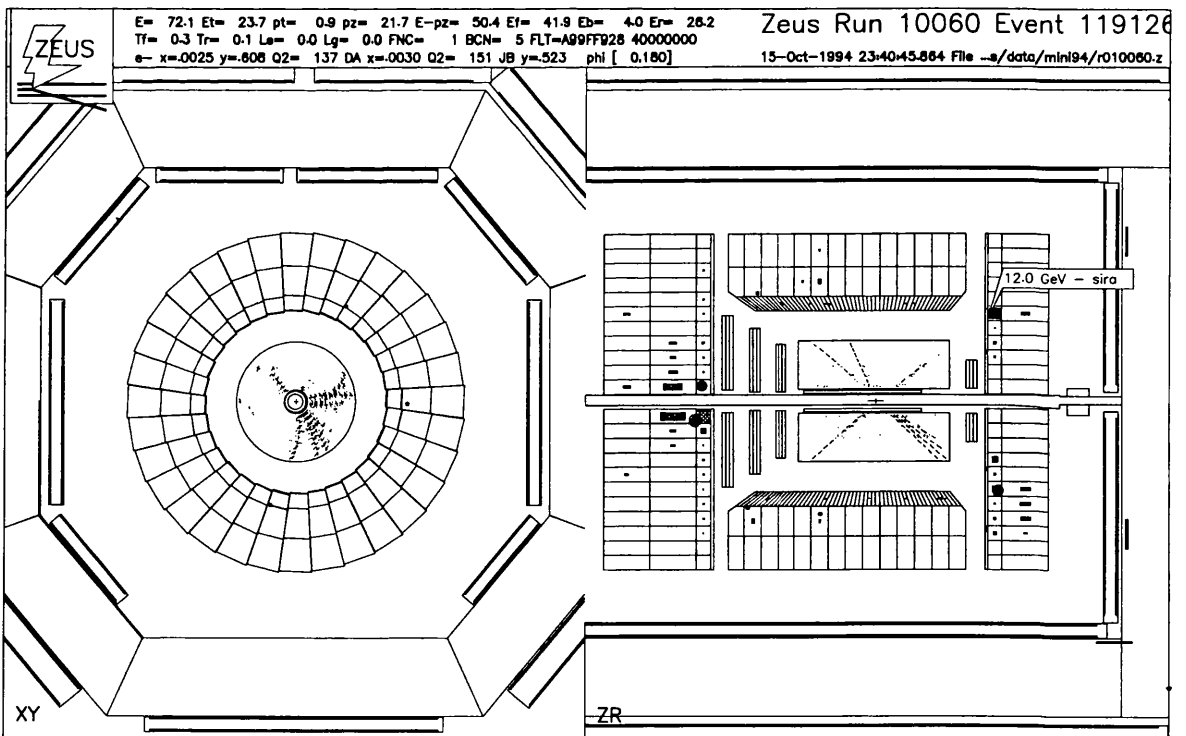


Figure 1.6: A neutral current DIS event.

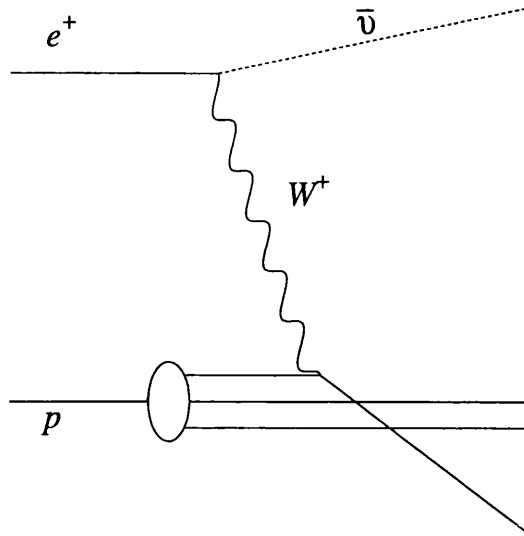


Figure 1.7: Charged current deep inelastic scattering

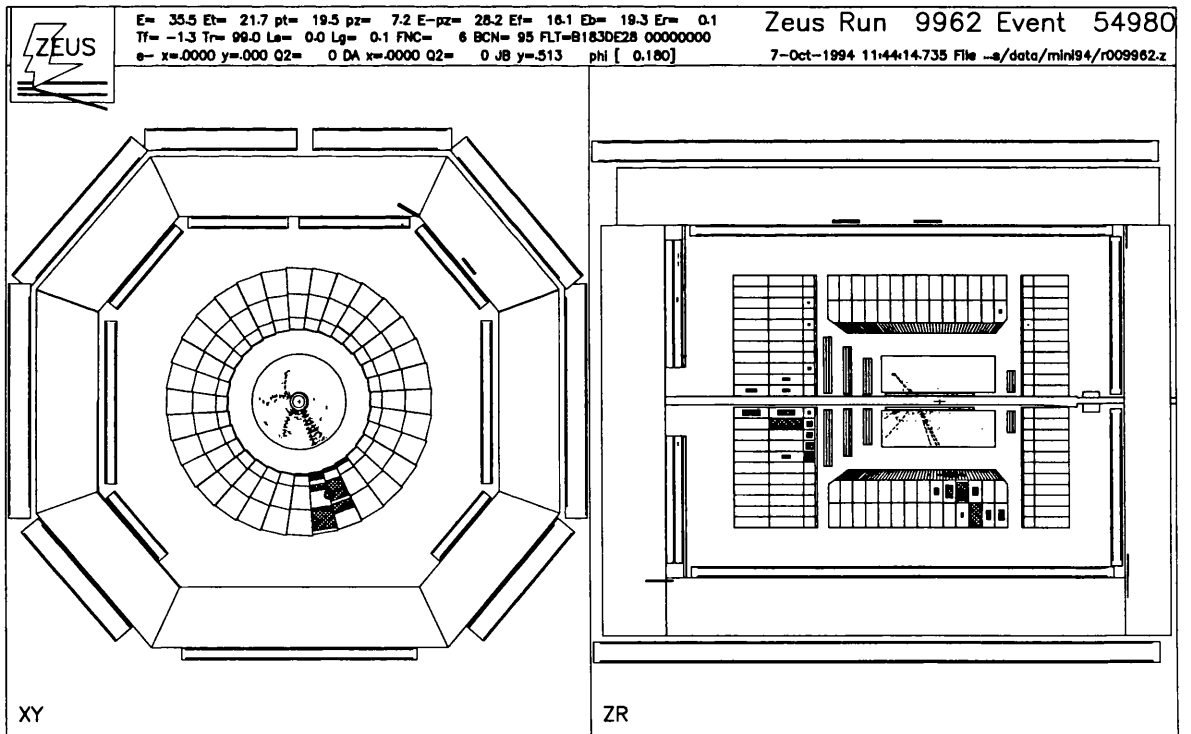


Figure 1.8: A charged current DIS event.

mechanisms for jet photoproduction. Figure 1.9 (a) shows a gluon producing a  $q\bar{q}$  pair with large transverse momentum, one of which subsequently scatters off the photon. This is referred to as boson gluon fusion (BGF). The photon can alternatively be absorbed by a quark or anti-quark which then emits a gluon with large transverse energy (see figure 1.9 (b)). In analogy to the similar process in Quantum Electro-Dynamics (QED), this mechanism is labelled QCD Compton. Both BGF and QCD Compton processes involve the whole photon momentum entering the hard scatter and are said to be “direct” photon processes. Figure 1.10 shows a candidate for a direct photoproduction event. The two jets are produced back to back in azimuth as shown by the end-on section and in the  $E_T$  weighted distribution of energy deposits in  $\eta\phi$  space (the “lego plot” to the left of figure 1.10).

A further set of processes entails the photon acting as a source of partons, one of which takes part in a hard scatter with a parton from the proton. Possible diagrams of such “resolved” photon processes are shown in figure 1.11. In addition to the proton remnant there are energy deposits in the rear ( $-\eta$ , electron direction) region of the detector which can be attributed to the photon remnant. A candidate resolved event is shown in figure 1.12.

### 1.2.3 Hard Colour Singlet Exchange

A subsample of jet photoproduction events are characterized by a lack of hadronic activity between jets separated in pseudorapidity  $\eta$ . These events are said to have a rapidity gap between the jets. Such an event is shown in figure 1.13, there being little hadronic activity between  $\eta = 1.5$  and  $\eta = -1$ . QCD predicts the differential cross-section for events with a rapidity gap of  $\Delta\eta$  to decrease exponentially with  $\Delta\eta$ . Contrary to this expectation, the measured cross-section has a plateau at large values of  $\Delta\eta$ . A plateau is expected from the exchange of  $\gamma$  or  $Z$  particles but the contribution of these processes is expected to apply at a much smaller

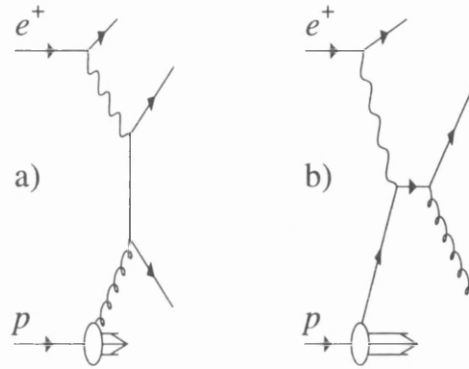


Figure 1.9: The two direct photon processes a) boson gluon fusion and b) QCD Compton. In jet photoproduction, the hard scale is provided by the transverse energy of the two outgoing partons.

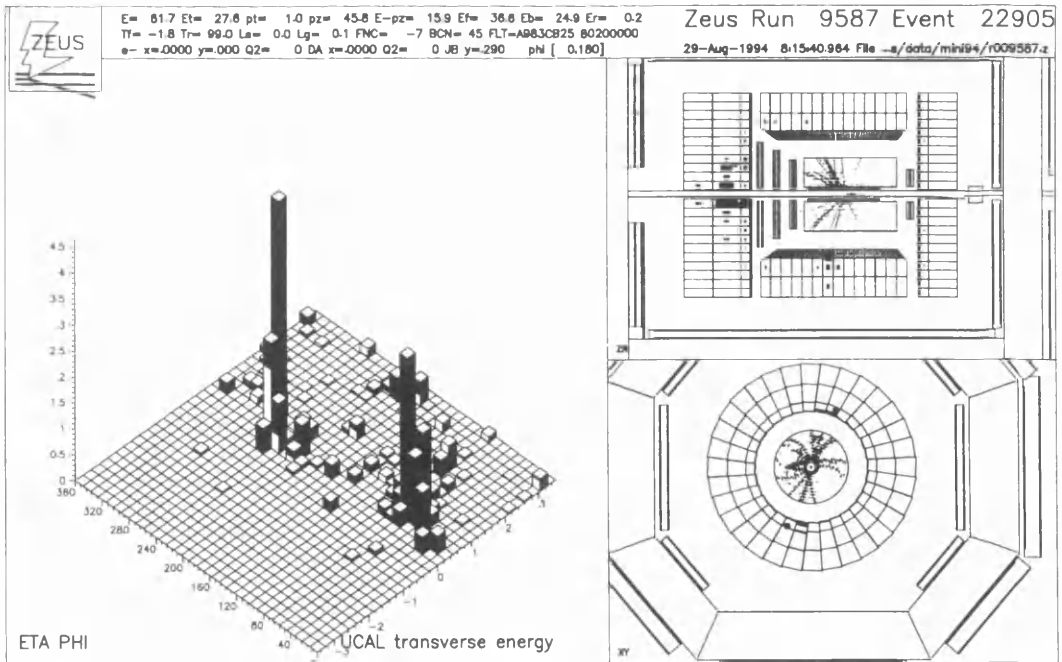


Figure 1.10: A direct photoproduction candidate seen in the ZEUS detector.

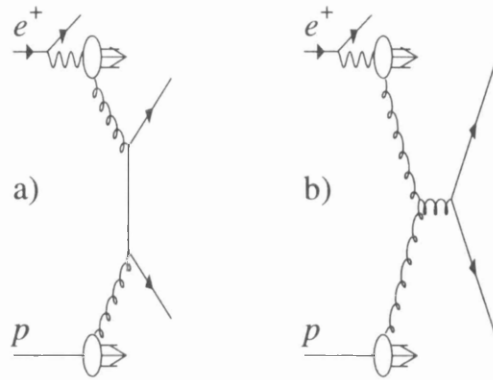


Figure 1.11: Two examples of resolved photon processes.

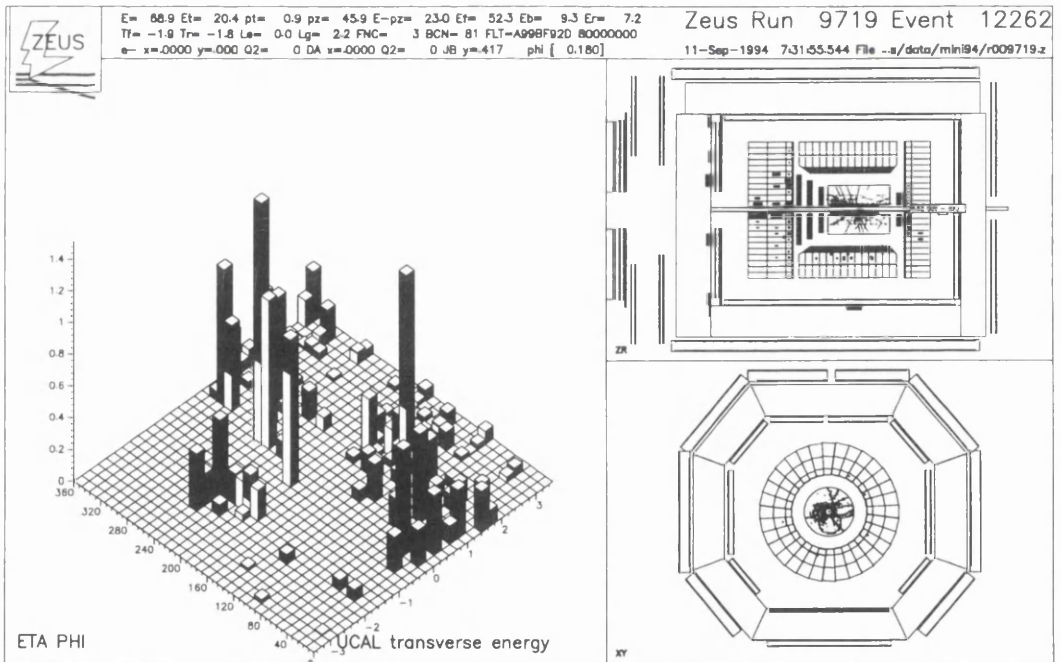


Figure 1.12: A resolved photoproduction candidate seen in the ZEUS detector. Note the hadronic activity in the rear (electron direction) region of the detector suggesting a photon remnant.

value of the cross-section than the plateau seen in the data. This result can be explained by models incorporating the possible exchange of a strongly interacting colour singlet, the phenomenological Pomeron (see figure 1.14).

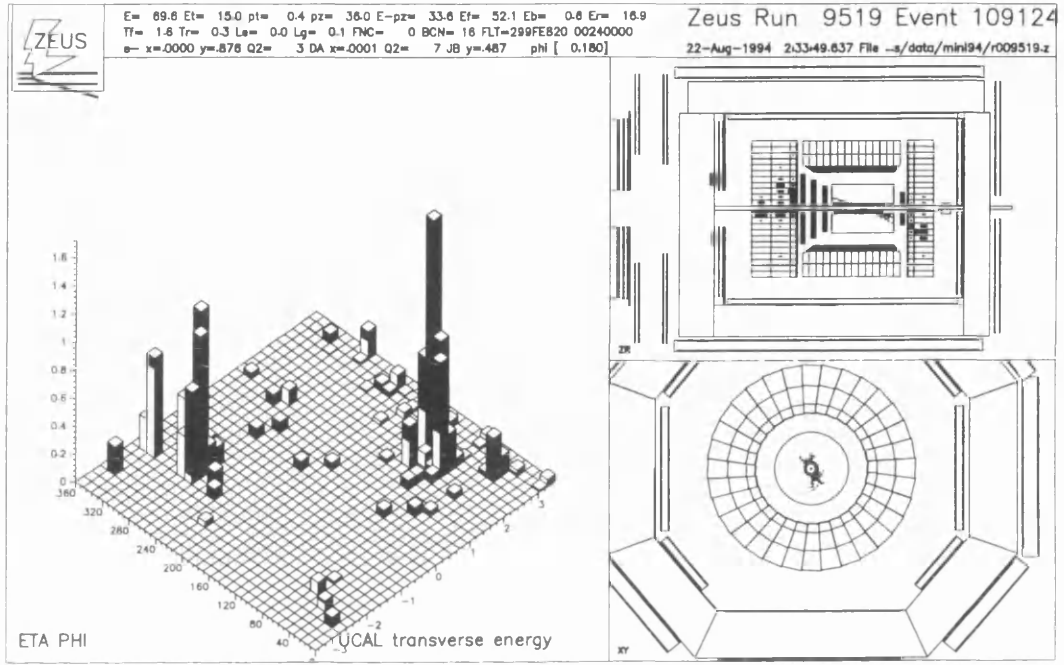


Figure 1.13: An event with a large rapidity gap between jets. The rate of such events suggests the possible exchange of a strongly interacting colour singlet.

### 1.3 Proton Structure

HERA probes the structure of the proton through (among others) the process of deep inelastic  $e^\pm p$  scattering (DIS). DIS experiments had a major role in the development of QCD. DIS experiments at SLAC [2] first showed the proton to be constituted of the charged point-like partons now accepted as quarks and also provided indirect evidence for the existence of the gluon.

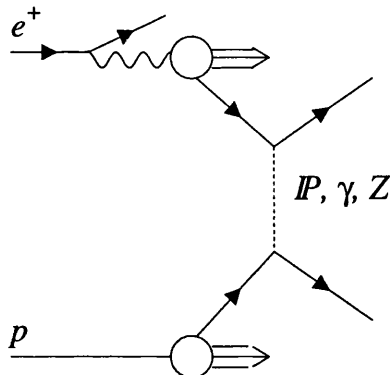


Figure 1.14: A resolved photon process where a colour singlet is exchanged, leading to a rapidity gap between the two outgoing jets.

### 1.3.1 The Proton Structure Function $F_2$

In DIS the virtual photon strikes a charged parton in the proton, causing the proton to break up (see figure 1.2). By measuring the properties of the produced hadronic system and the scattered electron one can reconstruct the kinematic variables  $x$ ,  $Q^2$  and  $y$  as discussed in section 1.1. The differential  $e^\pm p$  cross-section can then be expressed in terms of two separate functions of  $x$  and  $Q^2$ , the proton structure functions  $F_2$  and  $F_L$  [3], as shown in equation 1.15.

$$\frac{d^2\sigma}{dx dQ^2} = \frac{2\pi\alpha^2}{xQ^4} [(1 + (1 - y)^2)F_2(x, Q^2) - y^2 F_L(x, Q^2)] \quad (1.15)$$

A physical interpretation of  $F_2$  is provided by the quark parton model (QPM) [4]. The QPM views the proton as being constituted of three non-interacting valence quarks. DIS is then the scattering of the electron off a free quark. The  $e^\pm p$  cross-section can hence be written as the incoherent sum of the individual electron-quark scattering probabilities [5] as in equation 1.16

$$\frac{d^2\sigma}{dx dQ^2} = \sum_q \int_0^1 dx f_q(x) \left( \frac{d^2\sigma}{dx dQ^2} \right)_{eq} \quad (1.16)$$

where  $f_q(x)$  is the probability of the quark  $q$  carrying a fraction  $x$  of the proton momentum.

This leads to the QPM prediction for  $F_2$  [5] given in equation 1.17.

$$F_2(x) = \sum_q e_q^2 x f_q(x) \quad (1.17)$$

If the QPM were to be correct in its assumption that the proton is constituted wholly of quarks, one would expect the fraction of the proton momentum carried by charged partons to be equal to unity, i.e.  $\int dx F_2(x) = 1$ . Measurements show that contrary to this expectation  $\int dx F_2(x) \approx 0.5$  [2]. In QCD the remainder of the proton momentum is thought to be carried by gluons, the electrically neutral mediators of the strong force that binds the quarks in the proton.

From equation 1.17 one can see that the QPM predicts  $F_2$  to have no  $Q^2$  dependence, a phenomenon known as scaling [6]. In QCD, the struck quark can emit a gluon before interacting with the photon. This possibility and the presence of the subsequent  $g \rightarrow q\bar{q}$  splitting introduce a  $Q^2$  dependence to  $F_2$ ;  $Q^2$  is related to the resolving power of the photon and as  $Q^2$  increases the photon can resolve more  $q\bar{q}$  pairs, leading to an increase in  $F_2$ .

$f_q(x)$  in the QPM becomes  $f_q(x, Q^2)$  in QCD, the renormalized parton density function [5]. QCD describes the  $g \rightarrow q\bar{q}$  splitting and can predict the  $Q^2$  behaviour, or evolution, of  $f_q(x, Q^2)$  but requires a starting distribution  $f_q(x, Q_0)$  which can be obtained from fits to existing data [7][8][9]. Measurements of  $F_2$  [10][11] at different values of  $Q^2$  hence provide a useful test of QCD predictions.

### 1.3.2 Hadronic Final States

Other measurements within the deep inelastic scattering kinematic regime can act as useful tests of the nature of QCD. Recent studies have investigated whether

QCD coherence effects are observable at HERA. QCD coherence affects the way in which the struck parton evolves into the observed hadronic final state [12]; in QCD models that incorporate coherence, the emission of gluons at large angles is suppressed. The Breit frame is the ideal place to look for these effects. The Breit frame is defined as the frame in which the exchanged boson is entirely spacelike and in which the struck quark is scattered through 180 degrees. If one boosts to the Breit frame it is possible to separate the current fragmentation region, the hadronic system associated with the struck parton, from that associated with the incoming parton, labelled the target fragmentation region. Measurements of the charged particle multiplicity at many different values of  $Q^2$  have been shown to be sensitive to QCD coherence effects in the current region and favour coherent models [13][14]. This set of measurements illustrates the ability of HERA to investigate the structure of QCD by studying scale dependence. Other such illustrations are measurements of  $\alpha_s$  as a function of  $Q^2$  [15][16][17].

## 1.4 Photon Structure

### 1.4.1 Direct and Resolved Processes

HERA can also probe the structure of the photon. Although having no intrinsic structure, the photon can fluctuate into a quark-antiquark pair with a lifetime bound by the uncertainty principle. The  $q\bar{q}$  state can then evolve via gluon emission into a more complicated, hadron-like object. There are subsequently processes where a quark or a gluon carrying a fraction of the photon momentum participates in a hard scatter with a parton from the proton. In LO QCD these resolved photon processes can be separated from direct photon processes, where the full photon momentum participates in the hard scatter. The BGF and QCD Compton processes shown in figure 1.9 are direct photon processes; resolved photon processes are shown in figure 1.11. In resolved processes there is, in

addition to the proton remnant, a remnant associated with the photon.

At sufficiently high photon virtuality  $Q^2$  the photon acts as a point-like probe, ie there is no contribution to the  $\gamma^*p$  cross-section from resolved photon processes. However, for events with photons of low virtuality, photoproduction events, both classes of process contribute.

### 1.4.2 $x_\gamma^{obs}$

Both resolved and direct events are characterized by having two outgoing partons of large transverse energy (see figures 1.9 and 1.11). These can manifest themselves as jets of hadrons in the final state as shown in figures 1.10 and 1.12. Studying hard photoproduction events, those where jets of hadrons are produced, has two main virtues. Firstly, the cross-sections for these processes can be calculated using perturbative QCD due to the hard scale provided by the  $E_T$  of the jets. Secondly, by associating the two jets of highest transverse energy with the outgoing partons, one can reconstruct the fraction of the photon momentum, labelled  $x_\gamma$  in analogy to Bjorken  $x$ , that went into the hard scatter and thereby make an attempt to separate the two classes of event. At low virtualities, the photon travels in the  $-z$  direction and carries an  $E - p_z = E(1 - \cos\theta) = 2E_\gamma$  into the  $\gamma p$  interaction; the proton travels in the  $+z$  direction and carries an  $E - p_z = 0$  into the  $\gamma p$  interaction. By measuring the  $E - p_z$  carried by the two outgoing jets one can hence measure the fraction of the photon energy that has gone into the production of these jets.

The quantity  $x_\gamma^{obs}$ , defined by equation 1.18, is the fraction of the photon momentum manifest in the two highest  $E_T$  jets.

$$x_\gamma^{obs} = \frac{\sum_{j=1}^2 E_{Tj} e^{-\eta_j}}{2Ey} \approx \frac{\sum_{j=1}^2 E_j - p_{zj}}{\sum_{hadrons} E - p_z} \quad (1.18)$$

Events with high  $x_\gamma^{obs}$  are associated with direct processes whilst events with low  $x_\gamma^{obs}$  are associated with resolved processes. The measured  $x_\gamma^{obs}$  distribution

shows a clear peak at high values and is inexplicable without invoking both direct and resolved photon processes [18].

### 1.4.3 Jet Cross-Sections

The expression for any jet cross-section can be factorized into two terms as shown in equation 1.19, one pertaining to the hard parton-parton scattering cross-sections,  $\hat{\sigma}$  at the hard scale  $Q^2$ , and one accounting for the parton distribution functions (pdf's) of the incoming beam particles,  $f_{\gamma/e}$ ,  $f_\gamma(x_\gamma, Q^2)$  and  $f_p(x_p, Q^2)$ .

$$\frac{d\sigma_{jet}}{dx_\gamma dx_p dy dp_T} = [f_{\gamma/e}(y) f_\gamma(x_\gamma, Q^2) f_p(x_p, Q^2)] \times \left[ \frac{d\hat{\sigma}}{dp_T} \right] \quad (1.19)$$

By choosing kinematic regimes for which either the parton dynamics or the pdf's are well constrained, one can test and extend our knowledge of the other.

Jet photoproduction cross-sections have indeed been shown to be sensitive to the parton distributions within both the proton and the photon [19][20][21]. The contribution from processes such as those shown in figures 1.9 (a) and 1.11 (b) means that jet photoproduction can probe directly the gluon content of the proton and photon; these measurements are hence complementary to those of  $F_2^p$  and the photon structure function  $F_2^\gamma$  (see chapter 2) as these probe only the quark content of the respective targets.

The sensitivity of jet photoproduction to parton dynamics has also been established. Resolved photoproduction processes are dominated by those with gluon propagators whereas direct photoproduction processes have a quark propagator. Comparison of the angular distributions of jets within samples of events classified as direct or resolved by means of a cut on  $x_\gamma^{obs}$  confirmed expectations based on the differing spins of the quark and gluon [22].

# Chapter 2

## Direct and Resolved Processes

### 2.1 Photon Structure Before HERA

#### 2.1.1 $F_2^\gamma$

Deep inelastic scattering of an electron off a photon target can be treated in a similar fashion to the deep inelastic scattering of an electron off a proton. Figure 2.1 shows the process  $e\gamma \rightarrow eX$ .

As with  $e^\pm p$  scattering the probing photon virtuality  $Q^2$  and the Bjorken scaling variables  $x$  and  $y$  are defined by equations 2.1 to 2.3 cf equations 1.1 to 1.3.

$$Q^2 = -q^2 = -(k - k')^2 \quad (2.1)$$

$$x = \frac{Q^2}{2p \cdot q} \quad (2.2)$$

$$y = \frac{p \cdot q}{p \cdot k} \quad (2.3)$$

Note that  $p$  is the four-momentum of the target photon. The differential cross-section is again written in terms of two separate functions of  $x$  and  $Q^2$ ,

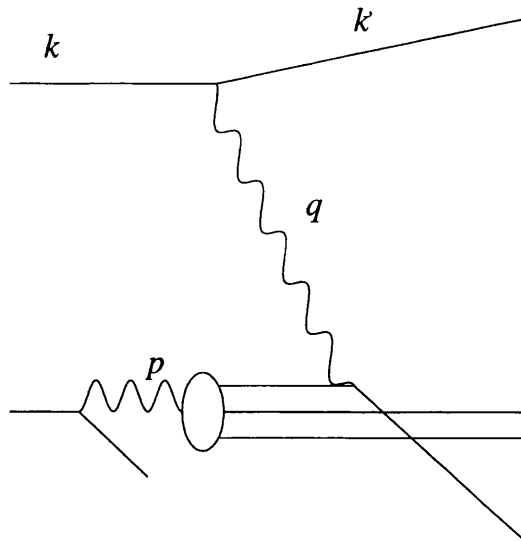


Figure 2.1:  $e\gamma$  DIS showing the four-momenta used to define the kinematic variables  $x$ ,  $y$  and  $Q^2$ .

the photon structure functions  $F_2^\gamma$  and  $F_L^\gamma$ , as shown in equation 2.4.  $F_L$  is the contribution from longitudinally polarized probing photons; virtual photons have longitudinal polarization states in addition to the transverse states allowed for massless real photons [23].

$$\frac{d^2\sigma}{dx dQ^2} = \frac{2\pi\alpha^2}{xQ^4} [(1 + (1 - y)^2)F_2^\gamma(x, Q^2) - y^2 F_L^\gamma(x, Q^2)] \quad (2.4)$$

### 2.1.2 QED $\rightarrow$ QCD Photon Structure

The process  $e\gamma \rightarrow e + l^+l^-$ , where  $l$  is a lepton, shown in figure 2.2 (a) is well understood and is calculable within QED. The dominant term for  $F_2^{\gamma, QED}$  is shown in equation 2.5 (for a more thorough treatment see [24]). There is good agreement between the predictions and measured values of  $F_2^{\gamma, QED}$  [25].

$$F_2^{\gamma, QED} = \sum_l e_l^4 \frac{\alpha}{\pi} x_\gamma [x_\gamma^2 + (1 - x_\gamma)^2] \ln \frac{Q^2}{m_l^2} \quad (2.5)$$

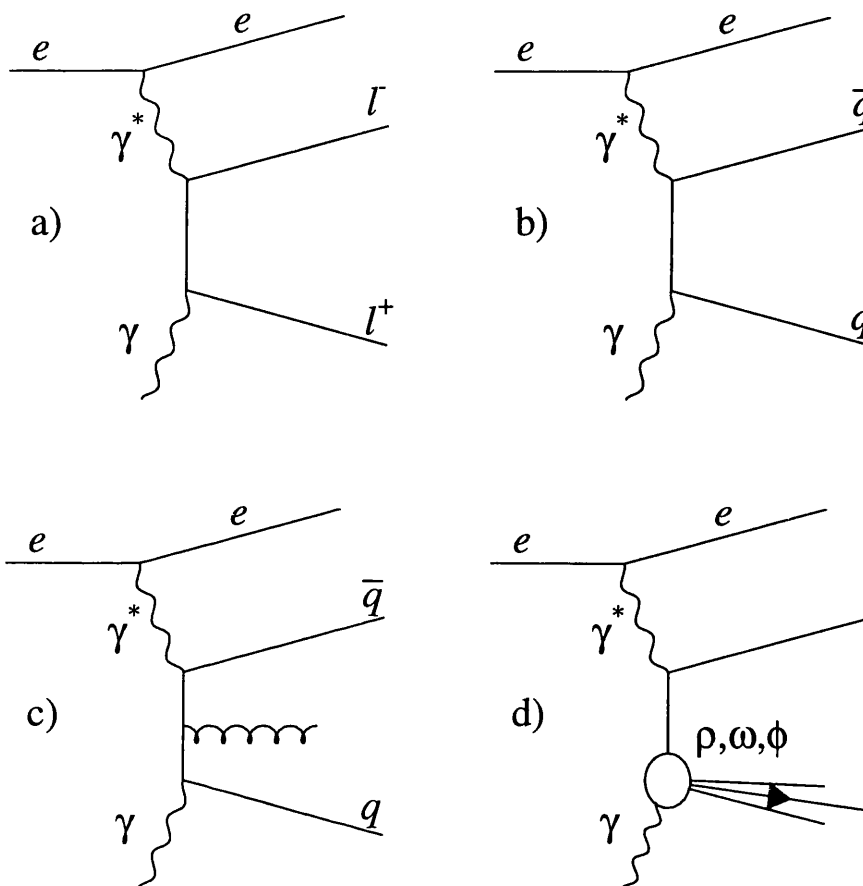


Figure 2.2: The scattering of a highly virtual photon off a quasi real target photon showing the QED contribution (a), the QPM contribution (b) and perturbative and non-perturbative QCD contributions (c) and (d) respectively.

Replacing the lepton lines in figure 2.2 (a) with quark lines gives the analogous QPM process shown in figure 2.2 (b). As in QED, an expression can be written for  $F_2^{\gamma, QPM}$  with the  $\ln(Q^2/m_l^2)$  term replaced by  $\ln(Q^2/m_q^2)$  terms dependent on the quark masses  $m_q$ . Any prediction of  $F_2^{\gamma, QPM}$  hence requires the input of unknown and poorly defined quark masses. In addition, the presence of QCD corrections represented by diagrams such as 2.2 (c), which introduce a  $\ln(Q^2/\Lambda^2)$

term (where  $\Lambda$  is the scale at which perturbative QCD becomes applicable), and the possibility that the initial  $q\bar{q}$  pair may form some bound state (figure 2.2 (d)) preclude any absolute prediction for  $F_2^\gamma$ .

As in the case of the proton, QCD is limited to predicting the behaviour of the quasi-real photon structure with  $Q^2$ , the probing photon virtuality; these predictions take the form of pdf's requiring a starting distribution at some fixed  $Q_0^2$  [26][27][28].

### 2.1.3 Measurements of $F_2^\gamma$

The main difficulty faced by those attempting to measure  $F_2^\gamma$  at  $e^+e^-$  colliders lies in reconstructing the incoming target photon energy and hence  $x$  [29]; the target photon is radiated from an electron (positron) which escapes unmeasured leaving the photon energy unknown. Measurement of the electron which has been scattered through an angle large enough for it to be detected gives the energy and virtuality of the probing photon. The target photon energy can hence be obtained by reconstructing the centre of mass energy from the produced hadronic system. An unknown amount of the produced hadronic system, however, escapes down the beampipe rendering this reconstruction problematic.

Interpretations of the measured cross-section in terms of  $F_2^\gamma(x, Q^2)$  hence require accurate simulation of the hadronic final state in order to correct for these detector acceptance effects. For a review of  $F_2^\gamma$  measurements see [30].

A more intrinsic limitation of deep inelastic  $e\gamma$  scattering is that the measurement of  $F_2^\gamma$  provides little information on the gluon content of the photon. Although measurements of  $F_2^p$  gives no direct information on the gluon content of the proton, one can make use of the fact that  $\int dx F_2^p + \int dx G^p = 1$ , where  $\int dx G^p$  represents the proton momentum carried by gluons. No such ‘‘sum rule’’ can be invoked for the photon where, as its structure comes from the initial  $\gamma \rightarrow q\bar{q}$  splitting,  $\int dx F_2^\gamma + \int dx G^\gamma = \mathcal{O}(\alpha_{em})$  [31].

Information on the gluon content of the photon is essential if one is to test the QCD inspired pdf's. HERA can provide such information.

## 2.2 Classification of $\gamma p$ Interactions

### 2.2.1 Two Classes of Resolved Photon Process

As has been discussed in chapter 1,  $\gamma p$  interactions can be separated into two distinct classes at leading order in QCD; the photon either couples directly to a parton from the proton (direct) or fluctuates into a source of partons, one of which enters the hard scatter (resolved).

A further classification of resolved photon processes is often made in order to model the behaviour of the photon. This further classification is based upon the nature of the initial  $\gamma \rightarrow q\bar{q}$  splitting. The  $q\bar{q}$  are produced with some momentum transverse to the initial photon direction. If this transverse momentum,  $k_T$ , is small the  $q\bar{q}$  pair can form a bound state and the  $\gamma p$  collision can be treated as a hadron-hadron collision (see figures 2.2 (d) and 2.3 (b)). The spin of the photon dictates that the meson formed should be akin to a spin-1 vector meson such as a  $\rho$ ,  $\omega$  or  $\phi$ . This treatment of the resolved photon structure is hence labelled the vector meson dominance (VMD) model [32].

If the  $k_T$  of the  $q\bar{q}$  is large, no bound state can be formed and the resulting system of quarks and gluons can be treated within perturbative QCD [33]. This aspect of the photon structure is labelled the anomalous component and is represented in figures 2.2 (c) and 2.3 (a).

Comparison of the photon behaviour depicted in figures 1.9 (a) and 2.2 (b) would suggest that there is some ambiguity in the separation of the direct component and the anomalous resolved component. Indeed, if the  $E_T$  of the outgoing partons in figure 1.9 (a) were derived from the  $k_T$  of the initial  $\gamma \rightarrow q\bar{q}$  splitting then one would categorize this as part of the anomalous component.

If this were to be the case, however, there would be no hard QCD ( $g \rightarrow q\bar{q}$ ) scatter and the process would not be leading order in  $\alpha_s$ . The  $E_T$  of the outgoing partons in figure 1.9 (a) must derive from the  $g \rightarrow q\bar{q}$  splitting for the process to be classified as a leading order QCD process [34]; the separation of the anomalous resolved and the direct components is hence valid at leading order.

In order to treat the resolved photon in this manner, one needs a value of the transverse momentum of the  $q\bar{q}$  pair,  $k_{Tmin}$ , below which the photon is a vector meson and above which it is a perturbative system of quarks and gluons. The choice of  $k_{Tmin}$  is arbitrary and the separation of the VMD and the anomalous components is a simplification of some more complicated structure. This simplification is, however, useful in parametrizing the structure of the photon and its behaviour as its virtuality increases, as will be discussed in section 2.3.

### 2.2.2 Separating “Direct” and “Resolved” Processes

The observable final state variable  $x_\gamma^{obs}$  was introduced in section 1.4.2 as a means of classifying photoproduction events with two or more jets (“dijet” events) as coming from direct or resolved photon processes. This classification is motivated by the assumption that the two final state jets can be associated with the two outgoing partons from the hard scatter. The photon remnant in the resolved process then differentiates it from the direct process where there is no such remnant.

Higher order effects complicate this approach. In a direct photon process, any additional hard process involving the outgoing partons will give an additional jet and hence a similar hadronic final state to a resolved photon process (see figure 2.4). The separation of the direct and resolved classes of event is hence unambiguous only at leading order. No criterion exists for an unambiguous event-by-event classification of dijet photoproduction events.

That said,  $x_\gamma^{obs}$  can be used to separate samples of events that are dominated

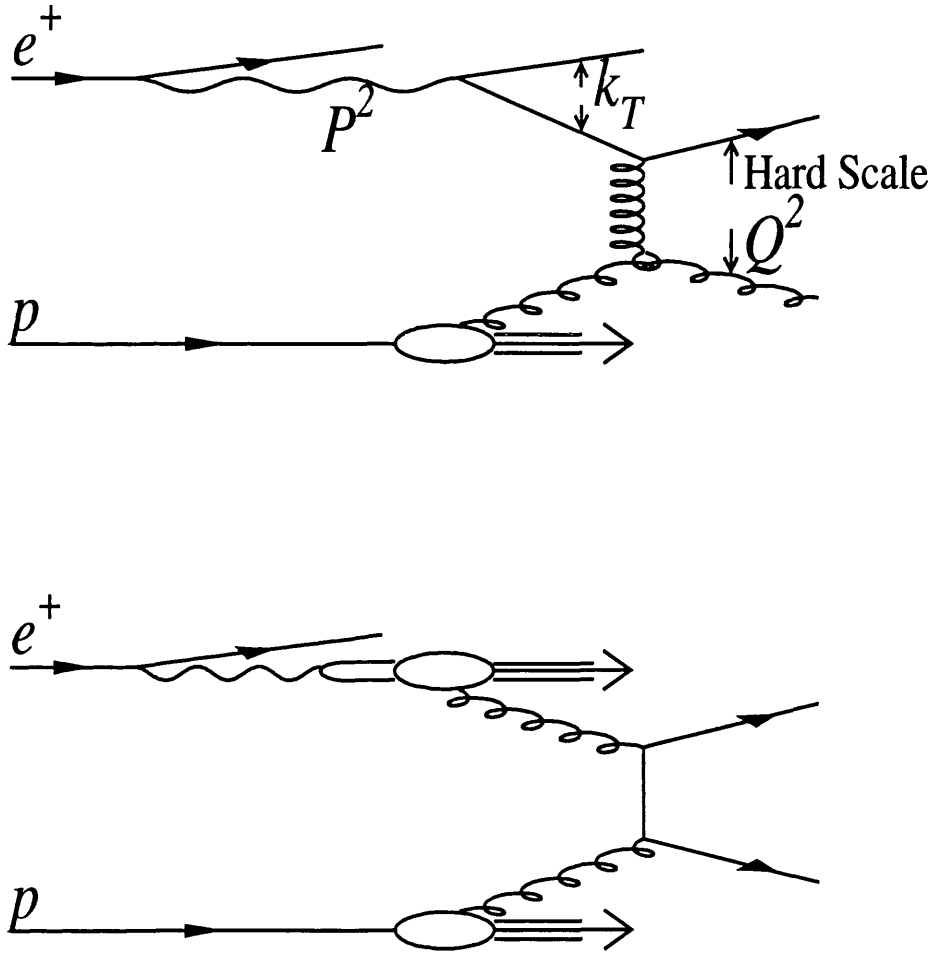


Figure 2.3: Possible diagrams for the perturbative "anomalous" resolved photon process (a) and the non-perturbative "VMD" resolved photon process (b).

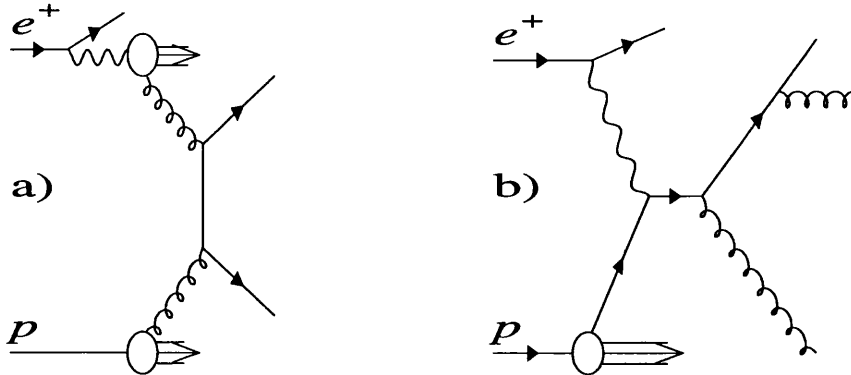


Figure 2.4: The similarity of the hadronic final states in (a) LO resolved and (b) NLO direct photoproduction illustrates that the separation of direct and resolved processes is unambiguous only at leading order.

by those coming from direct or resolved photon processes. Direct photon processes generally give high values of  $x_\gamma^{obs}$  whilst resolved photon processes give low values of  $x_\gamma^{obs}$ . A cut is imposed and any event with an  $x_\gamma^{obs} > 0.75$  is labelled as direct and any event with  $x_\gamma^{obs} < 0.75$  is labelled as resolved. These definitions are arbitrary in the sense that the value of 0.75 does not have a strong theoretical basis but it is motivated by Monte Carlo studies showing that this value gives good separation of the two event classes at leading order [19].

The main concern of this thesis is the changing nature of the direct and resolved composition of the photon with its virtuality. This has been studied by obtaining the  $x_\gamma^{obs}$  distribution for events with quasi-real photons and for events with photons of virtuality  $P^2$  in the range  $0.1 < P^2 < 0.55 \text{ GeV}^2$  and comparing the two. The virtuality has been labelled  $P^2$  following the  $F_2^\gamma$  formalism given in section 2.1.1 where  $Q^2$  is the dominant, probing scale (provided in this case by the

hard parton-parton scatter) and  $P^2$  is the virtuality of the target photon. The cut at 0.75 has been utilized to measure the ratio of the resolved dijet cross-section to the direct dijet cross-section as a function of  $P^2$ .

## 2.3 The $P^2$ Evolution of Photon Structure

### 2.3.1 Existing Data

The only existing data regarding the structure of photons with virtualities in the range now accessible at ZEUS were published by the PLUTO collaboration [35]. They measured the effective structure function  $F_{eff}^\gamma = F_2 + 3/2F_L$  at a  $Q^2$  of 5 GeV<sup>2</sup> for photons with a mean virtuality  $P^2$  of 0.35 GeV<sup>2</sup> in  $e\gamma^*$  DIS. The use of  $F_{eff}^\gamma$  was necessitated by the presence of a contribution from longitudinally polarized target photons absent when the target photons are quasi-real.

The data consisted of 78 double tagged events, those where both scattered electrons were detected. This measurement suggested that  $F_{eff}^\gamma$  decreased with increasing  $P^2$  and was consistent with an expectation based upon QPM + VMD but was limited by poor statistics.

### 2.3.2 A New Kinematic Regime

The recent developments in the ZEUS detector that have made possible the measurements presented in this thesis (see chapter 3) have renewed theoretical interest in the structure of the virtual photon [36][37][38].

Interest in the changing structure of the photon stems from the opportunity it provides to explore the transitional region between perturbative QCD and non-perturbative QCD.

This thesis compares the  $x_\gamma^{obs}$  distributions obtained from two different kinematic regimes defined by equations 2.6 and 2.7. The probing, dominant scale in this context is provided by the hard parton-parton scatter.

$$Q^2 \gg \Lambda^2 \gg P^2 \quad (2.6)$$

$$Q^2 \gg P^2 \geq \Lambda^2 \quad (2.7)$$

As  $P^2$  moves above  $\Lambda^2$  the structure of the photon should become dominated by the perturbative anomalous component whereas the non-perturbative VMD component should become less important.

### 2.3.3 Suppression of Resolved Component with $P^2$

The general expectation [36][37][38] is that as  $P^2$  increases, the contribution to the dijet cross-section from resolved photon processes should decrease relative to the contribution from direct photon processes; the lifetime of the virtual photon is governed by the uncertainty principle and so as the virtuality increases, the time that the photon has to evolve into a hadronic system decreases and hence the contribution from resolved processes decreases.

Both the anomalous and VMD contributions decrease with increasing  $P^2$  but at different rates. Equations 2.8 and 2.9 give possible  $P^2$  dependences of the two components if treated separately.

$$\text{ANOM} \propto \ln \left( \frac{Q^2}{\Lambda^2 + P^2} \right) \quad (2.8)$$

$$\text{VMD} \propto \frac{Q^2}{(m_\rho^2 + P^2)^2} \quad (2.9)$$

A more rigorous approach, where the two components are combined to avoid discontinuity is presented in [37] for example.

# Chapter 3

## ZEUS Detector

*I must hear the feet however faint they fall.*

S. Beckett - Footfalls

### 3.1 HERA

The beams of 820 GeV protons and 27.5 GeV positrons are brought into collision at two interaction points, situated at which are the ZEUS and H1 experiments. A “bunch” of particles travels in one of 220 equidistant “buckets”, each of which is paired to a bucket in the other beam. There is a prospective bunch crossing every 96 ns. In the 1994 running period 153 paired  $ep$  bunches were accompanied by 17 unmatched proton bunches and 15 unmatched positron bunches. Unmatched and empty crossings are used for background studies.

### 3.2 Overview of the ZEUS Detector

The ZEUS detector is designed to study a wide range of physics topics, some of which are discussed in chapter 1. This is achieved through a combination of sub-components that track, identify and measure the energy of particles coming from the point of interaction. Figure 3.1 shows a longitudinal section of the ZEUS

detector. The asymmetry in the incoming beam energies is reflected in the design of the detector; there is more instrumentation in the forward (positive  $z$ ) region of the detector as defined by the incoming proton direction.

Innermost are the tracking detectors: the vertex detector (VXD), the central tracking detector (CTD) and the forward and rear tracking detectors (FTD and RTD). Charged particles emanating from the interaction are deflected by a 1.4 Tesla magnetic field provided by the solenoid that encapsulates the tracking detectors. The trails of ionization left in the gas-filled wire tracking chambers are hence curved in the  $xy$  plane, the curvature giving the momenta of the particles. The analysis presented in this thesis uses CTD information to give an event vertex and to reject background events.

Sandwiched between the three FTD chambers are two transition radiation detector (TRD) modules; the combined FTD and TRD is labelled FDET in figure 3.1. Work done by myself regarding the calibration of the TRD chambers is presented in chapter 4.

Surrounding the solenoid is the main calorimeter, comprised of three sections: the forward, rear and barrel calorimeters labelled FCAL, RCAL and BCAL respectively in figure 3.1. The calorimeter is used to identify and measure jets of hadrons, reconstruct  $\sum_{hadrons}(E - p_z)$  ( $= 2E_\gamma$  in photoproduction) and to reject events due to upstream beam-gas interactions.

Two electron tagging devices are installed in the electron direction. The beam pipe calorimeter (BPC) and the luminosity tagger provide samples of events with photon virtualities in the range  $0.1 < P^2 < 0.55 \text{ GeV}^2$  and  $P^2 < 0.02 \text{ GeV}^2$  respectively.

This chapter concentrates on those components essential to this thesis; for a full account of the entire ZEUS detector see [39].

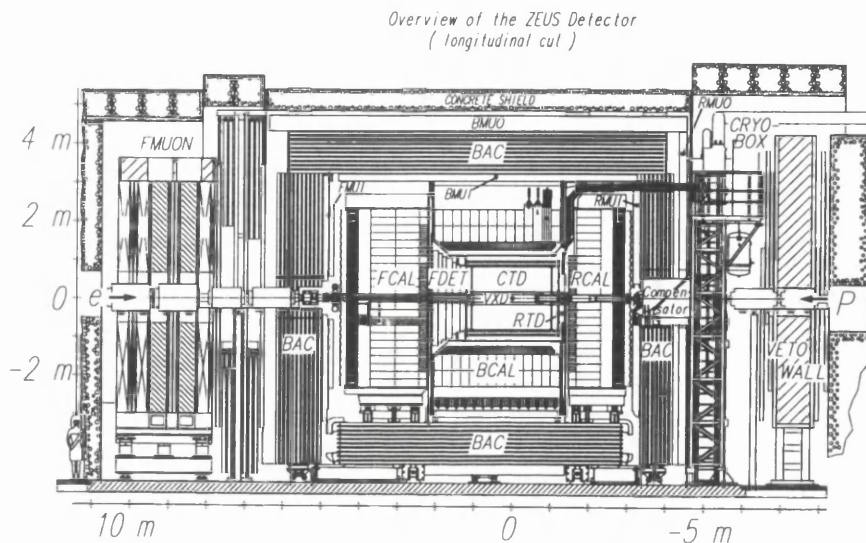


Figure 3.1: A longitudinal section of the ZEUS detector.

### 3.3 Calorimeter

#### 3.3.1 Design

As mentioned in the foregoing, the ZEUS calorimeter [40] is composed of three sections; the FCAL covers the angular range  $2.2^\circ < \theta < 39.9^\circ$ , the BCAL  $36.7^\circ < \theta < 129.1^\circ$  and the RCAL  $128.1^\circ < \theta < 176.5^\circ$ . The combined calorimeter is almost hermetic, 20cm $\times$ 20cm holes being required for the beam-pipe. This corresponds to an  $\eta$  coverage of  $-3.5 < \eta < 4.0$ . The jets used for this analysis were composed of energy deposits in cells within the  $\eta$  range  $-2.125 < \eta < 2.875$ , utilizing all sections of the calorimeter.

Each calorimeter consists of layers of depleted Uranium (DU) and plastic scintillator arranged in towers (see figure 3.2). Through electromagnetic or nuclear interactions with the DU, a particle traversing the calorimeter will cause a shower of particles. This shower will develop until the energy of the particles is low such that it is dissipated through ionization processes rather than through

the production of further particles.

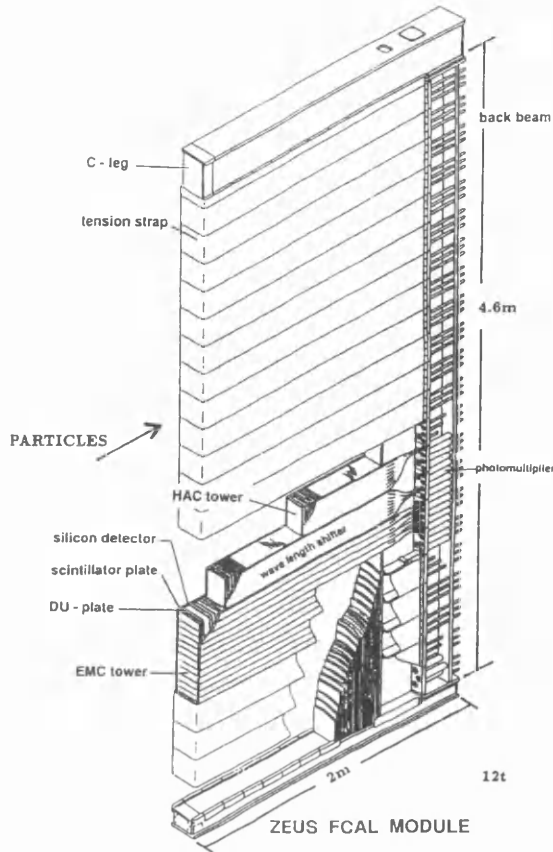


Figure 3.2: A diagram of a ZEUS FCAL module.

The development of the shower is sampled by the scintillator tiles. Light generated in the scintillator is converted to an electronic signal proportional to the energy of the incident particle by photomultiplier tubes.

It is an important task of the ZEUS calorimeter to be able to identify energy deposits that come from electrons (in order to tag and reconstruct the kinematics of DIS events for example). Equally important is the calorimeter's capability of measuring the energy and position of jets of hadrons.

Due to the differing natures of electromagnetic showers (those derived from incident electrons, positrons or photons) and hadronic showers (those derived from incident hadrons) it is possible to discriminate between the two types of

Cell Type	Face Dimensions
REMC	10cm x 20cm
FEMC	5cm x 20cm
BEMC	5cm x 25cm
RHAC	20cm x 20cm
FHAC	20cm x 20cm
BHAC	20cm x 20cm

Table 3.1: The dimensions of calorimeter cell faces.

energy deposit.

The radiation length  $X_0$  governs the distance into the calorimeter that an electromagnetic shower will propagate before the energy of the incident particle is fully dissipated [41].  $X_0$  is much smaller than the analogous nuclear interaction length,  $\lambda$  that characterizes the development of hadronic showers. In the ZEUS calorimeter,  $X_0 = 0.75\text{cm}$  and  $\lambda = 21.0\text{cm}$ . As  $\lambda \approx 25X_0$ , any electromagnetic shower peters out long before a hadronic shower has fully developed. The inner sections of the FCAL, BCAL and RCAL are hence dedicated to measuring the energy of electromagnetic showers (the ECAL), the outer sections to the measurement of hadronic energy (HCAL).

Table 3.3.1 shows the face dimensions of ECAL and HCAL cells for both the FCAL and RCAL. The inner sections have a finer granularity to reflect the fact that electromagnetic showers are narrower than hadronic showers [41].

### 3.3.2 Response and Resolution

A jet of hadrons is characterized by the angular variables  $\eta^{jet}$  and  $\phi^{jet}$ . In a simulated event (see chapter 5) these variables can be calculated directly from

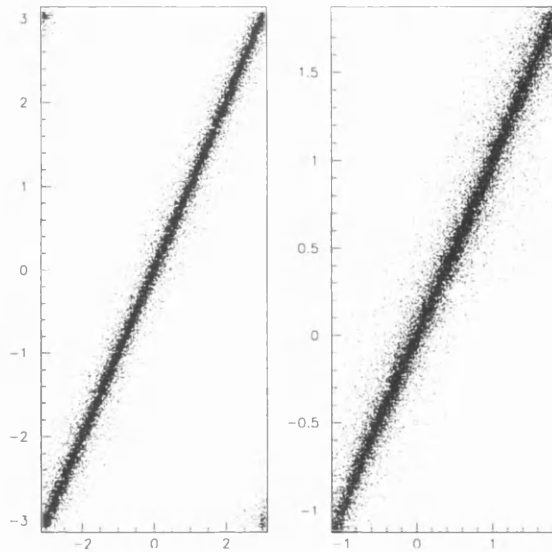


Figure 3.3: Scatter plots of  $\phi_{rec}^{jet}$  vs  $\phi_{had}^{jet}$  (left) and  $\eta_{rec}^{jet}$  vs  $\eta_{had}^{jet}$  (right) in simulated events (see chapter 5) displaying the excellent  $\eta$  and  $\phi$  resolution of the main ZEUS calorimeter.

the four-momenta of the particles entering the calorimeter ( $\eta_{had}^{jet}$ ,  $\phi_{had}^{jet}$ ) and from simulated calorimeter cell deposits ( $\eta_{cal}^{jet}$ ,  $\phi_{cal}^{jet}$ ). Figure 3.3 shows the strong one-to-one correlation between the two indicating that the granularity of the calorimeter provides an accurate measurement of these quantities.

A jet of hadrons will give rise to both a hadronic shower and a number of electromagnetic showers due to decays such as  $\pi^0 \rightarrow \gamma\gamma$ . To measure the energy of the jet accurately and without bias due to the level of the electromagnetic component of the jet, it is desirable that the calorimeter has an equal response to hadronic and electromagnetic energy deposits.

The response to electromagnetic showers is generally greater than the response to equivalent hadronic showers as a large amount of the energy of an incident hadron is lost to the binding energy of the Uranium nucleus in forming secondary hadrons.

This “lost” energy can be “compensated” through elastic interactions between

low energy neutrons from Uranium spallation and protons in the hydrogen nuclei of the plastic scintillator. The protons ionize the scintillator producing light and hence an additional signal. The amount of compensation is dependent upon the relative thicknesses of the uranium and scintillator layers.

The ZEUS calorimeter has the correct thickness of Uranium and scintillator layers such that there is an equal response to hadronic and electromagnetic showers [42]. This makes the response to a hadronic shower independent of the  $\pi^0$  content of that shower and hence improves the hadronic energy resolution. The energy resolutions for the ECAL and HCAL are given by equations 3.1 and 3.2 respectively where  $\oplus$  denotes that the terms sum in quadrature.

$$\frac{\sigma_E}{E} = \frac{0.18}{\sqrt{E}} \oplus 0.01 \quad \text{for Electrons} \quad (3.1)$$

$$\frac{\sigma_E}{E} = \frac{0.35}{\sqrt{E}} \oplus 0.02 \quad \text{for Hadrons} \quad (3.2)$$

There are two further advantages of the choice of a DU and plastic scintillator calorimeter. The radiation from natural (non-induced) Uranium decays acts as a source through which to monitor and calibrate the response of the scintillator, waveguide and photomultiplier system. This acts to preserve the absolute calibration derived from test beam results.

The fast response of the plastic scintillator gives the calorimeter a time resolution of 2ns. This provides a very powerful tool for rejecting background events (see chapter 6).

## 3.4 Positron Taggers

### 3.4.1 LUMI tagger

The luminosity positron tagger (LUMI tagger) [42] lies 35m from the interaction point in the direction of the initial positron beam (see figure 3.4).

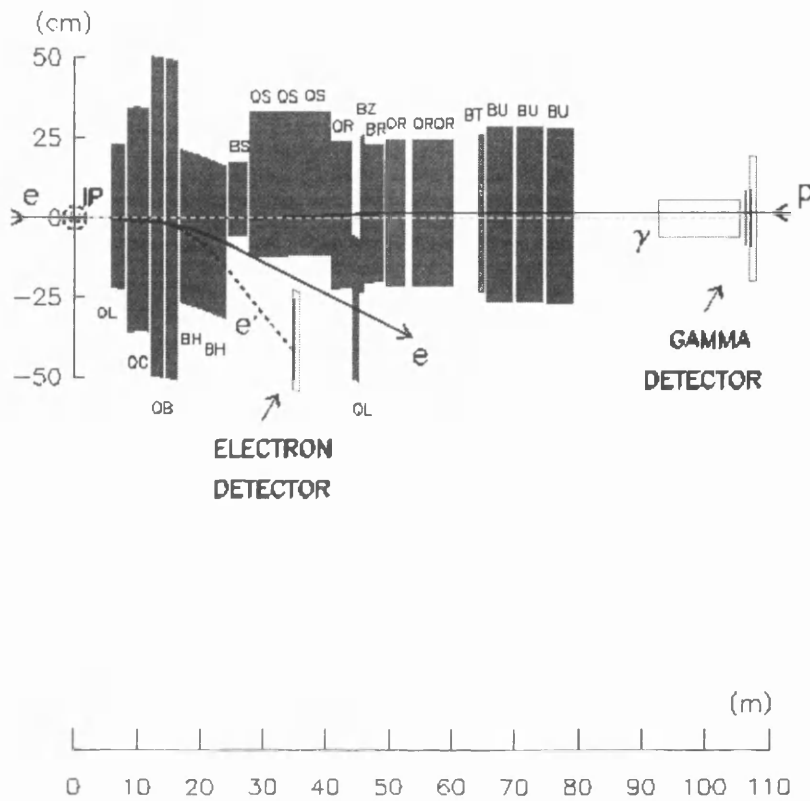


Figure 3.4: The ZEUS luminosity detector showing the LUMI positron (electron) detector.

As the electron beam is deflected from the straight “interaction” section of the HERA ring, the beam magnets act as a spectrometer, separating the electrons that have lost energy through photoproduction reactions or photon bremsstrahlung from the rest of the beam. Electrons with an energy in the range  $0.1E_e < E'_e < 0.9E_e$  can be deflected into the luminosity electron tagger, a lead and plastic scintillator calorimeter.

The resulting shower is measured with an energy resolution of

$$\frac{\sigma_E}{E} = \frac{0.15}{\sqrt{E}} \quad (3.3)$$

allowing a direct measurement of the photon energy independent of that provided by the main calorimeter ( $E_\gamma = E_e - E'_e = yE_e$  in photoproduction events). A

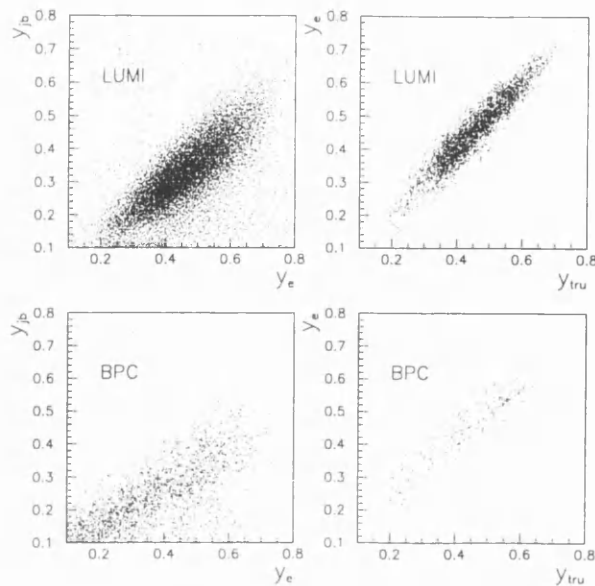


Figure 3.5: The measurements of  $y_e$  of the LUMI tagger and the BPC compared to  $y_{jb}$  and, for simulated events, to  $y_{tru}$ .

comparison of the two measurements of  $y$  via the main calorimeter ( $y_{jb}$ ) and the LUMI tagger ( $y_e$ ) is shown in figure 3.5 (top left), along with the correlation between  $y_e$  and  $y_{tru}$  for simulated events (top right) where  $y_{tru}$  is taken directly from the event kinematics.

A silicon strip detector provides a measurement of the position of the electron induced shower in the calorimeter. Due to the fact that the electron has been influenced by a number of magnets this position measurement cannot be used to measure the angle  $\theta_e$  through which the electron was scattered at interaction. This precludes a measurement of the photon virtuality; an upper limit on  $P^2$  of  $0.02 \text{ GeV}^2$  can be assigned to events tagged in this fashion however by considering the maximum angle through which an electron can be scattered and still escape down the beampipe. The position measurement is used only to select events where the shower is well contained by the calorimeter.

### 3.4.2 Beampipe Calorimeter

1994 saw the installation of a prototype device designed to provide a first look at HERA physics at low photon virtualities. The beampipe calorimeter (BPC) [43] was situated 3.04 m from the interaction point in the electron direction (see figure 3.6) and tagged electrons scattered through very small angles such that  $\pi - 35\text{mrad} < \theta_e < \pi - 17\text{mrad}$ . The device was placed on the inside of the storage ring next to the beampipe. A steel and tungsten flange (2.8 radiation lengths) in front of the detector acted as a preshowering device. A sample of events with  $P^2$  in the range  $0.1 < P^2 < 1.1 \text{ GeV}^2$  was provided. The low acceptance of the prototype BPC (it was a partial device covering approximately 1 rad in  $\phi$ ) resulted in the sample of events with two or more jets in the final state being restricted to the range  $0.1 < P^2 < 0.55 \text{ GeV}^2$ .

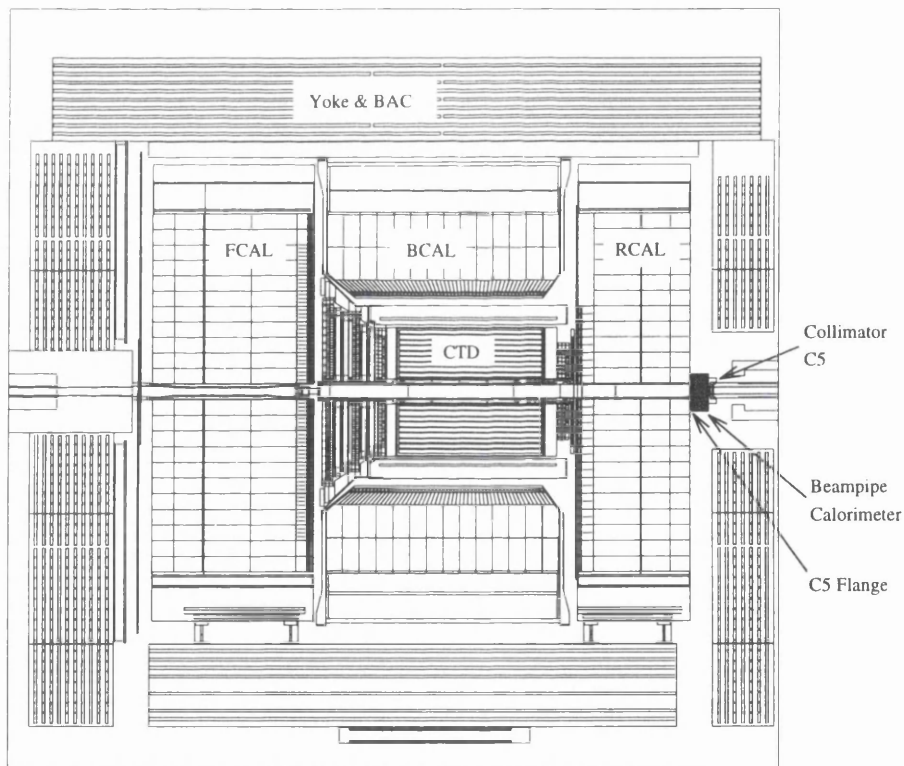


Figure 3.6: The position of the BPC relative to the rest of the ZEUS detector.

The calorimeter consisted of eight layers of tungsten sandwiched between nine

layers of silicon diodes (see figure 3.7). Two orthogonal strip detectors placed in front of the first layer of diodes provided a measurement of the  $x$  and  $y$  coordinates of the incident electron.

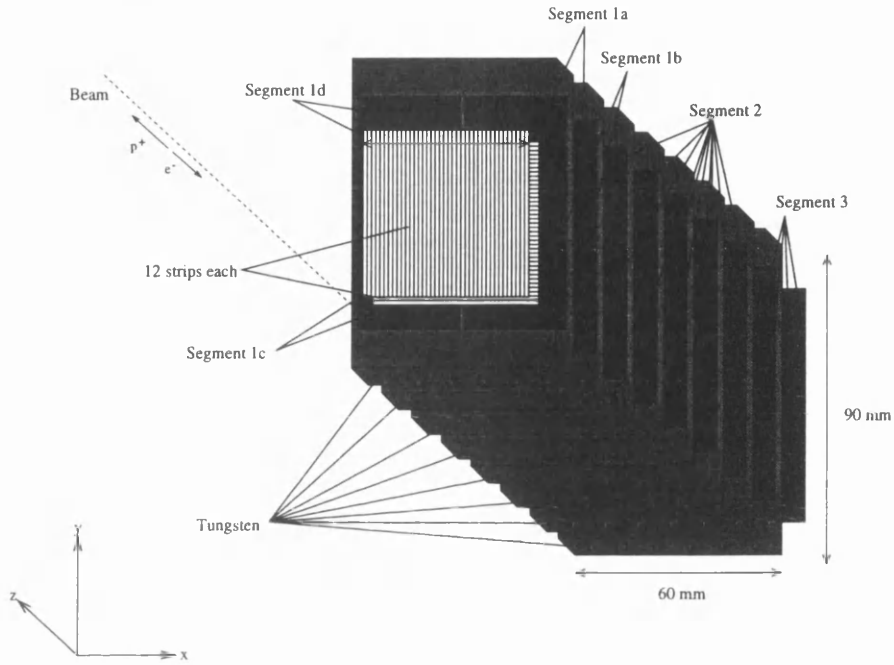


Figure 3.7: The composition of the BPC.

The energy resolution of the BPC has been measured to be

$$\frac{\sigma_E}{E} = \frac{0.28}{\sqrt{E}} \quad (3.4)$$

and the position resolution is  $\approx 3\text{mm}$ .

The errors on the measurement of the electron energy and position give a  $P^2$  resolution of 0.1 - 0.2  $P^2$ . Scatter plots of  $y_{jb}$  vs  $y_e$  and  $y_e$  vs  $y_{tru}$  for data and simulated events respectively are shown in figures 3.4.1 c) and d). Figure 3.8 shows the correlation between the measured and true values of  $P^2$  for simulated events.

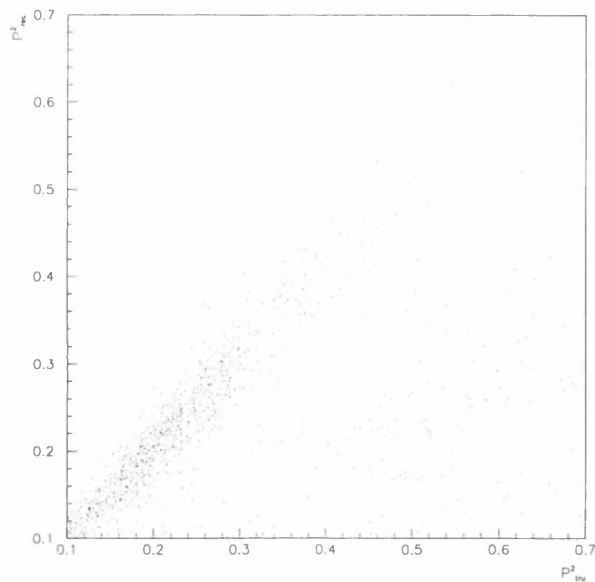


Figure 3.8: A comparison of the BPC reconstructed  $P^2$  and  $P_{tru}^2$  (both in  $\text{GeV}^2$ ) for simulated events.

## 3.5 Central Tracking Detector

For the purposes of this thesis, information from the CTD is used only to provide an event vertex and to reject background events (see chapter 6). Only those aspects of the CTD design relevant to these ends are discussed here. These include the determination of the  $z$  position of the primary vertex and the evaluation of the number of “bad-vertex tracks”.

### 3.5.1 CTD overview

The CTD [42] is a cylindrical drift chamber covering the angular range  $15^\circ < \theta < 164^\circ$ . The chamber contains an argon based gas. Charged particles traversing the detector ionize the argon molecules producing ionization electrons that drift toward a sense wire resulting in a pulse on that sense wire.

The signal from each sense wire is amplified and digitized and each pulse is

characterized by an amplitude and a time of arrival. If the amplitude of the pulse is larger than a certain threshold it is regarded as a “hit”.

The maximum drift time is 500 ns. Although this is larger than the crossing interval, this causes no practical difficulties as many crossings are empty and the inclination of the cells ensures that a track constituted of several hits has at least one drift time measurement less than the 96 ns crossing interval.

The drift velocities of ionization electrons in the gas are known and the arrival time can be converted into the distance from the wire that the initial ionization took place and hence the distance at which the particle passed. It is not known, however, from which side of the wire the ionization originated. This ambiguity results in each hit being accompanied by a “ghost hit” on the opposite side of the wire.

Nine “superlayers” of wires run the two metre length of the detector; five “axial” superlayers with wires running parallel to the  $z$  axis are interspersed with four “stereo” superlayers, the wires of which are at angles of  $\pm 5^\circ$  to the  $z$  axis (see figure 3.9).

Signals on the wires of superlayer one and on alternate wires in superlayers three and five are read out at both ends of the chamber. Comparison of the arrival times at each end gives a rough value of the  $z$  coordinate of the hit. This mechanism is known as “ $z$ -by-timing” and provides information for the trigger system (see chapter 6).

### 3.5.2 Vertex Reconstruction

A number of hits in one superlayer constitute a “segment”. Segments formed of valid hits point towards the interaction region whereas those formed of ghost hits do not. The ambiguity caused by ghost hits can thus be resolved. Tracks are constructed by matching segments from consecutive axial superlayers in the  $xy$  plane, starting from superlayer 9 and working inwards. Information on the

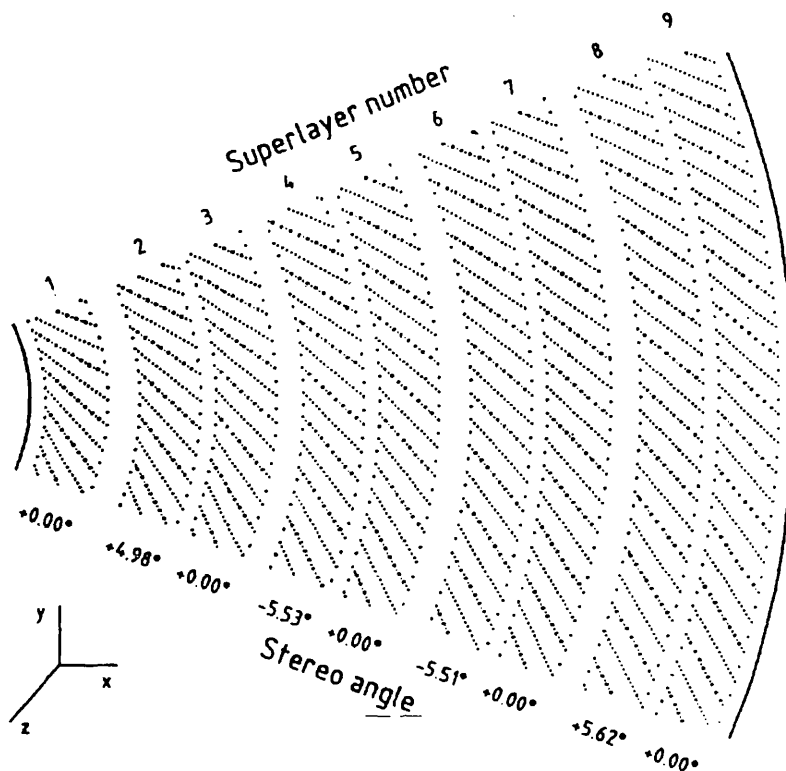


Figure 3.9: An octant of the CTD showing the arrangement of wires in “superlayers”.

progression in  $z$  of the track is provided by hits in the stereo superlayers and by hits on those axial wires equipped to provide “ $z$  by timing”. Tracks point to a  $z_v = z$  at closest approach to beam axis.

An event vertex can be reconstructed from one track (incorporating the beam axis) or from many tracks intersecting in the interaction region. The  $z$  position of this vertex is used to identify genuine  $ep$  events and to reject those events due to beam gas events (see chapter 6).

### 3.5.3 “Bad-Vertex” Tracks

It is possible for a beam gas event to have a reconstructed vertex in the required range of  $z$ . Counting the number of tracks that point to a  $z_v$  of less than -75 cm, rather than to the reconstructed vertex, can identify such events. Only tracks

with more than twenty five hits comprised of at least five stereo hits and five axial hits with a transverse momentum  $p_T > 200$  MeV are considered in determining the number of these tracks, labelled as “bad-vertex” tracks - good quality tracks that point to a vertex upstream of the interaction region.

The analysis presented in chapters 6 to 8 relies on information from the main calorimeter, the CTD and the two electron taggers discussed in the foregoing.

# Chapter 4

## ZEUS TRD Chambers

*Gold: Why did you have me if you didn't want me?*

*Gold Snr: How did we know it'd be you?*

Joseph Heller - Good as Gold

The physics output of the ZEUS detector is enhanced by reliable electron identification. To this end two transition radiation detector (TRD) modules [42] each consisting of two TRD chambers, are installed in the forward (proton direction) region of the detector (see figure 3.1). They are intended to provide information relevant to particle identification complementary to that provided by the main calorimeter and by the CTD through the measurement of shower characteristics and  $dE/dx$  energy loss respectively (see [41] for a review of particle identification). This chapter concerns work done by myself on mapping the response of the TRD chambers over the surface of the chambers.

### 4.1 The ZEUS Transition Radiation Detectors

When a charged particle traverses a boundary between two media it emits transition radiation [44]. Relativistic particles produce photons in the X-ray region of the electromagnetic spectrum. When more than one boundary is

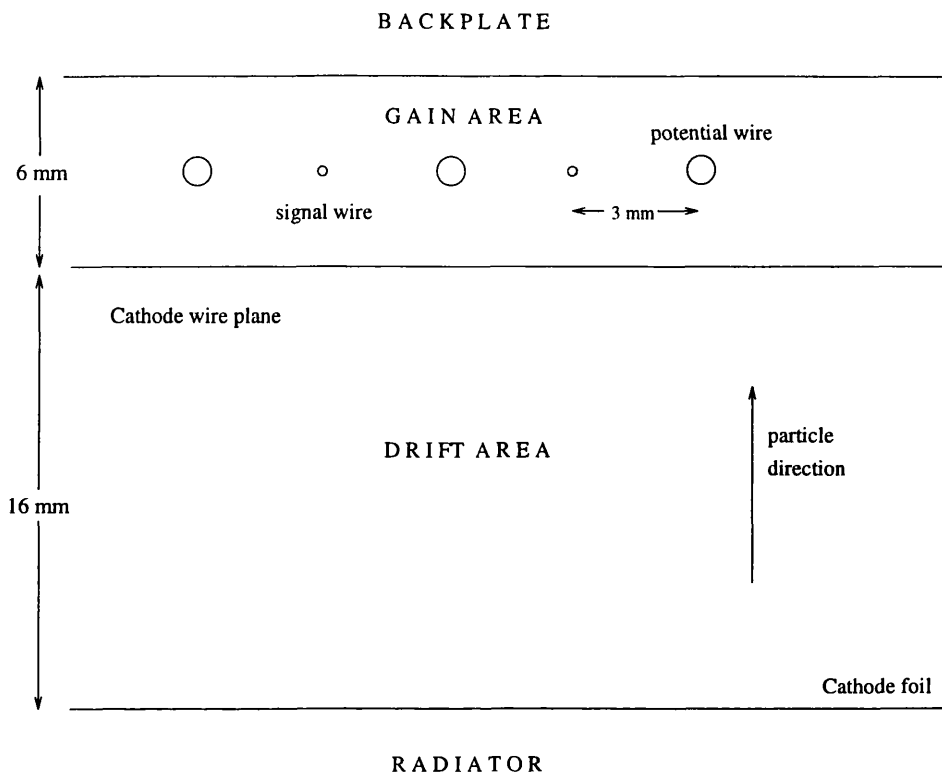


Figure 4.1: A section of a ZEUS TRD chamber viewed from above

crossed, the intensity of the radiation produced is proportional to the Lorentz factor  $\gamma = E/m$  of the particle, where  $E$  denotes the energy of the particle and  $m$  its rest mass, and to the number of boundaries crossed [44]. Transition radiation X-rays ionize the gas in the drift region of the chambers causing localized clusters of ionization which are then detected. The  $\gamma$  dependence of the intensity of the radiation means that transition radiation detection can be used to distinguish between different particle types. Good separation of electrons and pions can be achieved. The main envisaged use of the ZEUS TRDs is to help distinguish electrons/positrons from a substantially larger background of pions. This would aid studies of the leptonic decays of charmed mesons including the  $J/\psi$  for example.

Figure 4.1 shows a section of a TRD chamber viewed from above. Each of the four TRD chambers has a 70 mm layer of compressed 20  $\mu\text{m}$  polypropylene (PP) fibres within a radiator volume through which is pumped carbon dioxide. Particles traversing this radiator will cross a great number of PP/CO<sub>2</sub> boundaries before entering a drift region filled with a 90-8-2 mix of Xenon, carbon dioxide and isobutane gases. A foil at -1600 volts separates the radiator and drift regions. In the drift region, transition radiation photons can ionize Xenon atoms spawning electrons that drift away from the cathode foil causing further ionization, and anions that are collected at the cathode foil. An amplification region follows the drift region. This consists of a plane of horizontal cathodes at 0 volts, a plane of vertical anodes at 1600 volts and a backplane at 0 volts, each separated by three millimetres. Ionization electrons entering the amplification region are greatly accelerated by the strong electric field and cause an avalanche of further ionization which is deposited on one of the anode signal wires. The signal from this wire is converted to a digital pulse by dividing it into eighty time bins of ten nanoseconds. For each time bin an average amplitude over that bin is calculated in FADC counts. If this pulse satisfies certain threshold requirements, various properties of the pulse are stored. These include the total integrated signal (the total charge) and the pulseheight and time bin of any found clusters. A cluster is defined as any peak of eight counts above the baseline of the pulse. The baseline is calculated by taking the average height of the pulse over the first five time bins. A typical pulse is shown in figure 4.3.

A vast majority of found clusters are not due however to the absorption of transition radiation photons. The first found cluster (the cluster with the lowest time bin attributed to it) is generally due to the ionization caused when the charged particle traverses the amplification region. The geometry of the chambers results in ionization from both sides of the anode wire arriving during the same time period, thus generating a peak in the signal at an early time bin. Clusters caused by large localized amounts of ionization in the drift region will occur at

later time bins due to the slow drift velocity ( $35 \mu\text{m}/\text{ns}$ ) of the ionization electrons compared to the particle velocity. Most later clusters are due to high energy recoil electrons (delta rays) produced in the drift area by pions. Electrons also produce delta rays.

For the TRDs to help distinguish between electrons and pions it is essential to utilize any differences between pulses due to these different particle types. Electrons give rise to pulses that have a larger total charge than those due to pions. This is simply because electrons have a higher level of energy loss than pions at the energies concerned and produce transition radiation in addition. Monte Carlo studies [45] show that the energy of a TR photon absorbed in the drift region has a lower limit of 3 keV, whilst it is known that the number of delta rays is inversely proportional to their energy [46]. Imposing an energy threshold of 3 keV on found clusters would therefore reject a large number of delta ray induced pulses, and hence a large number of pions, without reducing the number of TR photon induced pulses. The magnitude of a found cluster is not, however, measured in keV but rather in FADC counts. An energy calibration is therefore required before an energy threshold can be applied. In addition to this absolute energy calibration, a relative calibration over the surface of each chamber is required to ensure that the threshold is equivalent for all pulses to which it is applied. The method used for this relative calibration is given in the next section.

## 4.2 Mapping the Response of the TRD

The total charge deposited on a signal wire by a passing charged particle is sensitive to the gas gain of the chamber at the point the particle passes. The higher the gas gain is, the larger the avalanche of ionization electrons that is deposited on the signal wire and hence the larger the total integrated charge of the pulse. The average total charge of pulses caused by particles traversing a

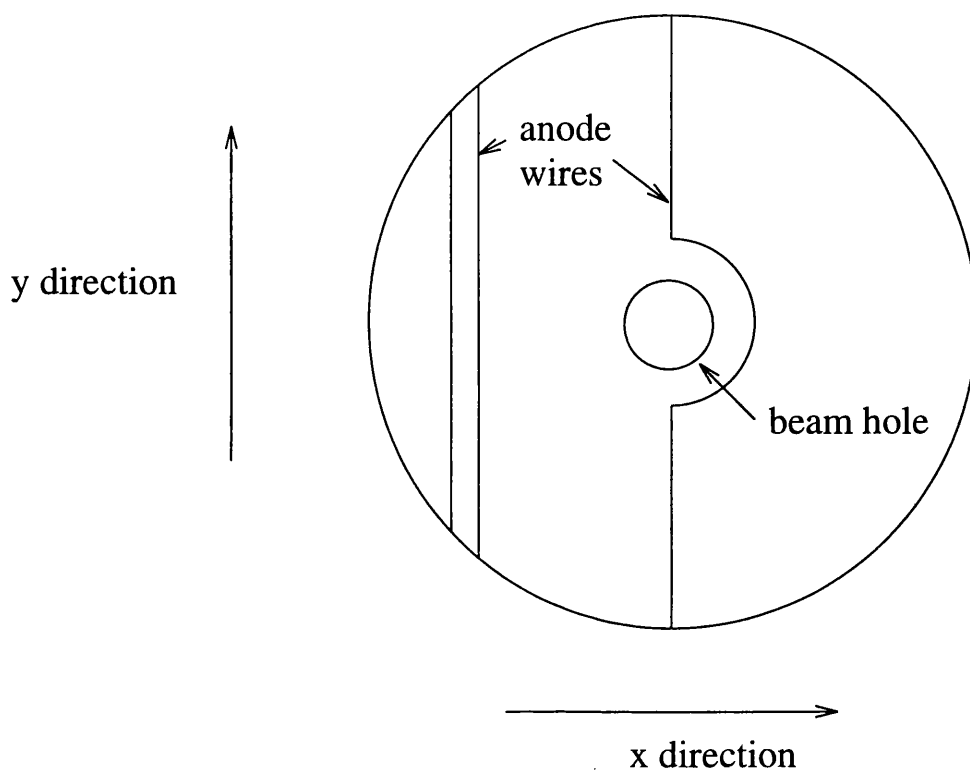


Figure 4.2: An end on view of a TRD chamber showing anode wire plane. To bypass the beamhole, the two halves of the wire are connected by a printed circuit board allowing it to be read out from one end only.

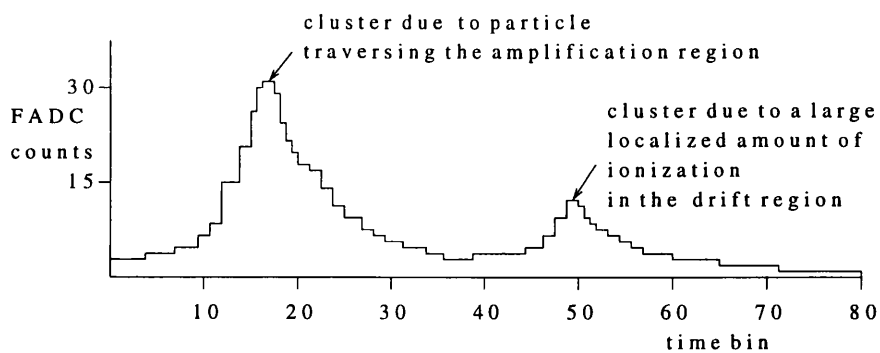


Figure 4.3: A typical TRD anode pulse showing clusters of ionization.

chamber at a certain point should therefore give an indication of the level of gain at that point. Relative energy calibration was attempted by mapping the average total charge over the surface of each of the four chambers.

In all that follows the four TRD chambers are numbered with respect to their distance from the interaction point with TRD1 being the closest and TRD4 the farthest. Chambers one and two are housed in TRD module one, chambers three and four in TRD module two.

### 4.2.1 Preliminary Considerations

To map the average total charge over the surface of a chamber, each pulse used contributed to the average of a bin in  $x$  and  $y$  defined by the position that the particle thought responsible for the pulse crossed the anode wire plane. Each anode wire has a well defined  $x$  position (see figure 4.2), but at which point along the length of the wire the ionization was deposited is unknown. It is therefore necessary to associate a TRD pulse with a particle track found by the external wire chamber tracking detectors that “sandwich” the TRD modules (see figure 3.1). A delay in the commissioning of the forward tracking detector (FTD) meant that only tracks found by the central tracking detector (CTD) could be used. The  $y$  coordinate attributed to the pulse is supplied by extrapolating the CTD track to the wire plane of the chamber in question. To match a TRD pulse with an extrapolated CTD track there must be a match between the  $x$  position of the anode wire in question and the  $x$  coordinate of the extrapolated track. The long extrapolation involved and the possibility of scattering in the material that lies between the CTD and the TRD chambers introduces an error on the extrapolated track coordinates of  $\approx 1\text{cm}$ , larger than the 6mm spacing of the signal wires in the TRD. The ionization due to a particle with a CTD track can be deposited, therefore, on any one of three anode wires. If more than one of these wires shows a found cluster, there is no unambiguous match between the track and a single

pulse.

An investigation was made into how often the neighbours of the wire with a found cluster nearest to and within one centimetre of a track, also showed a cluster. The results of this investigation are shown in figure 4.4, the zero bin indicating the cases where no cluster was found on any of the wires in the band given by the  $x$  coordinate of the track and its error. It can be seen that in up to fifty percent of cases where a wire sufficiently close to the track showed a found cluster, at least one of its neighbours did also. The level of this effect varies between the four chambers and is most marked in chambers one and two. This raised the possibility that there could be extensive hit sharing taking place whereby the ionization caused by one particle is shared between two adjacent wires. In this scenario the first found cluster on each wire would have very similar time bins. Tracks entering the chamber at a large angle could also leave deposits on two adjacent wires, a cluster on one wire coming from ionization early in the drift region, a cluster on the next due to the particle traversing the amplification region. For this case there is both an upper and lower limit on the difference in the time bin of the first found cluster due to the geometry of the chamber, the drift velocity of the gas and the maximum angle at which tracks can enter the chamber. In both of these situations the pulses should be added to give the true total ionization produced by that particle.

Figure 4.5 shows an attempt to classify neighboured pulses by looking at the difference in time bin of the first found clusters on the adjacent wire,  $\Delta$ , for chambers one and four. The right hand plots show what this  $\Delta$  distribution would look like if the pulses had no causal link of the type discussed in the foregoing. This was obtained by taking the time bins of first found clusters from remote wires and subtracting them.

It can be seen that the  $\Delta$  distribution is more sharply peaked at zero for the adjacent wires than for the remote wires. The difference between the distribution

in the central nine bins can be interpreted as the level of hit sharing putting this at nought to ten percent of the adjacent wire cases. This value increases from chamber one to chamber four. The broad similarity between the “adjacent” and “remote” distributions suggests that no conclusion can be drawn from the value of  $\Delta$  in an individual circumstance, removing the possibility of identifying hit sharing or large angle tracks. It should be noted that there is a background of particles coming from photon conversions in the material between the CTD and the TRDs for which there are no tracks, due to the delay in commissioning the FTD. This background probably provides the dominant contribution to this effect of found clusters on adjacent wires.

### 4.2.2 Constructing the “Gain Maps”

For each event with CTD tracks entering the TRD chambers, an attempt was made to match TRD pulses to extrapolated CTD tracks. Only tracks separated from the other tracks in the event by at least 5cm in the  $x$  direction at the anode plane of TRD1 were considered in an attempt to reduce ambiguities in the track - pulse matching. The pulse of the anode wire nearest the extrapolated track was attributed to that track on two conditions: that the shortest distance between the wire and the extrapolated track was less than the error on the  $x$  coordinate of the track; and that neither of the neighbouring wires showed a found cluster in that event. When a pulse and track were matched in this manner the total integrated charge of the pulse contributed to the running average for the relevant bin in  $x$  and  $y$ .

One of the main problems with the TRD chambers has been that the tension in the wires has acted to bend the backplane causing high voltage trips at lower high voltages than the nominal operating values. This bowing of the backplane could lead to a variation of the gas gain over the surface of the chamber with the gain in the centre of the chamber being reduced. There are, however, no

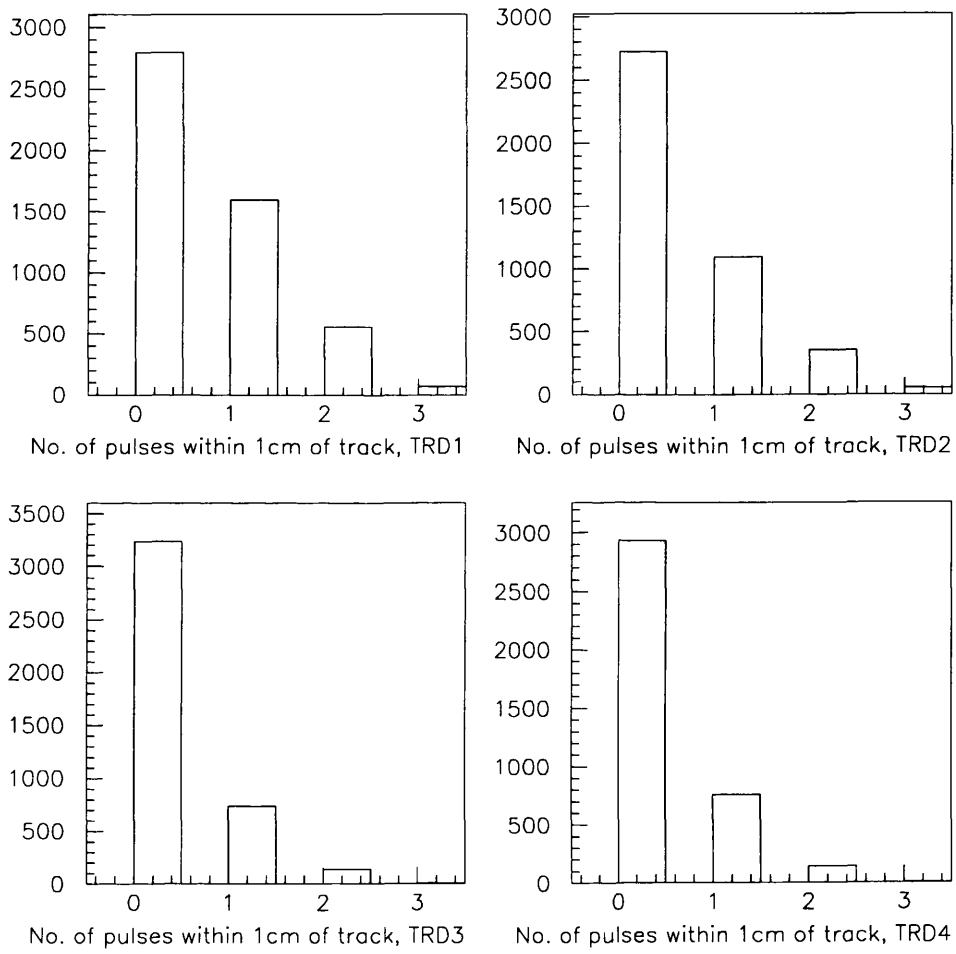


Figure 4.4: The number of wires showing clusters within 1cm of an extrapolated track. Only groups of adjacent wires contribute to bins 2 and 3.

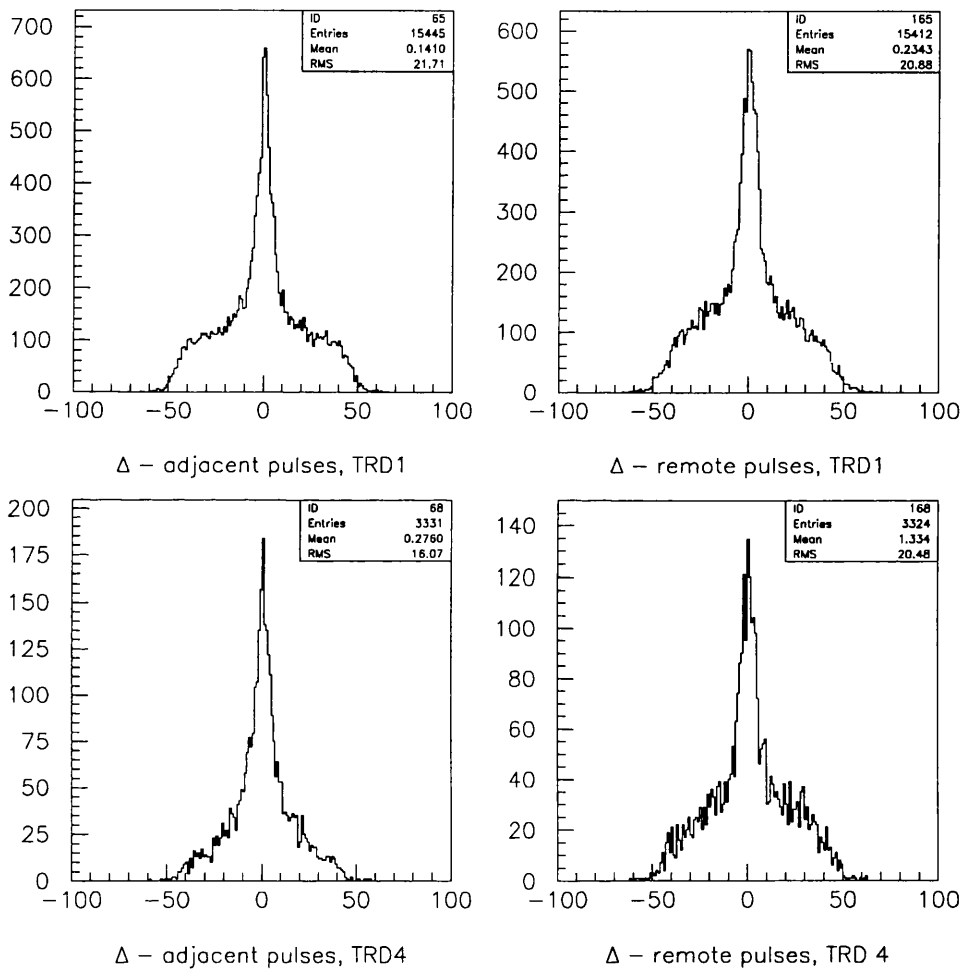


Figure 4.5: The distribution of  $\Delta$  for adjacent pulses (left) compared to a randomly generated distribution of the same quantity for remote wires (right), chambers one and four.

entries for the bins around the beam hole as CTD tracks in this area are not well constructed. The outlined method is therefore unable to investigate gain variations in this region.

In addition to the variation of the gas gain over the surface of the chambers, the method used should be sensitive to any attenuation of the pulse as it travels along the signal wire to the readout electronics. Such an attenuation would manifest itself as a decrease in the average total charge with increasing distance from the end of the wire from which the signal is read out. Choosing a bin size of  $10\text{cm} \times 10\text{cm}$  means that each  $x$  bin represents a group of sixteen wires read out by the same amplifier and hence at the same end. Wires that bypass the beam hole could show a different response on the two halves of the wire due to losses in the printed circuit board that connects them.

Figures 4.6 to 4.9 show the variation of average total charge with  $y$  bin for each  $x$  bin in the specified chamber. The bins that cover the beam hole area (bins 7 and 8 in both  $x$  and  $y$ ) have no entries, as do some of the extreme outer bins. In these cases the errors on the points have been set artificially high so that these points do not affect the linear fit applied to the data.

Chambers three and four show no significant variation in average total charge as a function of  $y$ . Several  $x$  bins in chambers one and two do, however, show some definite slope in average total charge against  $y$ . Furthermore; if the value of this slope ( $\delta\text{avtc}/\delta y$ ) is plotted as a function of  $x$  (see figure 4.10), it can be seen that this quantity increases across chambers one and two whilst showing no significant trend in chambers three and four.

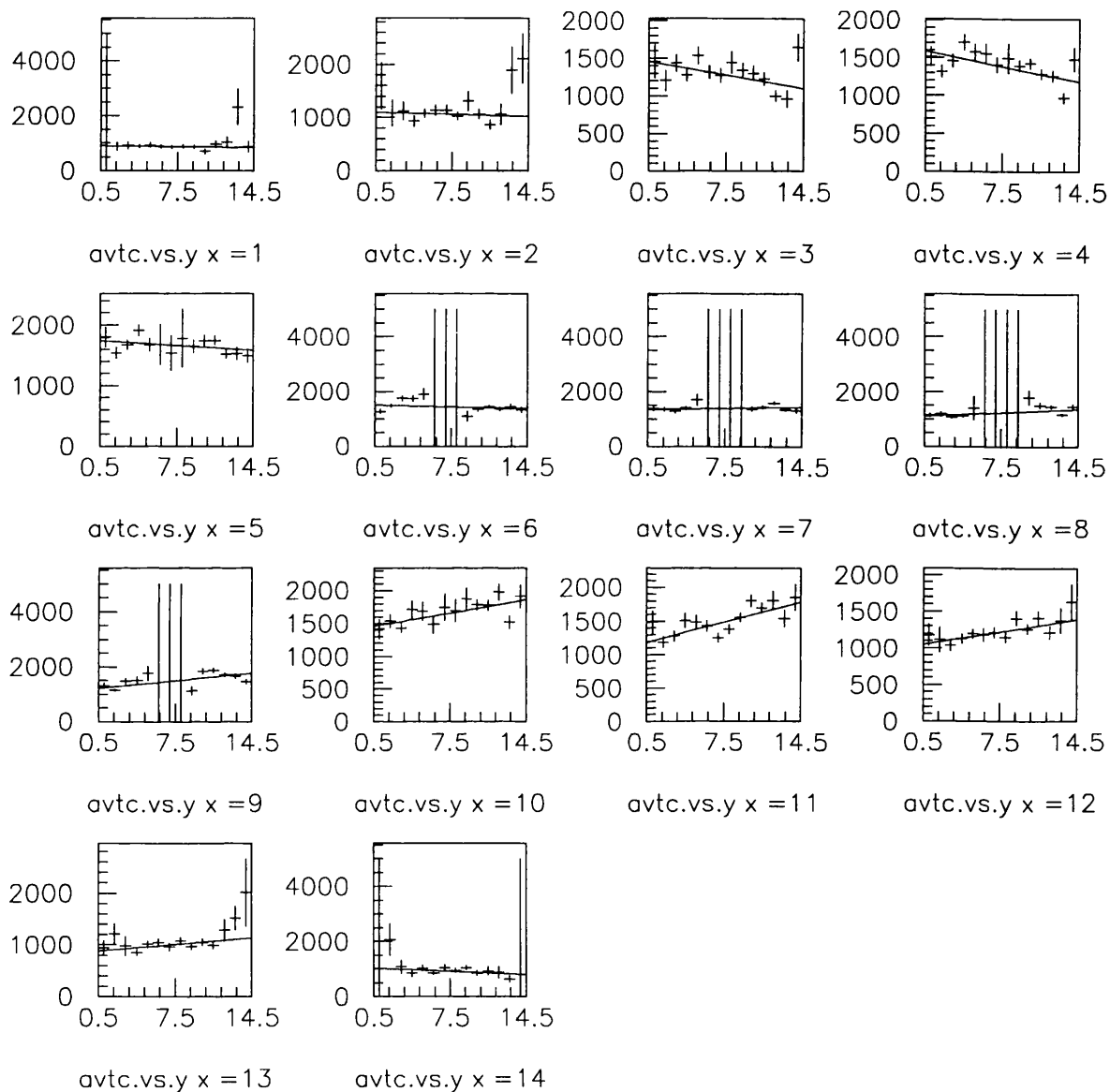


Figure 4.6: Average total charge (avtc) against  $y$  bin for each  $x$  bin TRD1.

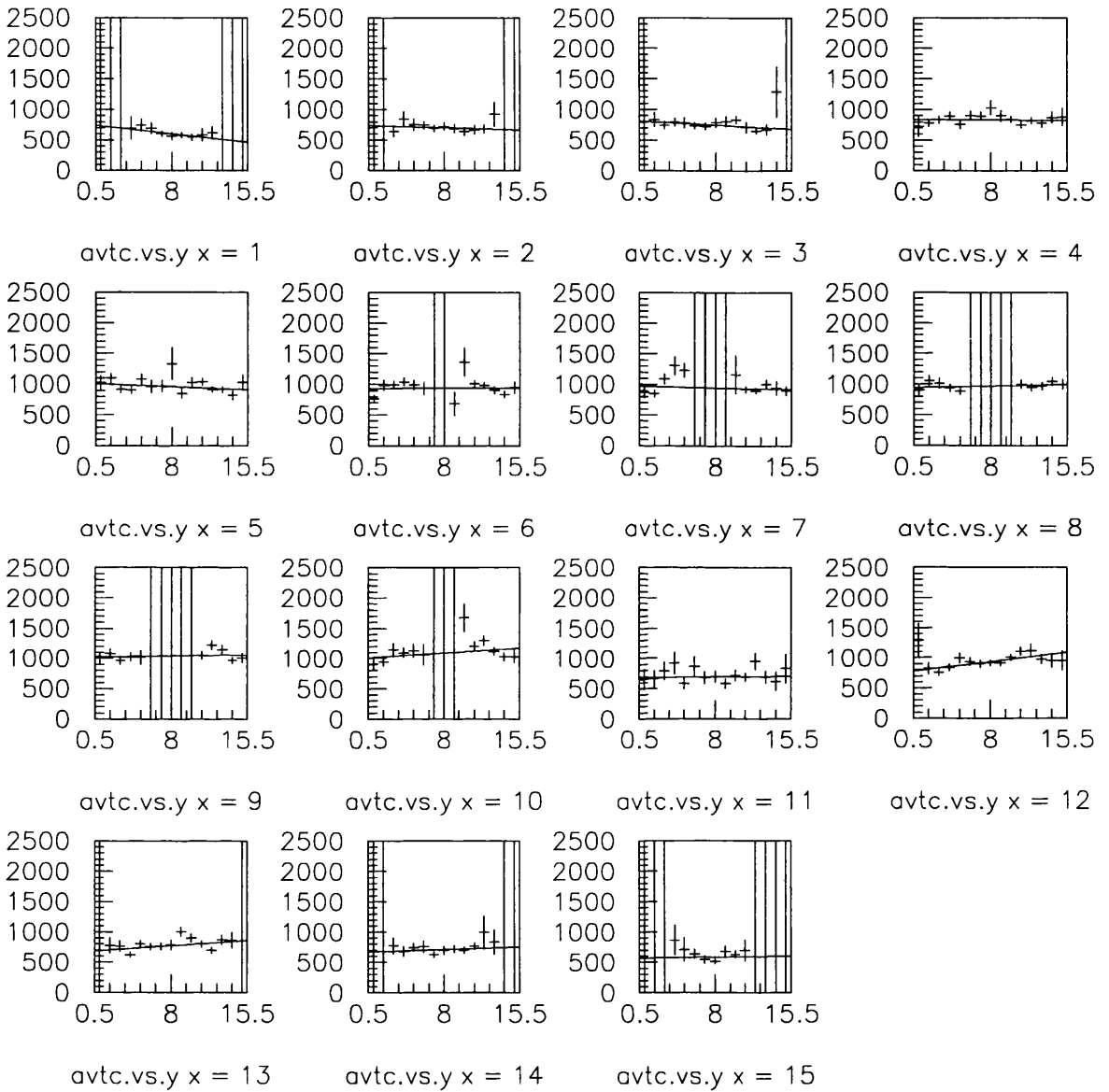


Figure 4.7: Average total charge (avtc) against  $y$  bin for each  $x$  bin TRD2.

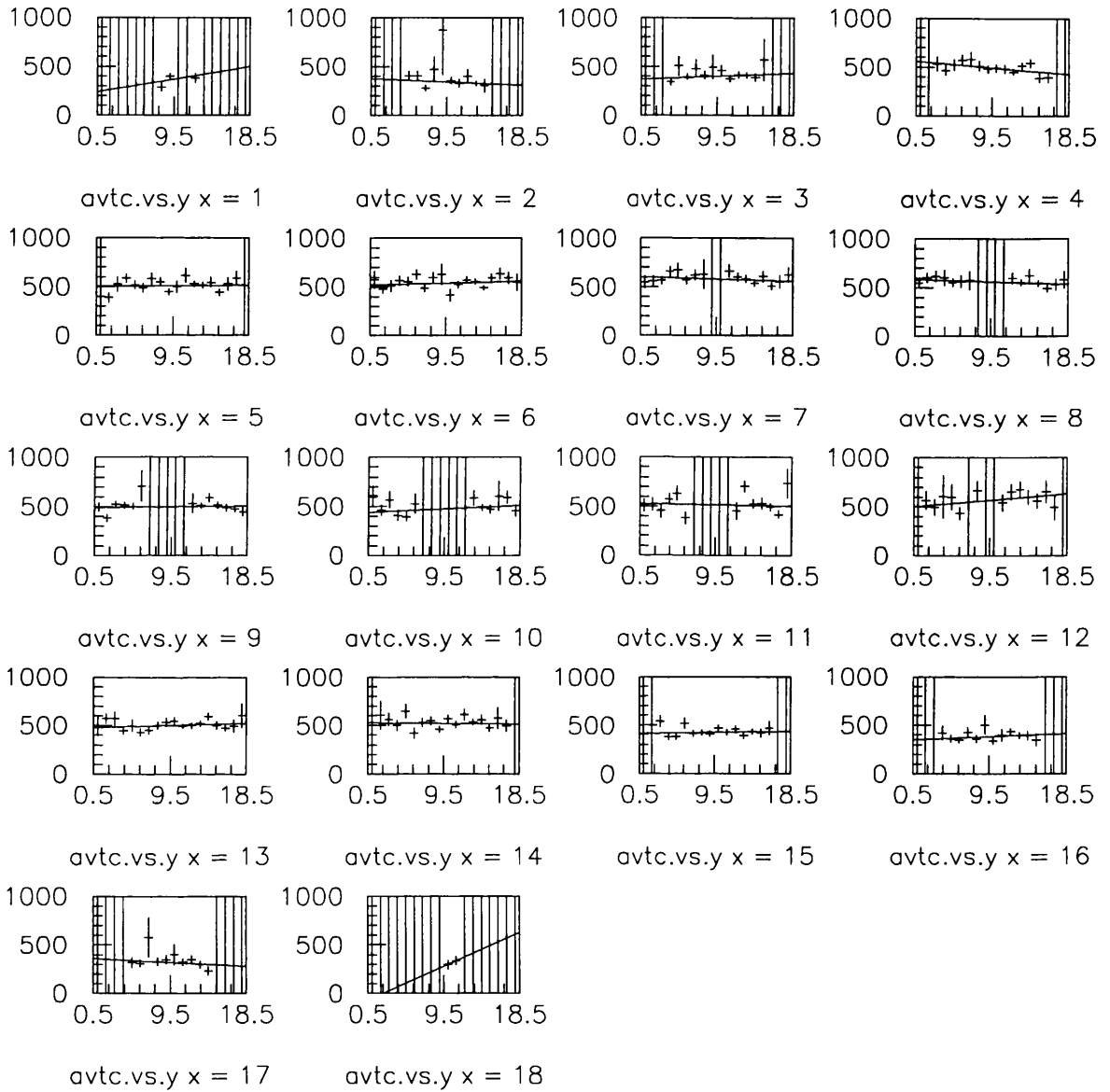
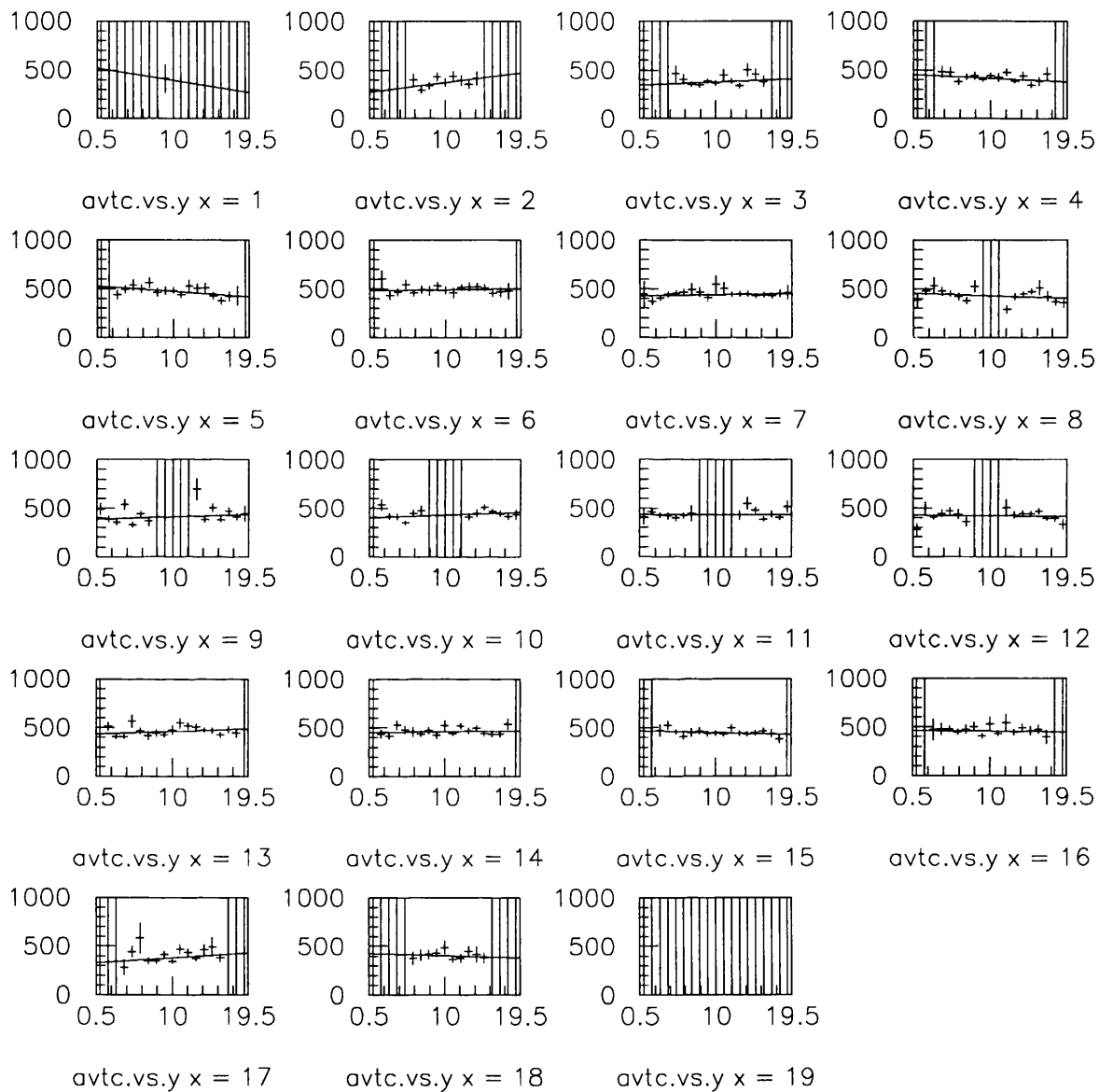


Figure 4.8: Average total charge (avtc) against  $y$  bin for each  $x$  bin TRD3.

Figure 4.9: Average total charge (avtc) against  $y$  bin for each  $x$  bin TRD4.

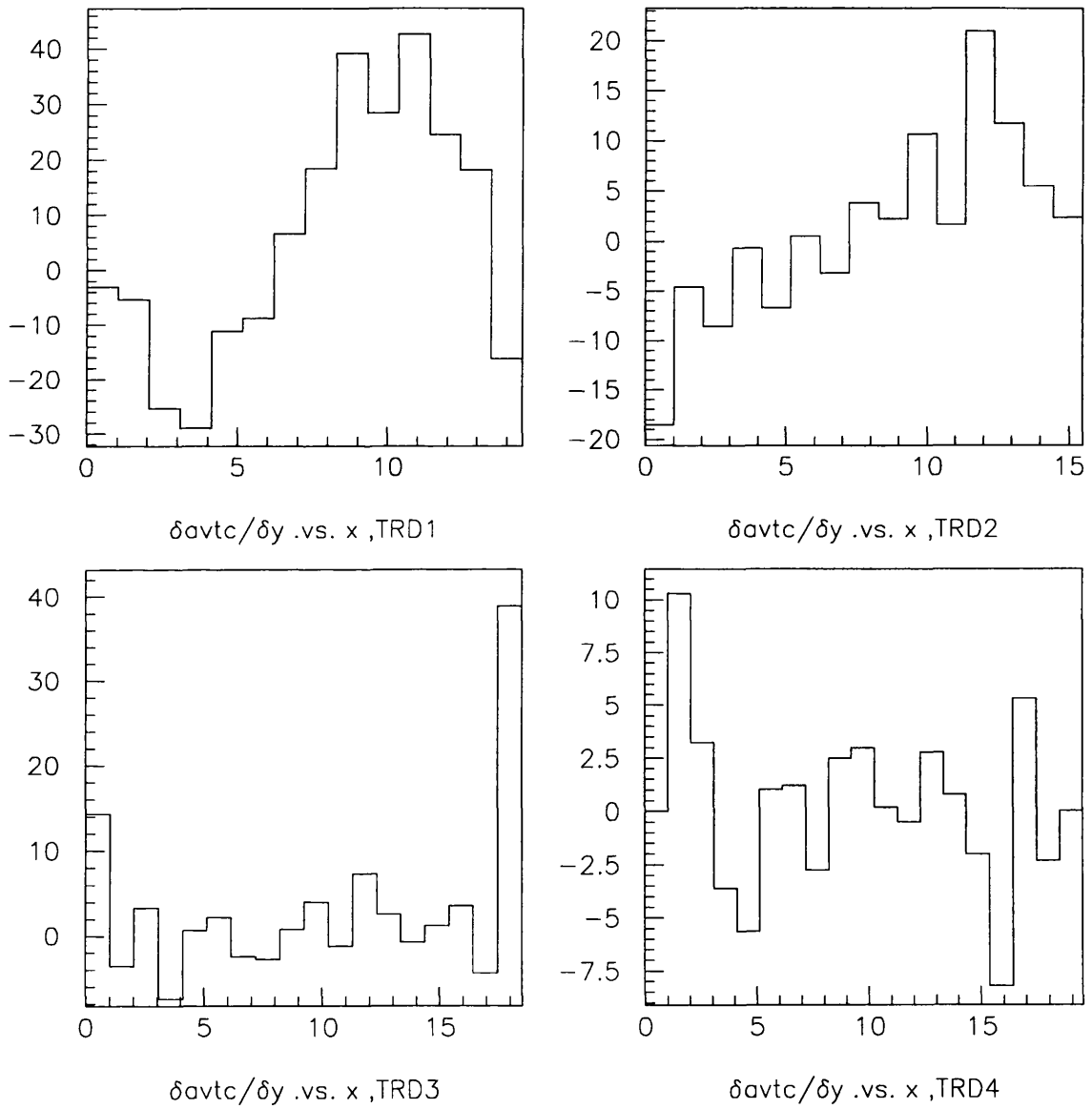


Figure 4.10:  $\delta avtc/\delta y$  plotted against  $x$  bin for each chamber.

### 4.3 The Effect of the Magnetic Field on TRD Data

It was surmised that the observed trends discussed in the foregoing may be due to the large and inhomogeneous magnetic field in the region of the TRD chambers. A very simple model based upon the electromagnetic fields present and the geometry of the chambers was constructed to test this hypothesis.

The behaviour of ionization electrons in a drift chamber may be modelled by the “drift equation” given in equation 4.1, where  $e$  and  $\underline{v}$  are the charge and drift velocity of ionization electrons,  $\underline{E}$  and  $\underline{B}$  the electric and magnetic fields present and  $k$  is a constant characteristic of the drift gas. From equation 4.1 it can be shown that the drift velocity of ionization electrons in TRD chambers one and two has a component in the  $x$  direction given by equation 4.2. Use is made of the fact that, in the region of TRD chambers one and two, the  $x$  and  $y$  components of the magnetic field,  $B_x$  and  $B_y$ , can be approximated by  $\beta x$  and  $\beta y$ ,  $\beta$  being a constant; for chambers three and four,  $B_x$  and  $B_y$  are negligible.

$$k\underline{v} = e\underline{E} + e\underline{v} \times \underline{B} \quad (4.1)$$

$$v_x = \frac{v_z B_x B_z - E_z B_y}{(E_z/v_z)^2 + B_z^2} = \frac{v_z \beta x B_z - E_z \beta y}{(E_z/v_z)^2 + B_z^2} \quad (4.2)$$

$v_x$  can act such that ionization electrons produced in the drift region can arrive on a different signal wire from that which registers the first rise. This decreases the total charge collected on the signal wire recording the hit associated with the first rise.

This effect is dependent upon both the size of  $v_x$  (and hence  $x$  and  $y$ ) and the direction of  $\underline{v}$  relative to the direction of the ionizing particle as shown in figure 4.11. To quantify the effect of such ionization loss on the average total charge at a given  $x$  and  $y$ , the “effective length” of ionization was calculated as a function of  $x$

and  $y$ . The path length of a particle traversing the drift region of a TRD chamber varies over the surface of the chamber, assuming that the particle originates at the interaction point. It was assumed that the level of ionization was constant along this path length (*ie* no account was taken of delta rays or TR photon production) This path length was divided into small sections. For each section, the distance in  $x$  between the ionization electrons and the ionizing particle at the signal wire plane was calculated using the geometry of the chamber and equation 4.2. This distance gave a probability that the ionization would arrive on a different signal wire than the first rise and the appropriate fraction of that “length of ionization” was deemed lost. An effective length of ionization, incorporating these losses and adding in the first rise, was determined for each  $xy$  bin. The results of this model for chamber one are shown in figure 4.12.

The effective ionization length varies with  $y$  for a given  $x$ . On the  $-x$  side of the chamber the effective length of ionization decreases with increasing  $y$ ; on the  $+x$  side of the chamber the effective length of ionization increases with increasing  $y$ . The magnitude of this effect is smaller towards the centre of the chamber than toward the edges of the chamber. Similar results were obtained for chamber two. These general trends are in agreement with those seen in the measured “gain maps” (figures 4.6 and 4.7) suggesting that the variations in total charge observed in the data are indeed due to the effects of the magnetic field.

## 4.4 Conclusions

The response of each of the four TRD chambers has been successfully mapped over its surface. That the response of chambers three and four is flat in  $y$  demonstrates that there is negligible attenuation of the signal as it travels to the read out end of the wire. Similarly, no loss of signal is observed for those wires that are joined at the beam hole by printed circuit boards.

No variation in the gas gain due to the bowing of the backplane is seen. The

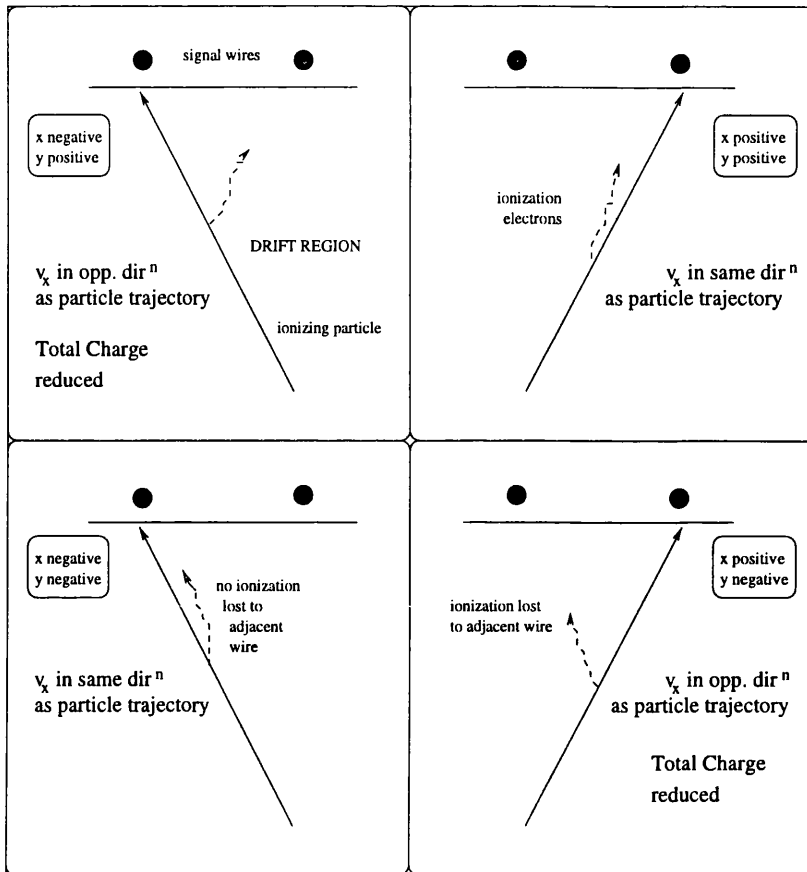


Figure 4.11: Diagram showing how the varying  $x$  component of the drift velocity of ionization electrons leads to a variation in the “effective length of ionization” and hence the collected total charge over the surface of a TRD chamber.

possibility of significant changes in gain around the beamhole due to this effect cannot, however, be discounted as the gain maps obtained do not cover the area immediately around the beam hole due to the lack of CTD tracks in that region.

A definite effect has been observed in chambers one and two, by which the response of the chambers in a given  $x$  bin is a function of  $y$ , the slope of which varies with  $x$ . A model was constructed that describes the trends seen in the data, demonstrating that this effect can be accounted for if one considers the effect of the ZEUS magnetic field upon the drift velocity of ionization electrons in the chamber.

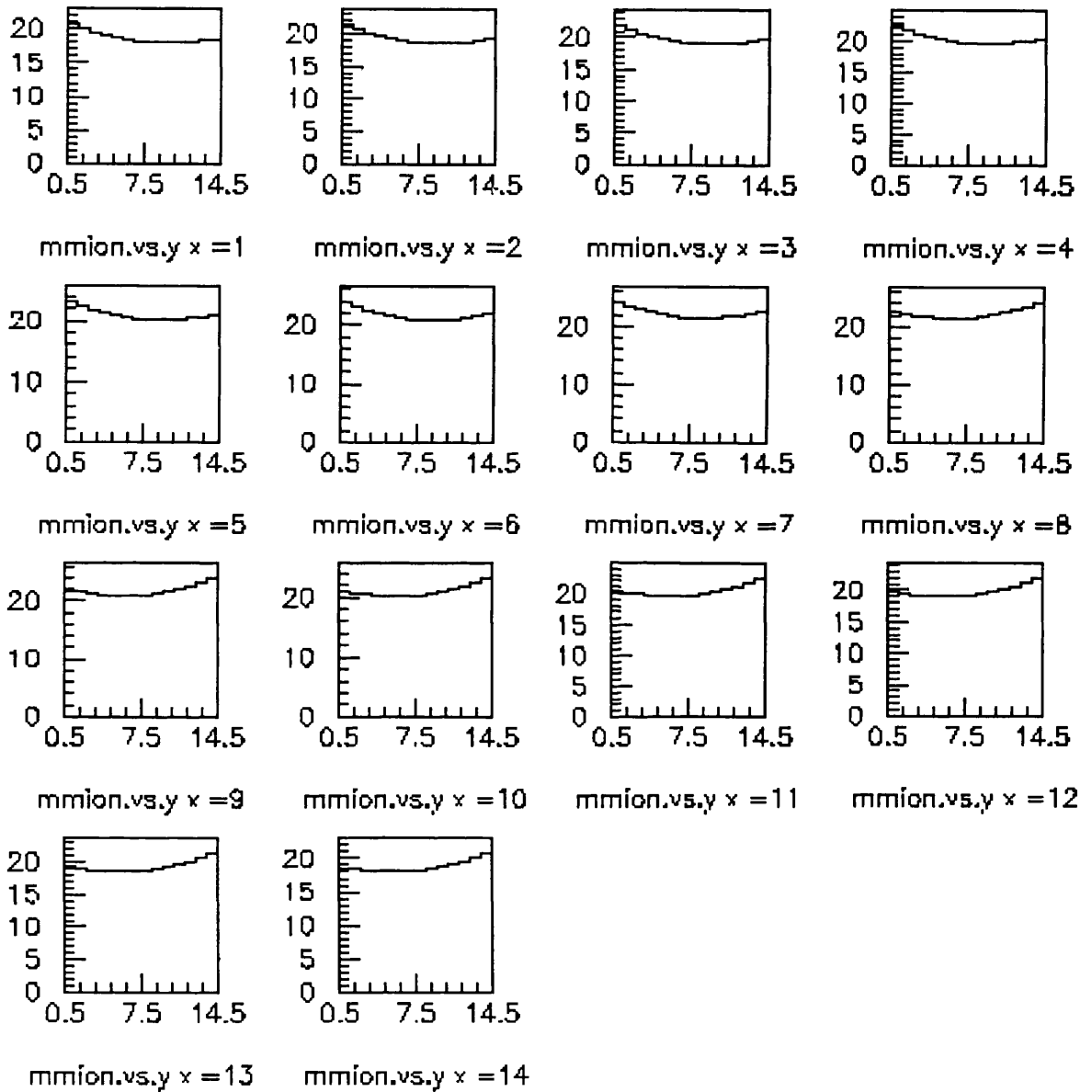


Figure 4.12: The “effective length of ionization” (in mm) against  $y$  bin for each  $x$  bin calculated for TRD1 using the model described in section 4.3.

# Chapter 5

## Event Simulation

The discussion of direct and resolved photoproduction introduced in chapters 1 and 2 is now resumed. For measurements such as those presented in chapter 7 to be useful in testing QCD predictions they should not depend, as far as possible, on the methods used to obtain them; it is essential to understand any systematic errors introduced and correct the raw data for effects of the detector acceptance, response and resolution on physical distributions if one is to interpret measured distributions in terms of underlying physical processes.

This is achieved through the creation and study of mock data known as Monte Carlo events. The production of Monte Carlo hard photoproduction events involves several distinct processes. Figure 5.1 is a schematic diagram showing the stages involved in the production of a resolved hard photoproduction event.

A probability driven “event generator” determines the class of hard scatter ( $qg \rightarrow qg$ ,  $gg \rightarrow gg$ ,  $qq \rightarrow qq$ , ..), and the kinematics of the event. The event generator also governs the transformation of the system of outgoing partons into a system of hadrons (hadronization).

The response of the detector to this hadronic system is then simulated, as is the trigger system. This provides mock data, the form of which is identical to the real data; this can hence be subject to exactly the same reconstruction, selection and analysis processes as the real data.

Information of Monte Carlo events is available at three levels (see figure 5.1):

- “Truth Level” - generated values of quantities such as  $P^2$  and  $y$  that are kinematic variables of the event.
- “Hadron Level” - refers to properties of the generated event as determined from the four-momenta of the produced hadrons such as the jet properties  $\eta_{had}^{jet}$ ,  $\phi_{had}^{jet}$  and  $E_{Thad}^{jet}$ .
- “Reconstructed Level” - values of quantities determined from simulated deposits in the main calorimeter ( $\eta_{cal}^{jet}$ ,  $\phi_{cal}^{jet}$ ,  $E_{Tcal}^{jet}$ ,  $y_{jb}$ ) or in the BPC or LUMI taggers ( $y_e$ ,  $P^2$ ).

By comparing reconstructed level distributions with the analogous truth level or hadron level distributions, it is possible to ascertain the effects on the measured distributions introduced by the detector. These effects can then be accounted for and the raw data corrected.

## 5.1 Event Generators

The first step in simulating an event is to determine the energy and virtuality of the photon, that is to choose values of  $y$  and  $P^2$ .  $y$  is taken from the distribution provided by the Weizsäcker Williams approximation [47] given in equation 5.1 where  $P_\gamma(y)$  is the probability of the electron radiating a photon carrying a fraction  $y$  of the electron energy.  $P_{max}^2$  is a higher cut off, chosen to be 4 GeV<sup>2</sup>;  $P_{min}^2 = (m_e y)^2 / (1 - y)$ .  $P^2$  is then taken from a distribution governed by the  $1/P^4$  dependence of the cross-section and  $P_{min}^2$

$$P_\gamma(y) = \frac{\alpha}{2\pi} \frac{[1 + (1 - y)^2]}{y} \log \left( \frac{P_{max}^2}{P_{min}^2} \right) \quad (5.1)$$

This is not the case for the PYTHIA [48] event generator where the Weizsäcker Williams approximation is used to give a value of  $y$  but where no value of  $P^2$  is

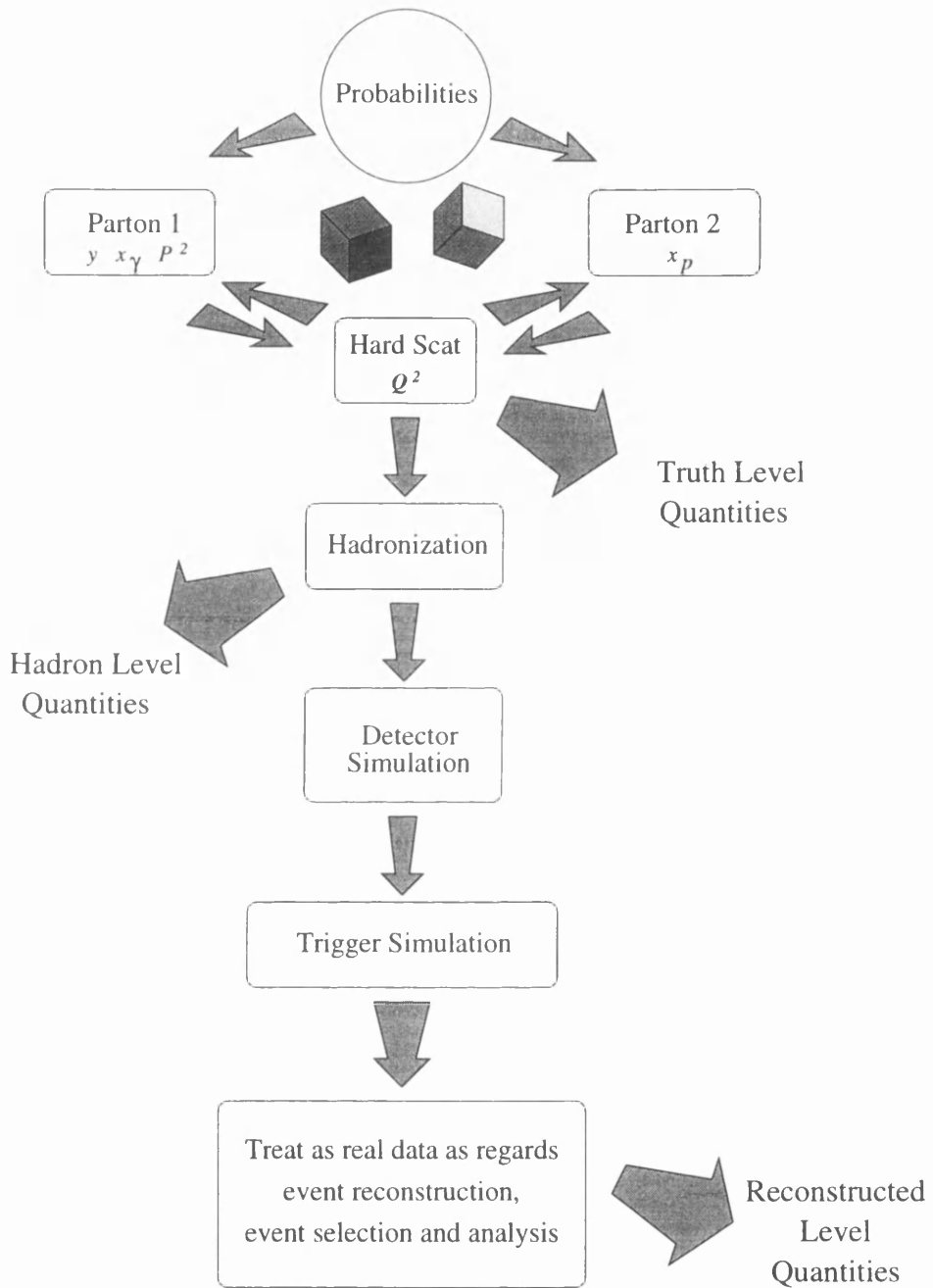


Figure 5.1: A schematic diagram showing distinct stages in the generation of Monte Carlo events.

generated and the scattered positron is assumed to continue in the  $-z$  direction undeflected [49], rendering PYTHIA unsuitable for use in correcting the tagged data presented in this thesis.

The leading order cross-sections for each subprocess are calculated and stored within the program package and a subprocess and scale are chosen according to cross-section weighted probabilities. As mentioned in chapter 1, the cross-section for dijet production can be factorized into a term relating to the parton-parton scattering amplitudes and one pertaining to the parton distributions within the proton and photon (see equation 1.19). The MRSA [7] pdf for the proton and the GRV [26] pdf for the photon were chosen to provide the incoming partons for the hard scatter. These pdf's were chosen as they give the best description of ZEUS data [10][19]. Figures 5.2 and 5.3 show the quark and gluon distributions of these parametrizations within the  $x$  ranges of interest to this thesis at a probing scale  $Q^2 = 25 \text{ GeV}^2$ .

A recent study of the effect of photon virtuality on real photon pdf's and the consequences for the relative contributions of resolved and direct processes is discussed in section 5.2.

Two event generators, PYTHIA and HERWIG [50], were used for the purposes of this thesis. The exact choice of scale differs for PYTHIA and HERWIG. PYTHIA uses the transverse momentum of the outgoing partons  $Q^2 = 1/2[(p_{T1} + m_1)^2 + (p_{T2} + m_2)^2]$  as the hard scale; HERWIG uses  $Q^2 = 2\hat{s}\hat{t}\hat{u}/(\hat{s}^2 + \hat{t}^2 + \hat{u}^2)$  where  $\hat{s}$ ,  $\hat{u}$  and  $\hat{t}$  are the Mandelstam variables. The two packages also differ in their description of the hadronization process. PYTHIA uses the Lund string model [51] whereas HERWIG uses a clustering algorithm [52].

It is desirable that different models are used as the hadronization process is poorly understood; as the corrected data should be free of detector effects, so should the corrections applied to the raw data be free of the influence of assumptions regarding the hadronization process. However, the less than rigorous treatment of the kinematics of the  $e\gamma$  vertex within PYTHIA precludes a study of

the systematic error introduced by the choice of hadronization scheme. PYTHIA was used only to provide the hadron level “jet profiles” presented in section 5.3.

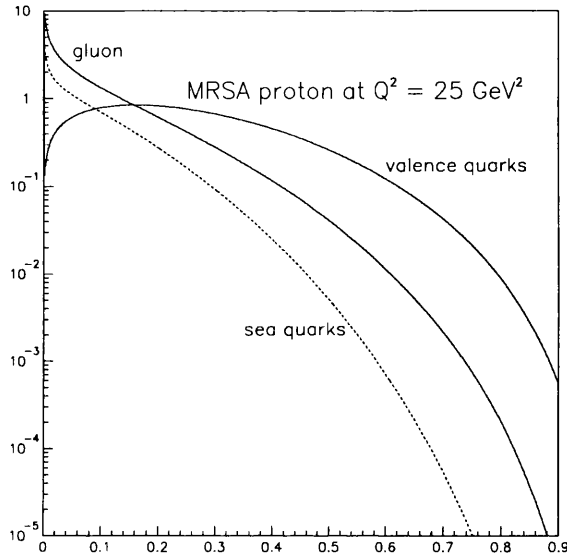


Figure 5.2:  $xP(i, x)$  where  $i = \text{gluon, valence quark, sea quark}$  vs momentum fraction  $x$  for the MRSA proton pdf at a  $Q^2$  of  $25 \text{ GeV}^2$ .

## 5.2 Predictions Using Models of the Virtual Photon

A number of pdf's now exist for virtual photons. The  $P^2$  dependence is implemented in a variety of ways. A purely perturbative treatment, neglecting the VMD component, is presented in [53] whereas the SaS [37] and GRS [38] pdf's combine separate  $P^2$  dependences of the VMD and anomalous components. The SaS1D parton distributions are shown in figure 5.4 for three photon virtualities  $P^2$  at a scale of  $25 \text{ GeV}^2$ .

It has been suggested [36] that one can transform any real photon pdf to a virtual photon pdf by multiplying the quark distributions by a factor  $r$  given in

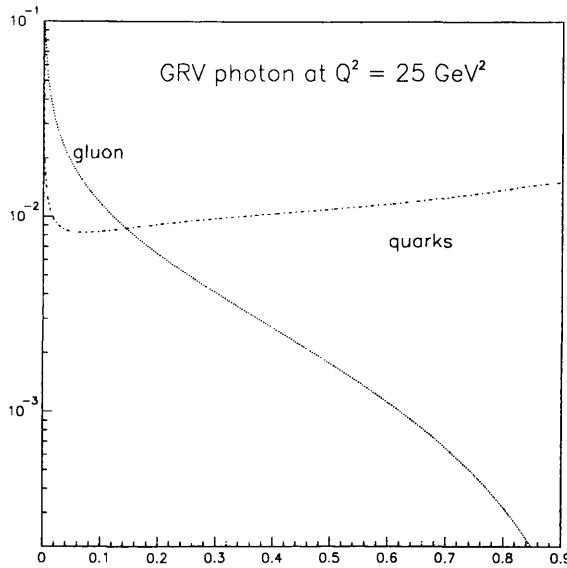


Figure 5.3:  $xP(i, x)$  where  $i = \text{gluon, quark}$  vs momentum fraction  $x$  for the GRV photon pdf at a  $Q^2$  of  $25 \text{ GeV}^2$ .

equation 5.2 where  $P_c^2$  is a typical hadronic scale; a factor of  $r^2$  is prescribed for the gluon.

$$r = 1 - \frac{\ln(1 + P^2/P_c^2)}{\ln(1 + Q^2/P_c^2)} \quad (5.2)$$

The ratio of the resolved and direct contributions to the dijet cross-section has recently been calculated as a function of the  $P^2$  for four parametrizations of the virtual photon [54]. These calculations are compared to the measurements presented in this thesis in chapter 8.

### 5.3 Jet Profiles and Multiple Interactions

In resolved photoproduction there is a remnant jet associated with the photon as well as a remnant jet associated with the proton. There is no reason why a parton from the photon remnant may not be involved in an additional hard scatter with

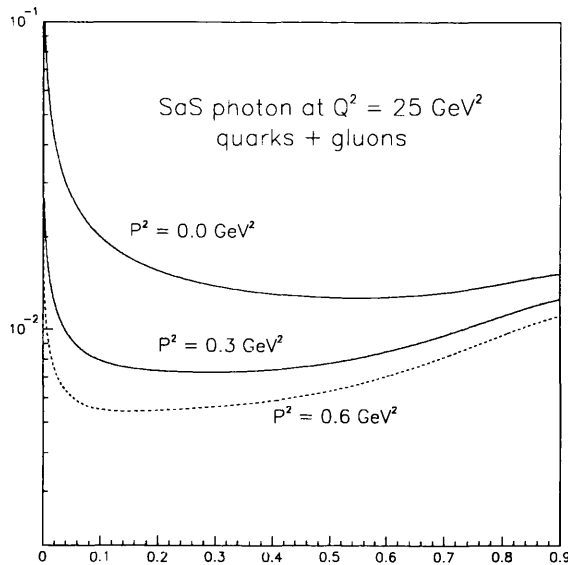


Figure 5.4:  $xP(i, x)$  where  $i = \text{gluon or quark}$  vs momentum fraction  $x$  for the SAS1D photon pdf at a  $Q^2$  of  $25 \text{ GeV}^2$  for 3 different photon virtualities.

a parton from the proton remnant as depicted in figure 5.5. Models that allow such “multiple interactions” give a better description of the data than models that exclude the possibility [55].

In addition to the possibility of further hard interactions there is the possibility of soft, non-perturbative interactions between the two remnants. Such interactions could provide a “soft underlying event” upon which the hard parton-parton scatter is superposed.

Models of multiple interactions are an optional feature of both PYTHIA and HERWIG. One of the main effects of multiple interactions, as implemented in these models, is to increase the flow of transverse energy outside the jets. This effect can be investigated through the study of jet profiles.

The  $E_T$  distribution in  $\eta\phi$  space for a two jet event is shown in figure 5.6. Jet profiles are a means of quantifying the  $E_T$  flow in such events and can be constructed at both hadron level and reconstructed level. The profile in  $\eta$  is the

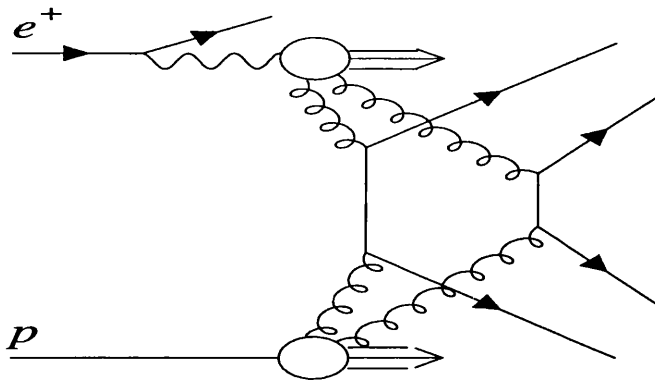


Figure 5.5: In resolved photoproduction events, additional hard scatters can take place between partons from the photon and proton remnants.

$E_T$  weighted distribution of  $\Delta\eta = \eta_{cell} - \eta_{jet}$  for hadrons/cells within 1 rad in  $\phi$  of the jet centre, the  $\phi$  profile the  $E_T$  weighted distribution of  $\Delta\phi = \phi_{cell} - \phi_{jet}$  for hadrons/cells within one unit of rapidity of the jet centre. Figure 5.7 is a representation of a plan view of a two jet event showing the definition of the variables  $\Delta\eta$  and  $\Delta\phi$ .

Hadron level jet profiles obtained using PYTHIA with and without multiple interactions are shown in figure 5.8. The effect of multiple interactions is most clearly observed at the shoulder at positive  $\Delta\eta$  in figure 5.8 (a).

### 5.3.1 $P^2$ Dependence of MI

As is illustrated in figure 2.3, the photon remnant in the anomalous case is “cleaner” than the remnant in the VMD case; the remnant in the VMD case is similar to the proton remnant, a mess of sea quarks and soft gluons. It has been suggested [56] that if the VMD component were to be suppressed with

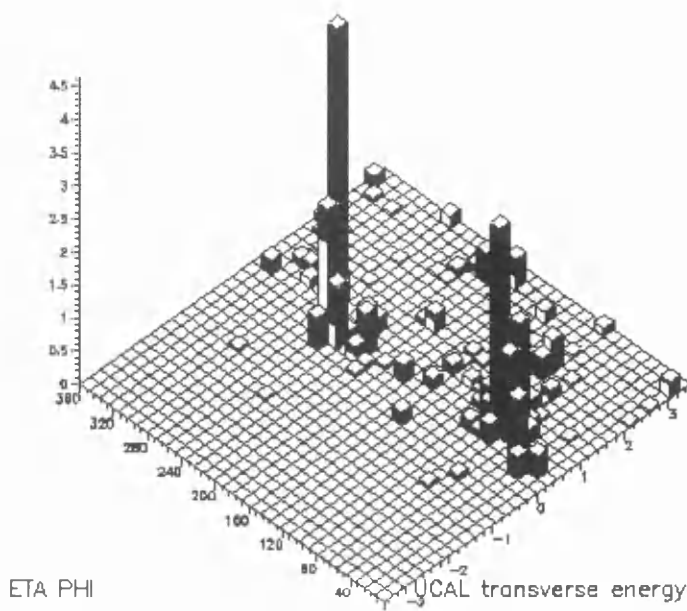


Figure 5.6: The distribution of transverse energy in  $\eta\phi$  space for a two jet event.

respect to the anomalous component then the level of multiple interactions (if present at all) would decrease due to this change in the nature of the remnant. This hypothesis is discussed in the next chapter in the context of jet profiles from the LUMI tagged and BPC tagged samples.

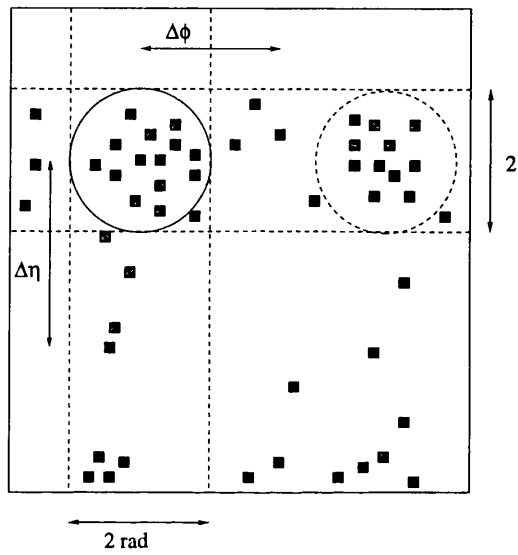


Figure 5.7: A representation of the distribution of hadrons within a two jet event in  $\eta\phi$  space. The black squares represent the jet centre and the hadrons/cells used to define  $\Delta\eta$  and  $\Delta\phi$ . The dotted lines show the bands in  $\eta$  and  $\phi$  within which hadrons/cells contribute to the profile in  $\phi$  or  $\eta$  respectively.

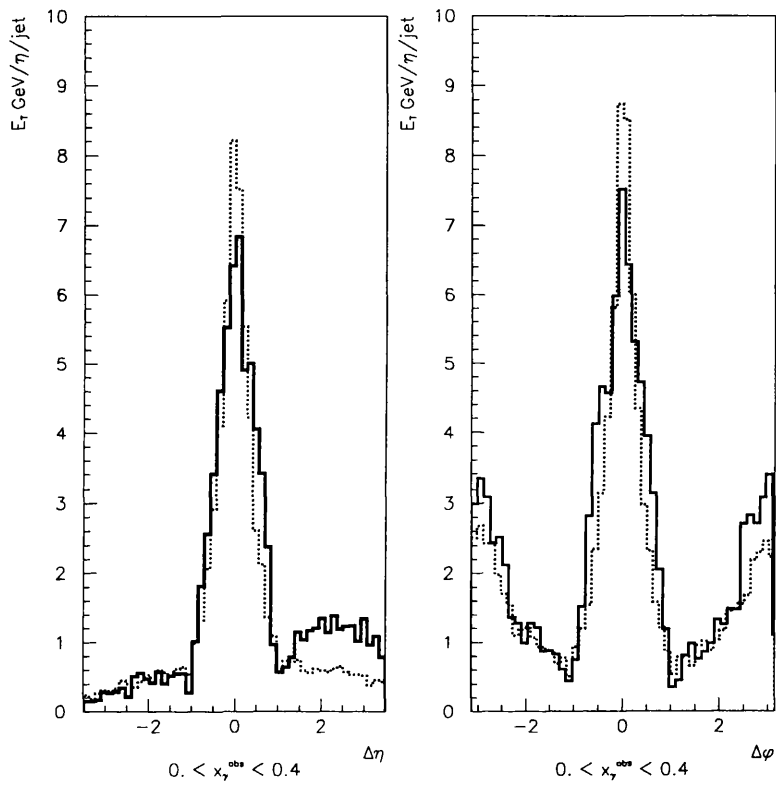


Figure 5.8: Hadron level jet profiles in both a)  $\eta$  and b)  $\phi$  for events generated by PYTHIA both with (dashed) and without (dotted) multiple interactions.

# Chapter 6

## Event Selection

*The wonderful thing about Triggers is that Triggers are wonderful things*

apologies A.A. Milne

### 6.1 The ZEUS Pipeline and Trigger System

#### 6.1.1 Overview

At HERA there is a possible interaction every 96 ns; information can be written to tape at a rate of five events per second. This disparity necessitates a method for deciding which events should be stored for future analysis and which events should be rejected.

A decision must be made as quickly as possible as room must be made for new events but the system should also be sophisticated enough to determine not only if the event is a genuine  $ep$  event but also what kind of  $ep$  event it is. The latter requirement is essential as the rate for genuine  $ep$  collisions,  $\approx 200$  Hz at the design luminosity of  $1.5 \times 10^{31} \text{ cm}^{-2} \text{ s}^{-1}$  [57], greatly exceeds the 5 Hz rate at which events can be stored. One needs to accept only a fraction of the physics processes that dominate the total cross-section.

The three stage ZEUS trigger satisfies these requirements. Figure 6.1 is a schematic diagram of the flow of information through the trigger system.

A very fast ( $5\mu\text{s}$ ) decision is made by the first level trigger (FLT) which reduces the data flow by a factor of one hundred. This increases the time that the second level trigger (SLT) has to accept or reject each event such that a more refined set of criteria can be applied. There are also more data available at this stage. The SLT reduces the rate by a further factor of ten.

The full data from each component is then combined (event builder) and passed to the third level trigger (TLT) where a further reduction in rate is achieved. Chosen events are then written to tape.

Whilst the FLT decision is being made, the data is stored in a pipeline along which it is shifted on receipt of a time signal. Accurate timing is necessary such that a trigger decision can be matched to the event to which it refers.

### 6.1.2 Backgrounds to be Removed

As stated in the foregoing, the events that must be rejected by the trigger system fall into the two categories of “non-physics background” and “physics background”.

- Non-physics Background
  - Beam gas interactions

Interactions between the proton beam and residual gas molecules in the beampipe upstream of the detector produce a large number of energy deposits in the calorimeter and a number of tracks in the CTD. The tracks will not however point towards a vertex in the interaction region and the energy in the RCAL is deposited  $\approx 16$  ns before the energy in the FCAL. These properties can be used to identify and reject these events.

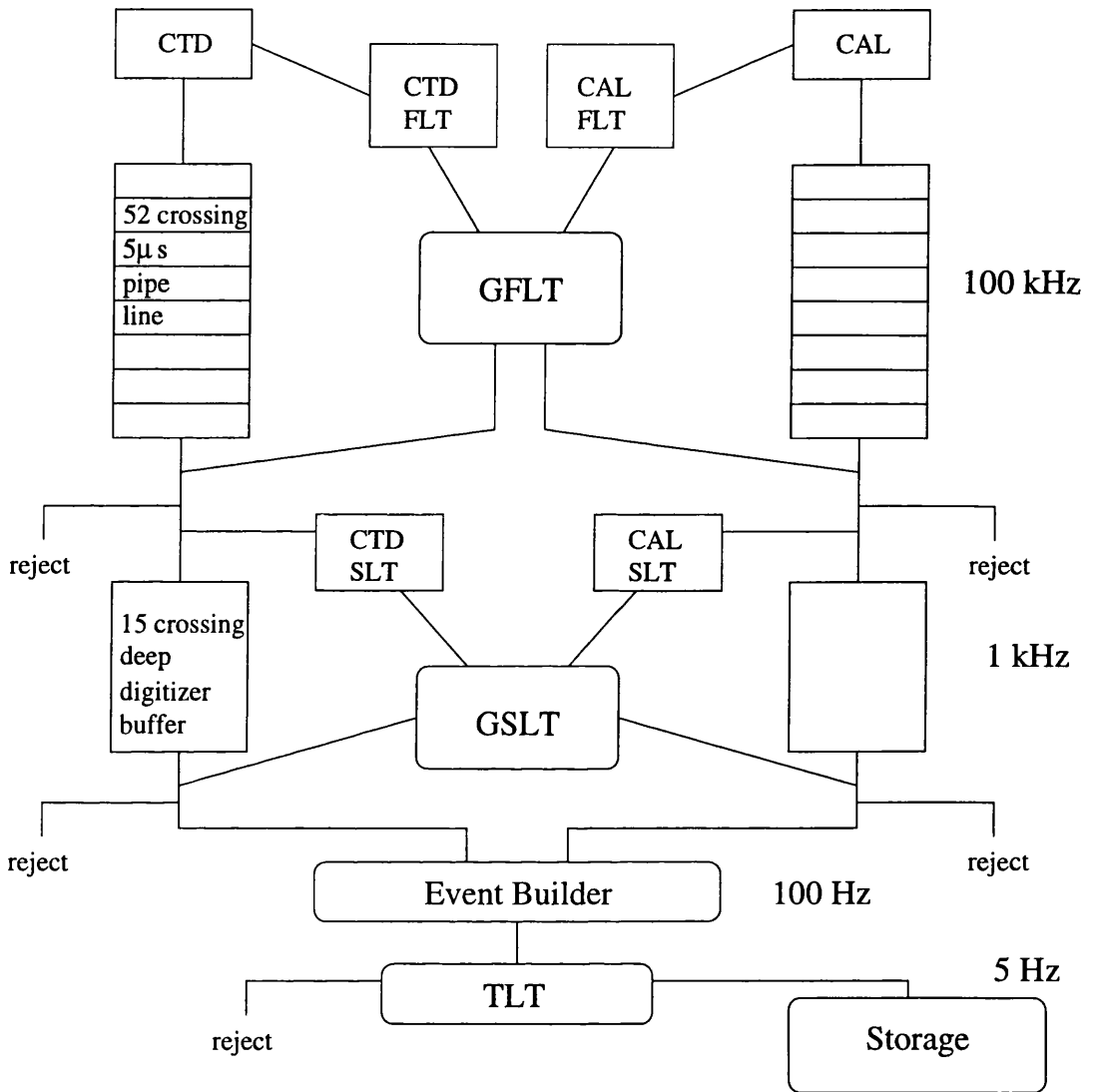


Figure 6.1: A schematic diagram showing the flow of event information through the ZEUS trigger system. For the sake of simplicity, only two subcomponents (CTD and CAL) are shown as contributing to the process. The values on the right hand side of the diagram are approximate rates at which events are processed at that particular stage.

- Cosmic Rays

Cosmic muons traversing the ZEUS detector deposit energy in the barrel calorimeter and leave a single track in the CTD. If a muon passes close to the  $z$  axis in the interaction region, the track could be interpreted as two tracks coming from a vertex and the event mistaken as a genuine  $ep$  collision. The energy deposit in the top half (positive  $y$ ) of the BCAL will arrive earlier than the deposit in the bottom half of the BCAL. This characteristic can be exploited for the rejection of these events.

- Physics background

The  $ep$  cross-section is dominated by photoproduction events (see Chapter 1). This thesis concentrates on hard parton-parton scattering in photoproduction events (hard photoproduction). The vast majority of photoproduction events are, however, “soft” in that there is no hard energy scale present. Studies of soft photoproduction are by no means limited by statistics and it is desirable that only a small fraction of these events is written to tape. It is important that this small fraction is known in order to calculate the total  $ep$  cross-section for example. These events must therefore be identified as  $ep$  events before being discarded. The process of accepting a known fraction of a certain type of event is called “prescaling”. The level of prescaling can be altered giving a flexible system that can respond to changes in luminosity.

### 6.1.3 First Level Trigger

The global first level trigger (GFLT) rejects events based on information from the local subcomponent FLT’s. These make simple calculations based on the first data to emerge from the subcomponent electronics. The CTDFLT, for instance, receives readout from the wires equipped with “z-by-timing” (see chapter 3). By

matching hits in  $rz$  and assuming a vertex at  $z = 0$ , the CTDFLT can count the number of “vertex tracks” defined as those which point toward some specified window in  $z$ . Independently, it matches hits in  $r\phi$  and counts the number of “ $r\phi$ ” tracks. The ratio of vertex tracks to  $r\phi$  tracks provides a criterion upon which the GFLT may reject beam gas events.

From the calorimeter first level trigger (CALFLT), the GFLT has information on the  $E_T$  in an event and on the missing  $E_T$ . Missing  $E_T$  can be used to identify possible charged current events.

#### 6.1.4 Second Level Trigger

By the time that events reach the SLT, more information is available upon which to base a decision. For instance, the CTDFLT only receives information from the “ $z$ -by-timing” system whereas the whole of the CTD data is available to the CTD SLT. The calorimeter timing is used to reject events from beam gas interactions. These will have a large value of  $(t_f - t_r)$  where  $t_f$  and  $t_r$  are the energy weighted average times for the forward and rear calorimeters respectively. A cut on the absolute value of  $t_r$  is also applied.

Calorimeter timing is also used to reject cosmic ray events as these have a large value of  $(t_{up} - t_{down})$  where  $t_{up}$  and  $t_{down}$  are the energy weighted average times for the upper and lower halves of the calorimeter.

The beam gas background is further suppressed by applying a cut on the total  $E - p_z$  of the event, there being a maximum  $E - p_z$  for an  $ep$  collision of twice the electron beam energy.

CTDSLTL can provide a rudimentary vertex which can eliminate beam gas events but this is only used in instances where there is not enough energy in the RCAL to apply any timing cuts.

### 6.1.5 Third Level Trigger

The SLT has a pass rate of  $\approx 100$  Hz. The subcomponent data for these events are combined and passed to the TLT which has time enough to select events on a reasonably sophisticated set of criteria.

The full CTD tracking algorithm is run on a subset of superlayers, giving an event vertex and the number of bad-vertex tracks, defined in chapter 3. Events are rejected by the TLT if:

- $|z_{vertex}| > 75$  cm
- No. of bad-vertex tracks  $> 5$
- $|t_f - t_r| > 8$  ns,  $|t_r| > 8$  ns or  $|t_f| > 8$  ns

A jet finding algorithm similar to the one described in section 6.1.6 is applied to the calorimeter cells, as is a rudimentary electron finding algorithm. Figure 6.2 shows a schematic diagram of the hard photoproduction trigger filter which is applied in addition to the GFLT and GSLT cuts described above. This provides several “branches” of events that are of interest to those studying hard photoproduction. All SLT branches can contribute to the TLT exit branches consisting of events with found jets labelled “1 jet” and “2 jet” in figure 6.2. The events used in the analysis presented in this thesis came through the LUMI or BPC SLT branches and the TLT 2 jet branch. These branches were not prescaled.

### 6.1.6 Jet Finding - Cone Algorithm

Interpreting data in terms of the QCD processes described in chapter 1 relies upon associating the outgoing partons of hard processes with the system of hadrons measured by the detector.

Both at TLT and in offline analysis this is done by using a “cone algorithm” [58][59] to identify jets of hadrons that can be associated with partons from the hard scatter.

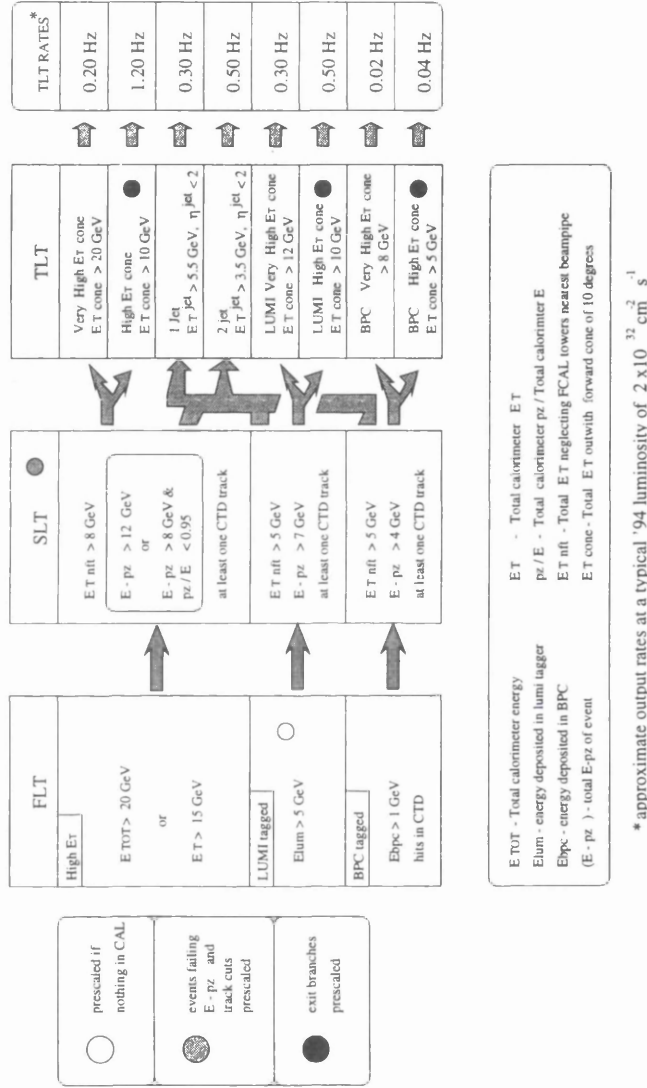


Figure 6.2: A schematic diagram of the hard photoproduction trigger filter. Note that each of the SLT branches can contribute to the TLT jet branches labelled “1 jet” and “2 jet”. Higher

$$E_T^{jet} \text{ thresholds are applied at } \eta^{jet} > 2.$$

The cone algorithm defines jets as being a spray of hadrons contained within a cone of a given radius in  $\eta\phi$  space, the transverse energies of which combine to give a value  $E_T^{jet}$  above some minimum  $E_{Tmin}^{jet}$ .

These are found as a number of calorimeter cells contained within a circle in  $\eta\phi$  space. A radius of one is used.  $\eta\phi$  space is used as the distance between cells in this space is invariant under boosts along the beam axis, such as the boost to the  $\gamma p$  frame in photoproduction. Note that  $E_T$  is also unaffected by such boosts. In a single event, jets found in the lab frame are thereby the same objects that would be found as jets in the  $\gamma p$  frame. At hadron level, the jet finding is hence insensitive to the asymmetry in the beam energies and the varying photon energy. For jet finding in the calorimeter, this statement is tempered only by the changing  $\eta$  resolution of the calorimeter as one moves from  $\eta = 0$ ; the  $\eta$  coverage of a calorimeter cell at  $\eta = 0$  is 0.1 whereas at  $\eta = 2.0$  it is 0.4.

## 6.2 Selecting Tagged Hard $\gamma p$ Events

The sample of events used for the analysis presented in this thesis was chosen from events passed by the TLT HPP filter on the criteria given below.

- Minimum of two jets with  $E_T^{jet} > 4$  GeV in the  $\eta$  range  $-1.125 < \eta^{jet} < 1.875$ 
  - The  $E_T^{jet}$  cut is motivated by the low statistics of the BPC data. A lower limit on the choice of  $E_T^{jet}$  cut is set by the threshold of 3.5 GeV used by the jetfinder at TLT (see figure 6.3)
- No positron candidate found in the main calorimeter with energy  $> 10$  GeV.
- A deposit in either electron tagger giving a photon energy of  $0.2E_e < E_\gamma < 0.6E_e$ .

- The  $y_e$  range is chosen as the region of  $y_e$  overlap between the two electron taggers (see figures 6.4 (a) and (b)).
- The  $y_e$  cuts are used to define the kinematic regime of interest whereas the measurement of  $y_{jb}$  is used to reject background events (see below).
- $0.15 < y_{jb} < 0.70$ 
  - The lower  $y_{jb}$  cut removes residual contamination from beam gas events; DIS events where the scattered positron enters the main calorimeter undetected are removed by the high  $y_{jb}$  cut. This contamination is very slight due to the positive tagging requirement. Figures 6.4 (c) and (d) shows the  $y_{jb}$  distribution for LUMI and BPC tagged events.
- $|t_f - t_r| < 6$  ns (see figure 6.5 (a))
- A reconstructed vertex in the range  $-40\text{cm} < z_{vertex} < 40\text{cm}$ . Figure 6.5 (c) shows the  $z_{vertex}$  distribution of the TLT output studied
- $35\text{GeV} < 2E_e y_{jb} + 2E'_e < 60$  GeV
  - The quantity  $2E_e y_{jb} + 2E'_e$  should peak around  $2E_e$  for a well contained tagged event. Low level backgrounds are removed by this cut (see figure 6.5 (d)).
- For BPC tagged events, only events with  $P^2 > 0.1$  GeV<sup>2</sup> were accepted (see figure 6.6).

Figure 6.5 (b) shows the  $t_u - t_d$  distribution for the events studied. No further cut on this quantity was deemed necessary. The tagging of positrons is discussed in chapter 3, as is the CTD vertex reconstruction.

A total of 271 BPC tagged events and 13351 LUMI tagged events passed the cuts discussed and constitute the event sample used for the analysis presented in chapters 7 and 8.

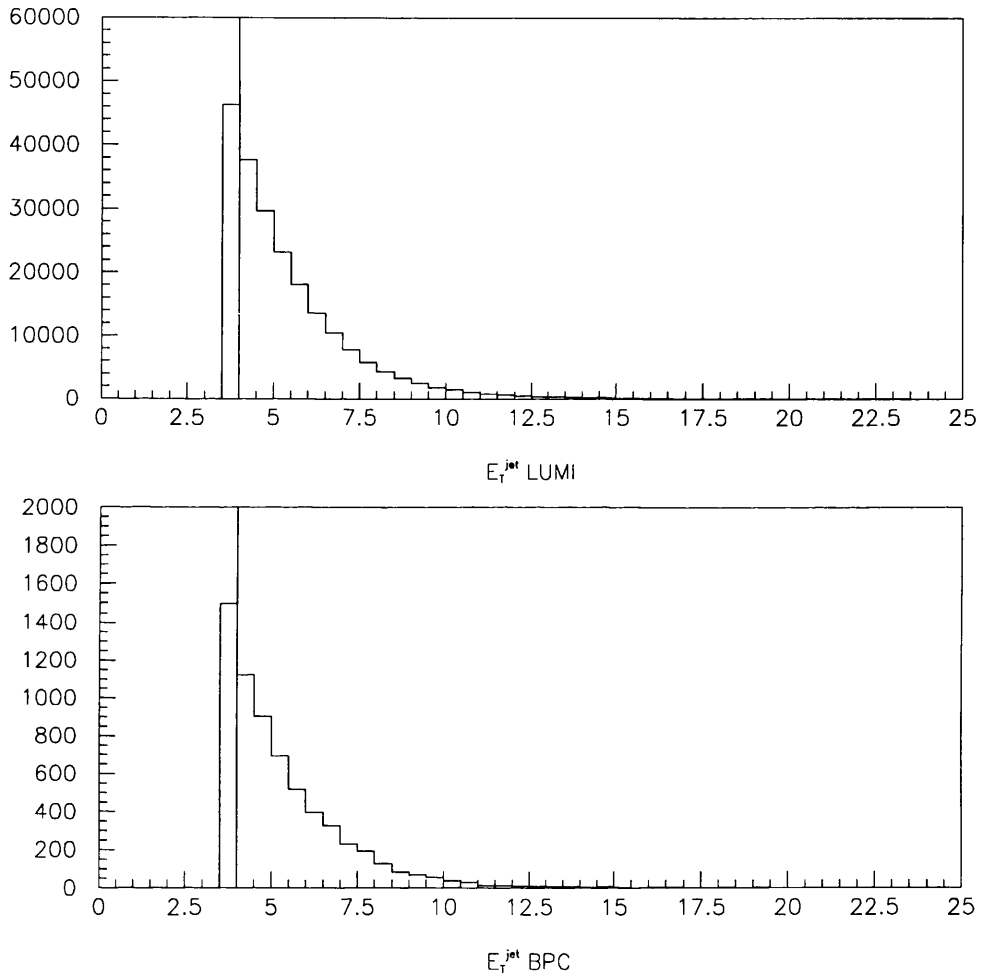


Figure 6.3: The  $E_T$  distribution of jets within  $-1.125 < \eta^{jet} < 1.875$  for LUMI tagged and BPC tagged data before the application of the final analysis cuts. The line shows the cut of 4 GeV applied to  $E_T^{jet}$ .

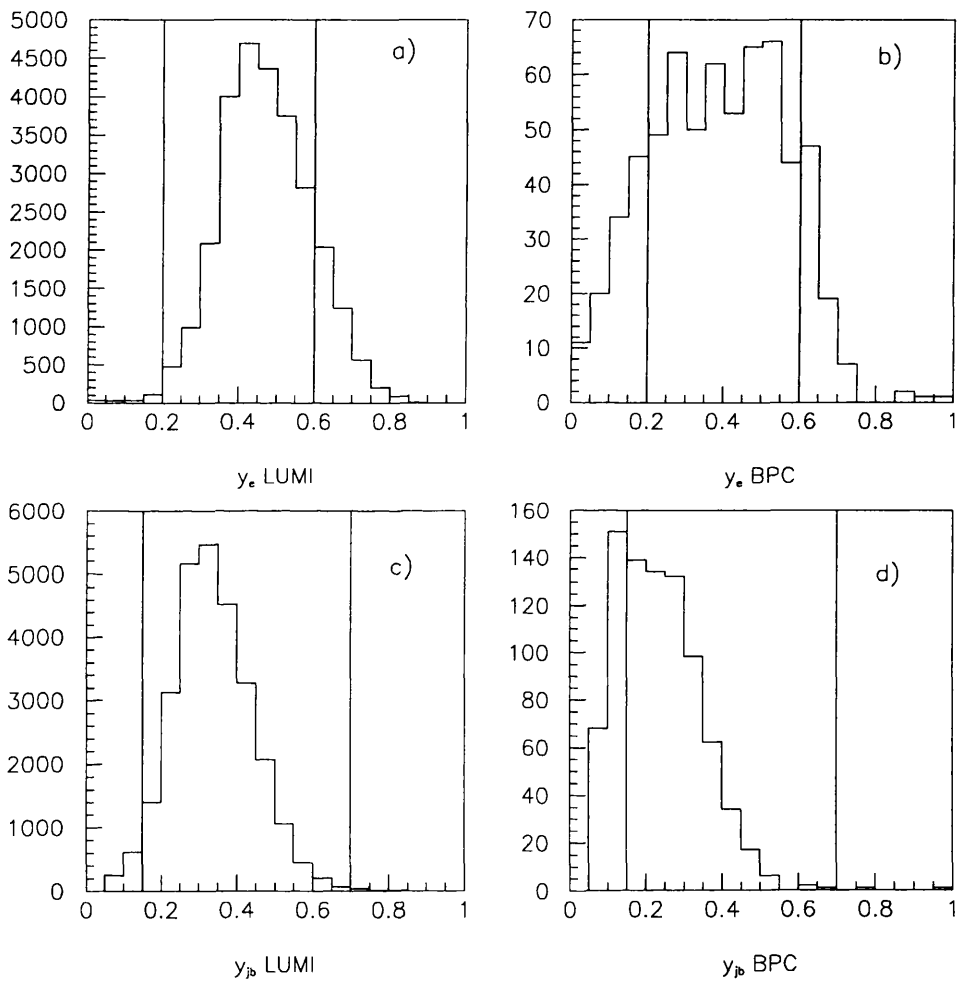


Figure 6.4: The distributions of  $y_e$  and  $y_{j_b}$  for both LUMI tagged and BPC tagged data. The lines show the cuts applied to provide the final event sample.

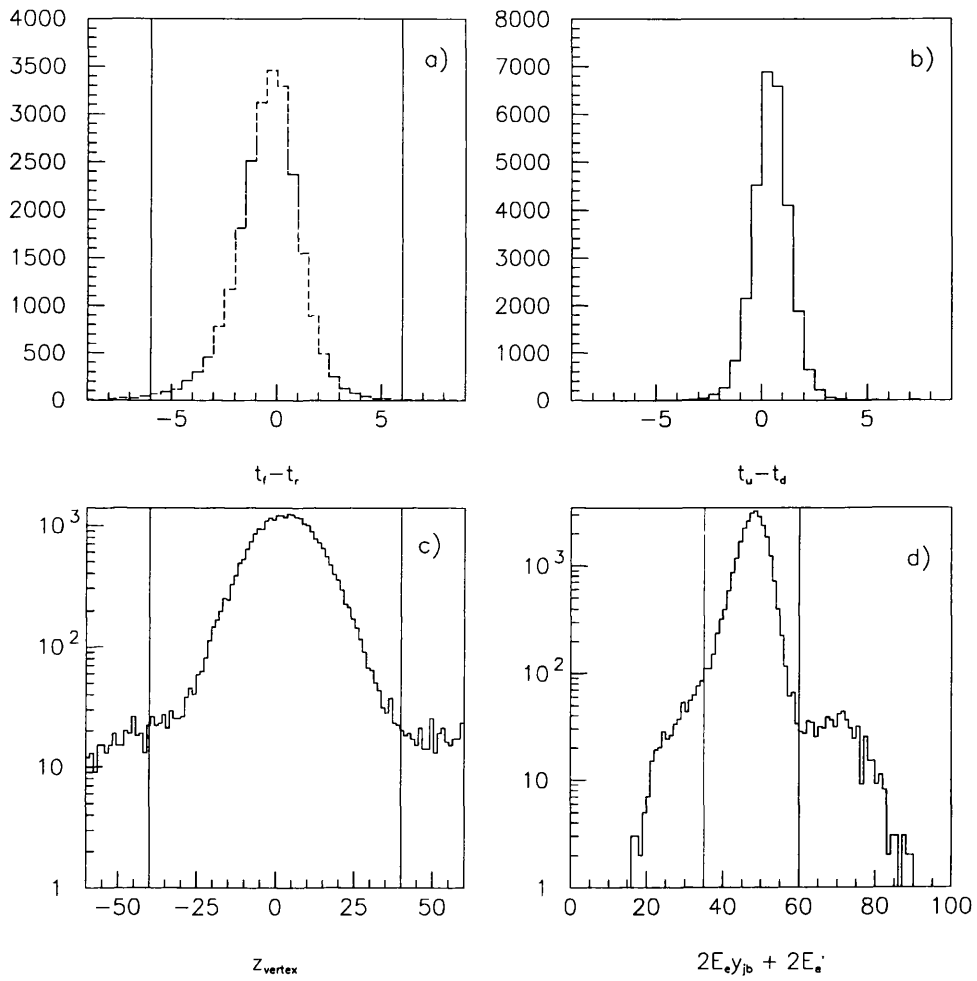


Figure 6.5: The distributions of  $(t_f - t_r)$ ,  $(t_u - t_d)$ ,  $z_{vertex}$  and  $2E_e y_{jb} + 2E'_e$  for the combined LUMI tagged and BPC tagged data. Once more, the lines show the cuts applied to provide the final event sample.

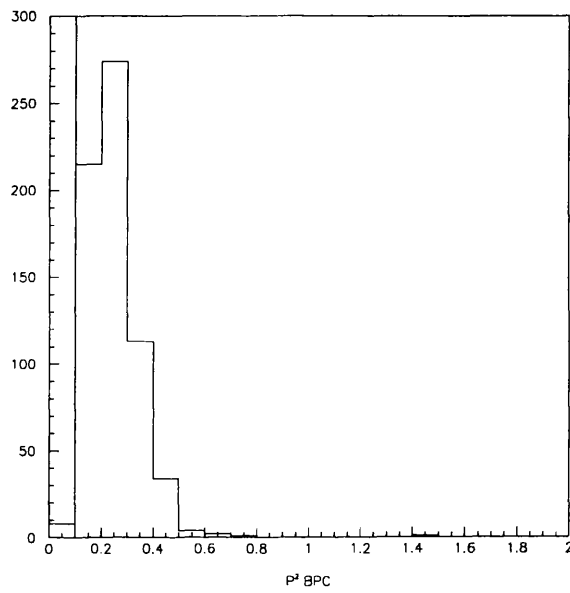


Figure 6.6: The  $P^2$  (GeV<sup>2</sup>) distribution of the BPC tagged data before the application of the final analysis cuts.

# Chapter 7

## Analysis

This thesis studies the  $P^2$  evolution of photon structure by contrasting the distributions of  $x_\gamma^{obs}$ , the fraction of the photon momentum manifest in the two highest  $E_T$  jets, obtained from data tagged by the LUMI tagger and the BPC. This chapter discusses in some detail the analysis of the data samples and the corrections for detector effects applied to the raw data to produce the measurements presented in section 7.8. The uncorrected data are presented, as are the correction techniques, the study of systematic errors and the corrected results. The corrected results are discussed in chapter 8.

### 7.1 The Data

$x_\gamma^{obs}$  is reconstructed through the measurement of  $y$ ,  $E_T^{jet}$  and  $\eta^{jet}$ . The distributions of these quantities are presented in figures 7.1 and 7.2 for the LUMI tagged and BPC tagged events that passed all the cuts described in chapter 6. Figure 7.2 shows both the  $y_e$  distributions obtained using the measurement of the scattered positron energy and the distributions of  $y_{jb}$  obtained from the summed  $E - p_z$  of the main calorimeter cells.

The clear correlation between  $y_{jb}$  and  $y_e$  for LUMI tagged events is shown in figure 7.3 (a).  $y_{jb}$  is systematically lower than  $y_e$  due to energy losses in the dead

material before the calorimeter and the escape of particles down the rear beam pipe. As can be seen in figure 7.3 (b), the inferior energy resolution of the BPC -  $28\%/\sqrt{E}$  contrasted with  $15\%/\sqrt{E}$  for the LUMI tagger (see chapter 3) - makes the  $y_{jb} - y_e$  correlation less clear for the BPC tagged data.

As mentioned in chapter 6, the total  $E - p_z = 2E_e y_{jb} + 2E'_e$  of an event should approximate  $2E_e = 55.04$  GeV if the event is a genuine and well contained tagged photoproduction event. The tagged data peaks at less than  $2E_e$  due to the systematically low measurement of  $y$  using  $y_{jb}$ . Figures 7.3 (c) and (d) show the  $2E_e y_{jb} + 2E'_e$  distributions for the LUMI and BPC tagged samples. The inferior energy resolution of the BPC is evident again in the wider peak of the BPC  $2E_e y_{jb} + 2E'_e$  distribution compared to the LUMI tagged data. The fact that the two distributions peak in the expected region clearly indicates that both samples are formed of genuine tagged events.

The  $z_{vertex}$  distribution of the combined data sample is presented in figure 7.4 along with the calorimeter timing differences. These distributions have the expected shape for a sample of genuine  $ep$  collisions; contamination from beam gas or cosmic muons would manifest itself as tails in these distributions. The  $P^2$  distribution of the BPC tagged data is shown in figure 7.4 (d). This reflects the  $P^2$  acceptance of the device and the  $1/P^4$  dependence of the  $ep$  cross-section.

## 7.2 Resolutions

From simulated Monte Carlo events, the accuracy with which the ZEUS detector is able to measure  $y_e$ ,  $y_{jb}$  and  $P^2$  was obtained by comparing the truth level and reconstructed level values of these quantities. The results of these studies are presented in figure 7.5.

To determine the effect of the ZEUS detector upon the properties of jets the jet finder is run on the final state hadrons before detector effects are accounted for. This provides hadron level values of  $E_T^{jet}$ ,  $\eta^{jet}$  and, using  $y_{tru}$ ,  $x_\gamma^{obs}$ .

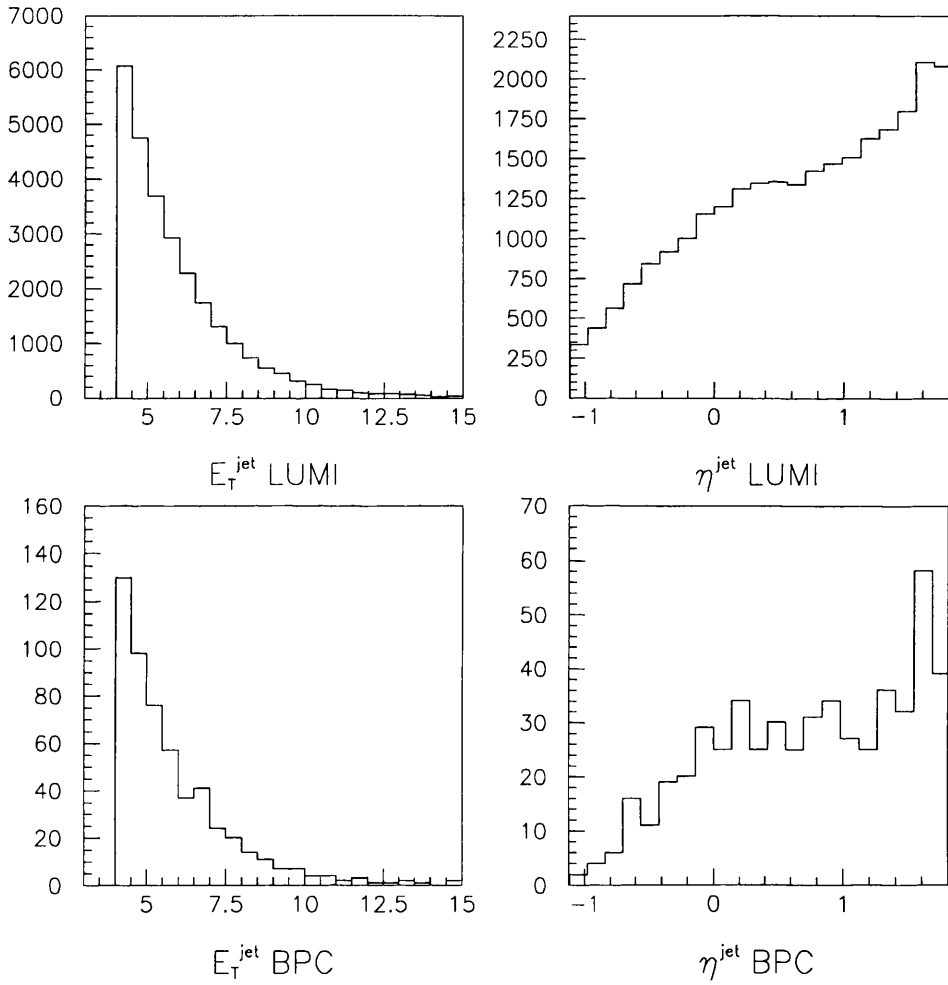


Figure 7.1: The  $E_T^{\text{jet}}$  and  $\eta^{\text{jet}}$  distributions for the LUMI tagged and BPC tagged data samples.

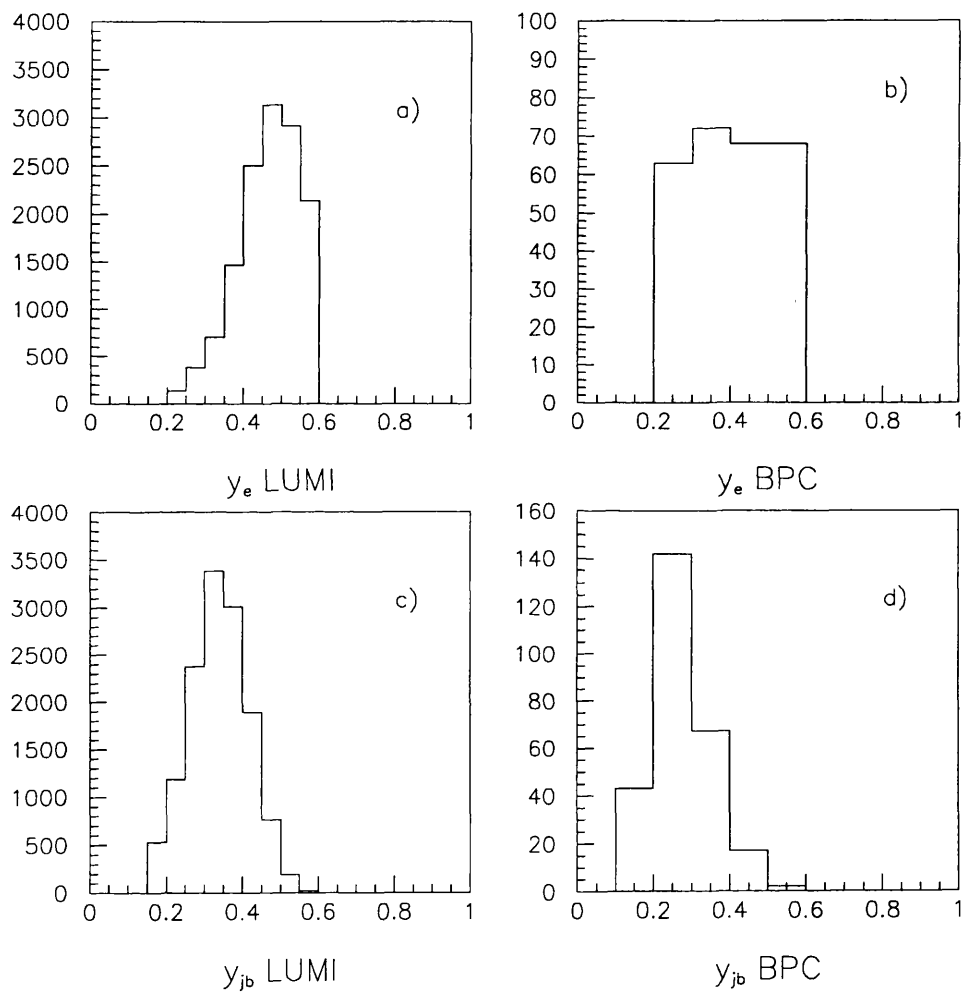


Figure 7.2: The distributions of  $y_e$  and  $y_{jb}$  for the data samples tagged by the LUMI and the BPC.

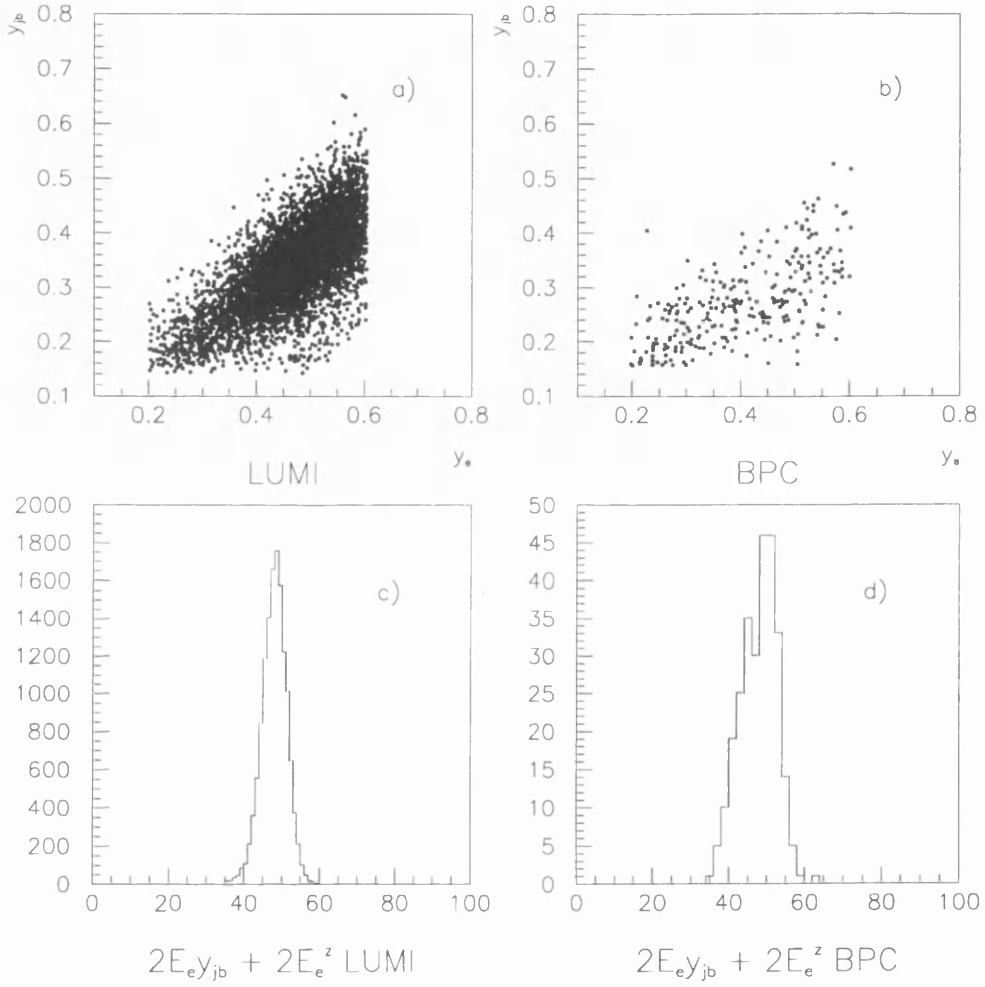


Figure 7.3: Scatter plots of  $y_{jb}$  vs  $y_e$  ((a) and (b)) and the distributions of the quantity  $2E_e y_{jb} + 2E_e^2$  ((c) and (d)) for both LUMI and BPC data samples.

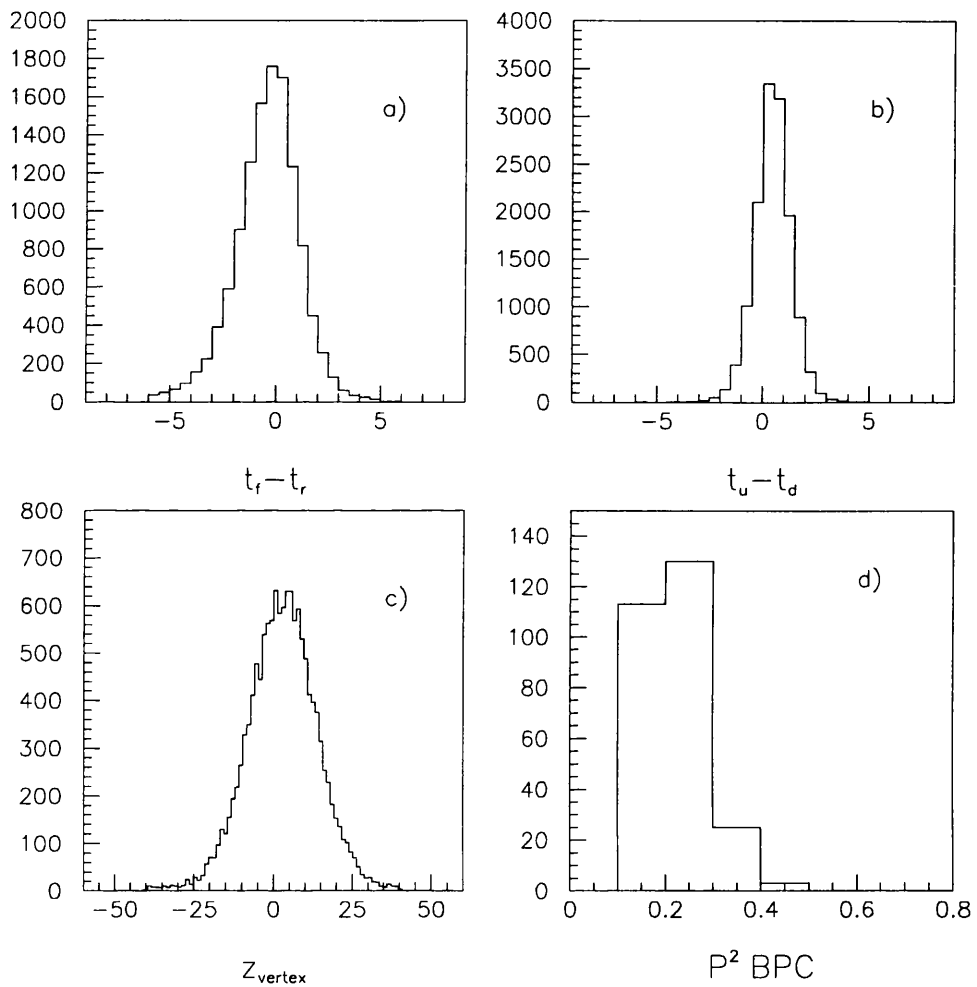


Figure 7.4: The (a)  $t_f - t_r$ , (b)  $t_u - t_d$ , and (c)  $z_{vertex}$  distributions for the final event sample. (d) shows the measured  $P^2$  distribution of the BPC tagged data.

Before one can compare the hadron level and reconstructed level values of jet properties it is essential that the hadron jet and reconstructed jet concerned refer to the same object. A criterion must be defined by which hadron level jets and reconstructed level jets are “matched” before their properties can be compared.

Figure 7.6 (a) shows the distribution of the distance in  $\eta\phi$  space,  $r = [(\eta_{rec} - \eta_{had})^2 + (\phi_{rec} - \phi_{had})^2]$  between a hadron jet and the nearest reconstructed jet.

There is a clear peak at small values of  $r$ . A hadron jet and a reconstructed jet are defined as being matched if  $r \leq 1$ . The two jets in a dijet event are produced back-to-back in  $\phi$ ; this accounts for the peak at  $r \approx \pi$ . Only matched pairs of jets contribute to the resolutions shown in figure 7.6 (b), (c) and (d).

The accuracy of the  $\eta^{jet}$  measurement is such that the same cuts can be applied at reconstructed level as at hadron level without fear of reducing the jet matching efficiency substantially. This is not the case for cuts applied to  $E_T^{jet}$ . Energy losses in the material before the calorimeter result in the  $E_T$  of reconstructed jets being approximately 20% lower than that of hadron level jets (see figure 7.6 (d)). To measure the cross-section for dijet events with  $E_T^{jet} > 5 \text{ GeV}^2$ , events with two jets with  $E_T^{jet} > 4 \text{ GeV}^2$  were selected to take account of the 20% offset. The effect of this decision is discussed in section 7.6.1.

The efficiency for matching hadron level jets of  $E_T \geq 5 \text{ GeV}$  with reconstructed level jets of  $E_T \geq 4$  is shown as a function of  $\eta$  in figure 7.7.

An event is classified as direct or resolved by means of a cut on the quantity  $x_\gamma^{obs}$  defined by equation 1.18 which is restated below for convenience.

$$x_\gamma^{obs} = \frac{\sum_{j=1}^2 E_T^j e^{-\eta^j}}{2E_e y} \approx \frac{\sum_{j=1}^2 E^j - p_z^j}{\sum_{hadrons} E - p_z} \quad (7.1)$$

Comparing the resolutions of the two measurements of  $y$  presented in figures 7.5 (a), (b) and (c) suggests that  $y_e$  should be used for the calculation of  $x_\gamma^{obs}$  in preference to  $y_b$  as it is the more accurate measurement. This overlooks the fact that the effect of energy scale uncertainties in the measurement of the jets and hence the numerator in equation 7.1 can be removed if the same calorimeter is

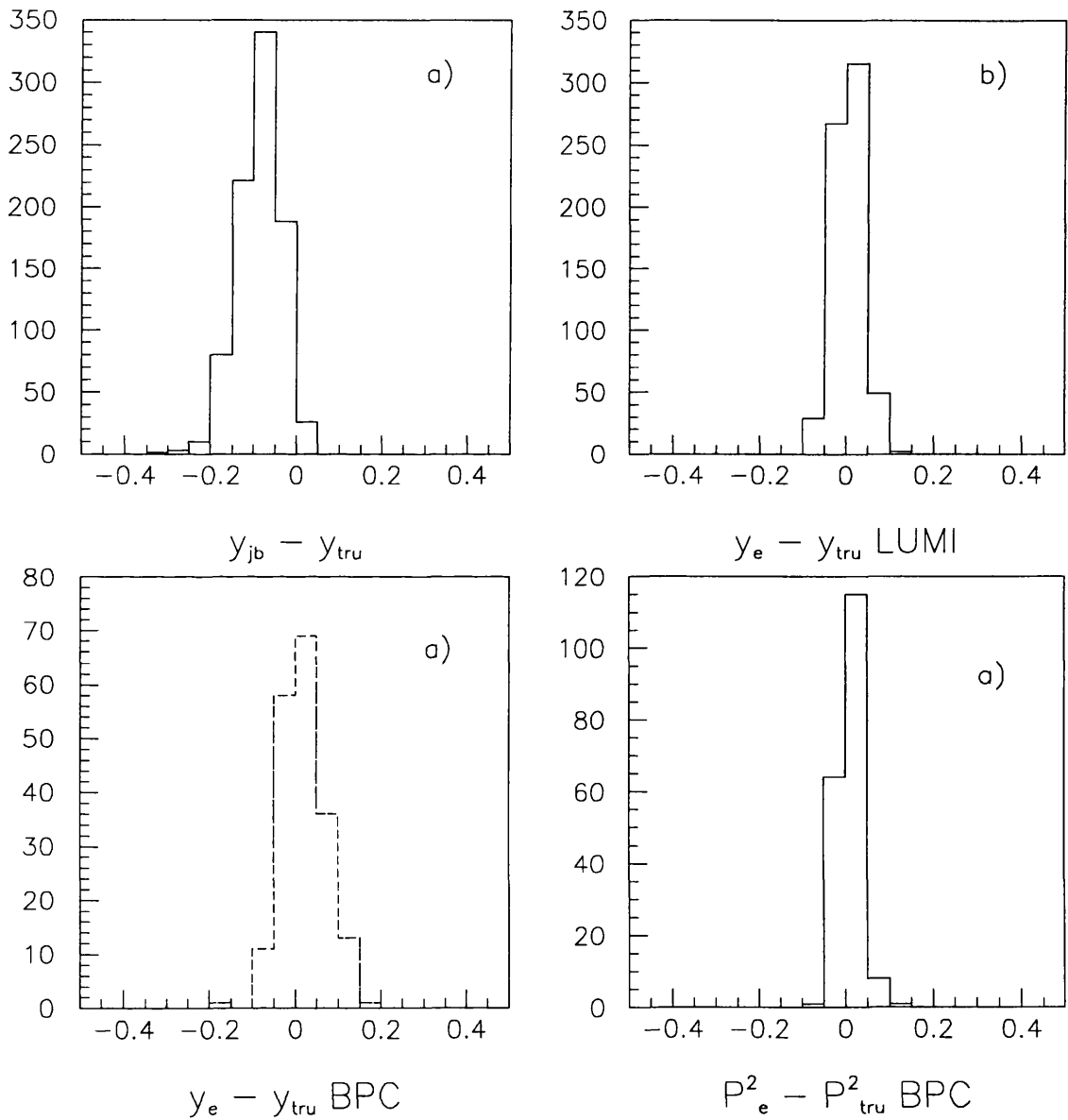


Figure 7.5: Distributions showing the resolutions of the measurements of  $y$  and  $P^2$ . Note that energy losses in the calorimeter and losses down the rear beam pipe mean that  $y_{jb}$  is systematically lower than  $y_{tru}$ .

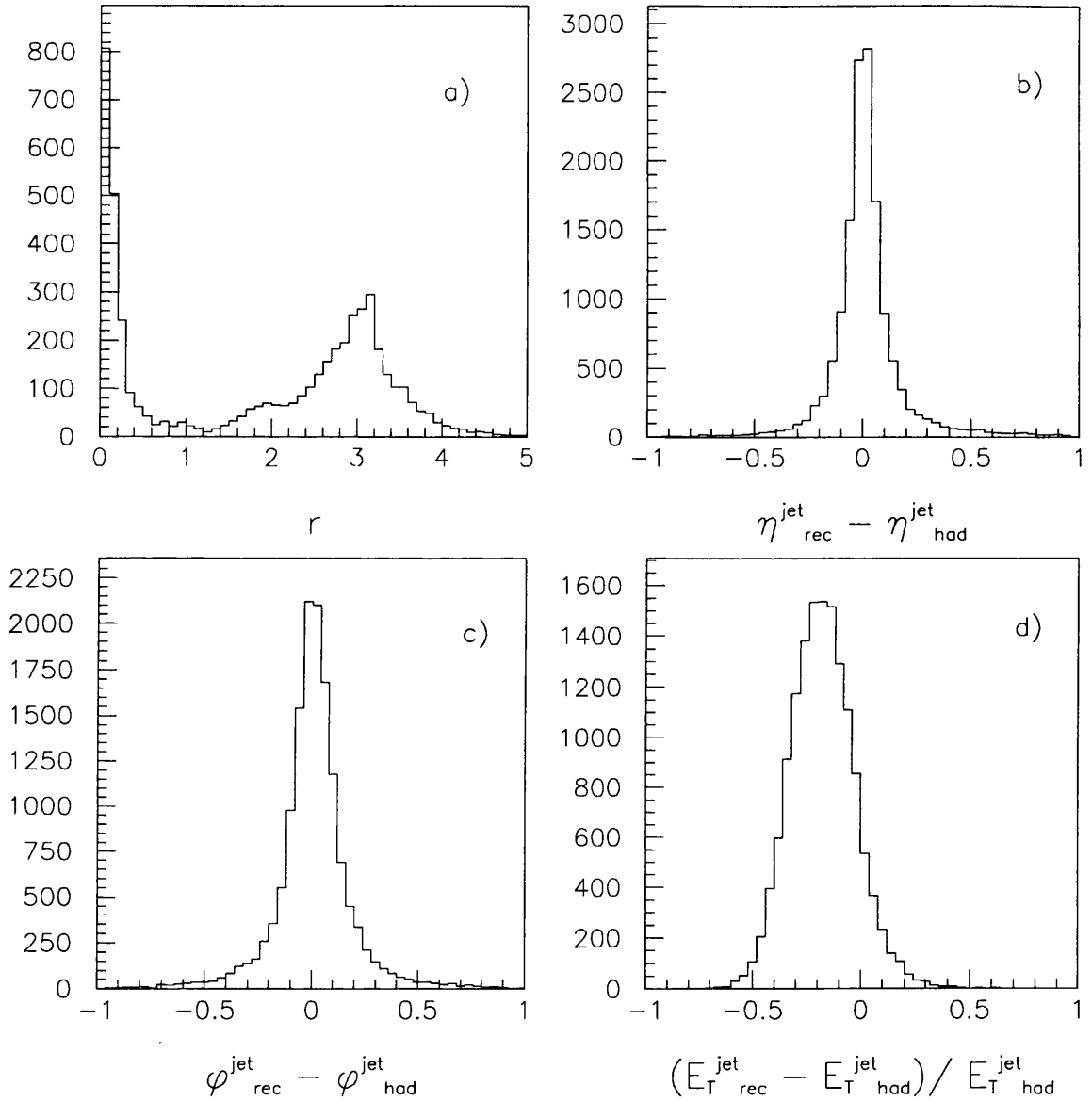


Figure 7.6: The resolutions of measurements of jet quantities: the distance  $r$  in  $\eta\phi$  space between a hadron level jet and any reconstructed level jet in the same event (a); the (b)  $\eta$ , (c)  $\phi$  and (d)  $E_T$  resolutions of jet measurements.

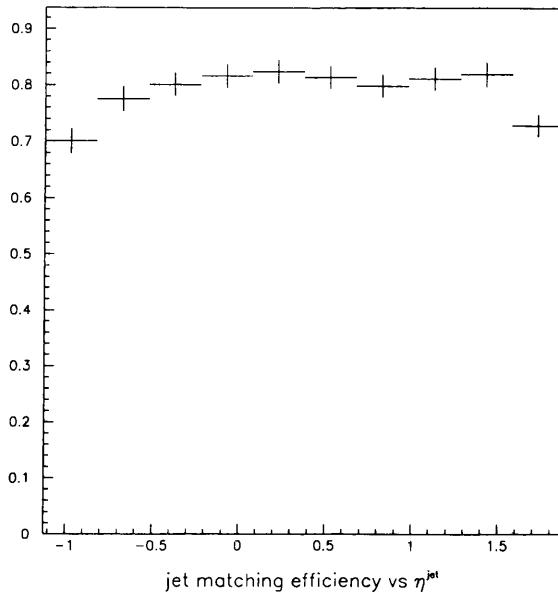


Figure 7.7: The efficiency of matching  $E_T > 5$  GeV hadron level jets with  $E_T > 4$  GeV reconstructed level jets, as a function of  $\eta_{had}^{jet}$ .

used to measure the denominator. The errors involved in the measurement of  $y_{jb}$  cancel the errors involved in measuring the jets; the more accurate measurement of  $x_\gamma^{obs}$  is hence obtained using  $y_{jb}$  rather than  $y_e$ .

This method of calculating  $x_\gamma^{obs}$  gives the resolutions for  $x_\gamma^{obs}$  shown in figure 7.8 where events with two jets of  $E_T \geq 5$  GeV at hadron level and two jets of  $E_T \geq 4$  GeV at reconstructed level within the stated  $\eta$  range contribute to the histograms shown. The  $x_\gamma^{obs}$  resolutions obtained using  $y_e$  as opposed to  $y_{jb}$  are shown to illustrate the advantage in using  $y_{jb}$ . Uncorrected  $x_\gamma^{obs}$  distributions are presented in section 7.4.

### 7.3 Jet Profiles

Jet profiles in  $\eta$  and  $\phi$  were constructed for both LUMI and BPC data samples. The profiles in  $\eta$  are the  $E_T$  weighted distributions of  $\Delta\eta = \eta_{cell} - \eta^{jet}$  for cells

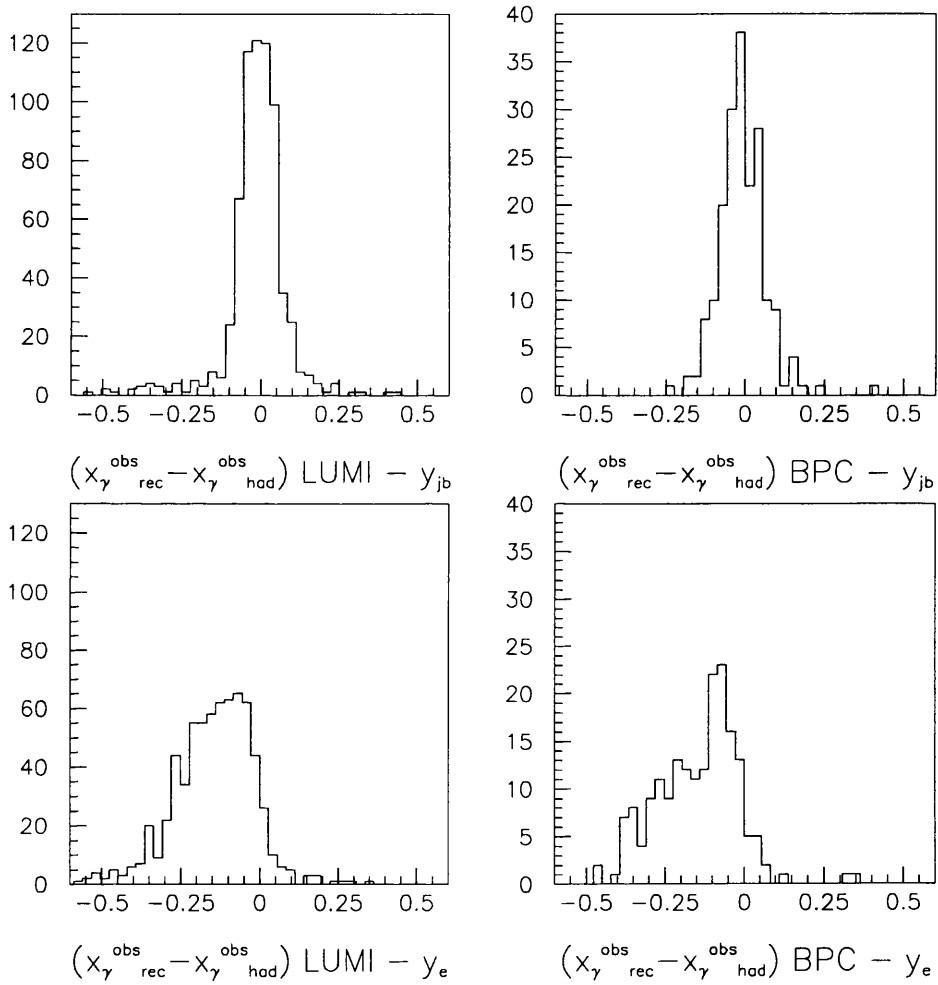


Figure 7.8: The resolutions for the measurement of  $x_{\gamma}^{\text{obs}}$  determined from simulated LUMI and BPC tagged events using  $y_{jb}$  (above) and  $y_e$  (below) to measure the photon energy  $E_{\gamma} = 2yE_e$ .

within a band of 1 radian in  $\phi$  of the jet centre (see chapter 5).

The profiles in  $\eta$  for events with  $x_\gamma^{obs}$  in the ranges  $0.0 < x_\gamma^{obs} < 0.4$  and  $0.4 < x_\gamma^{obs} < 0.75$  are presented in figure 7.9, the dotted histogram showing the BPC profile and the solid histogram the LUMI profile in each case. Two  $x_\gamma^{obs}$  ranges were used for the resolved events to account for the substantial difference in the shapes of the BPC and LUMI  $x_\gamma^{obs}$  distributions below  $x_\gamma^{obs} = 0.75$ .

Only jets with an  $E_T < 10$  GeV were chosen to contribute to the profiles shown. This ensured that the mean  $E_T$  of jets was similar for the BPC and LUMI samples; the tail of the  $E_T^{jet}$  distribution of the LUMI data would otherwise hinder the comparison of the LUMI and BPC profiles as the normalization of the profiles in figure 7.9 is absolute. It can be seen that the BPC tagged profile is slightly narrower than the LUMI tagged profile within the jet ( $\Delta\eta < 1$ ) and that there is less transverse energy flow in the positive  $\Delta\eta$  region. These profiles thus lend some support to the hypothesis that the level of multiple interactions may decrease as the virtuality of the photon increases.

There is no such difference between the profiles constructed for direct events ( $x_\gamma^{obs} > 0.75$ ), nor between the profiles in  $\phi$  for both direct and resolved events. These profiles are presented in figure 7.10.

## 7.4 $x_\gamma^{obs}$ Distributions

Figure 7.11 shows the  $x_\gamma^{obs}$  distributions for the two samples of events tagged with the BPC and the LUMI tagger. In each case there is a clear peak at high values of  $x_\gamma^{obs}$  that is associated with the direct contribution and a class of events at low  $x_\gamma^{obs}$  that is associated with the resolved process. By utilizing the cut at  $x_\gamma^{obs} = 0.75$ , the uncorrected ratio  $N_{res}/N_{dir}$  was obtained and is presented in figure 7.12. The error on the ratio of  $N_{res}$  resolved events and  $N_{dir}$  direct events is given by  $\sigma_{ratio} = \sqrt{(N_{res} + N_{dir})N_{res}/N_{dir}^3}$ .

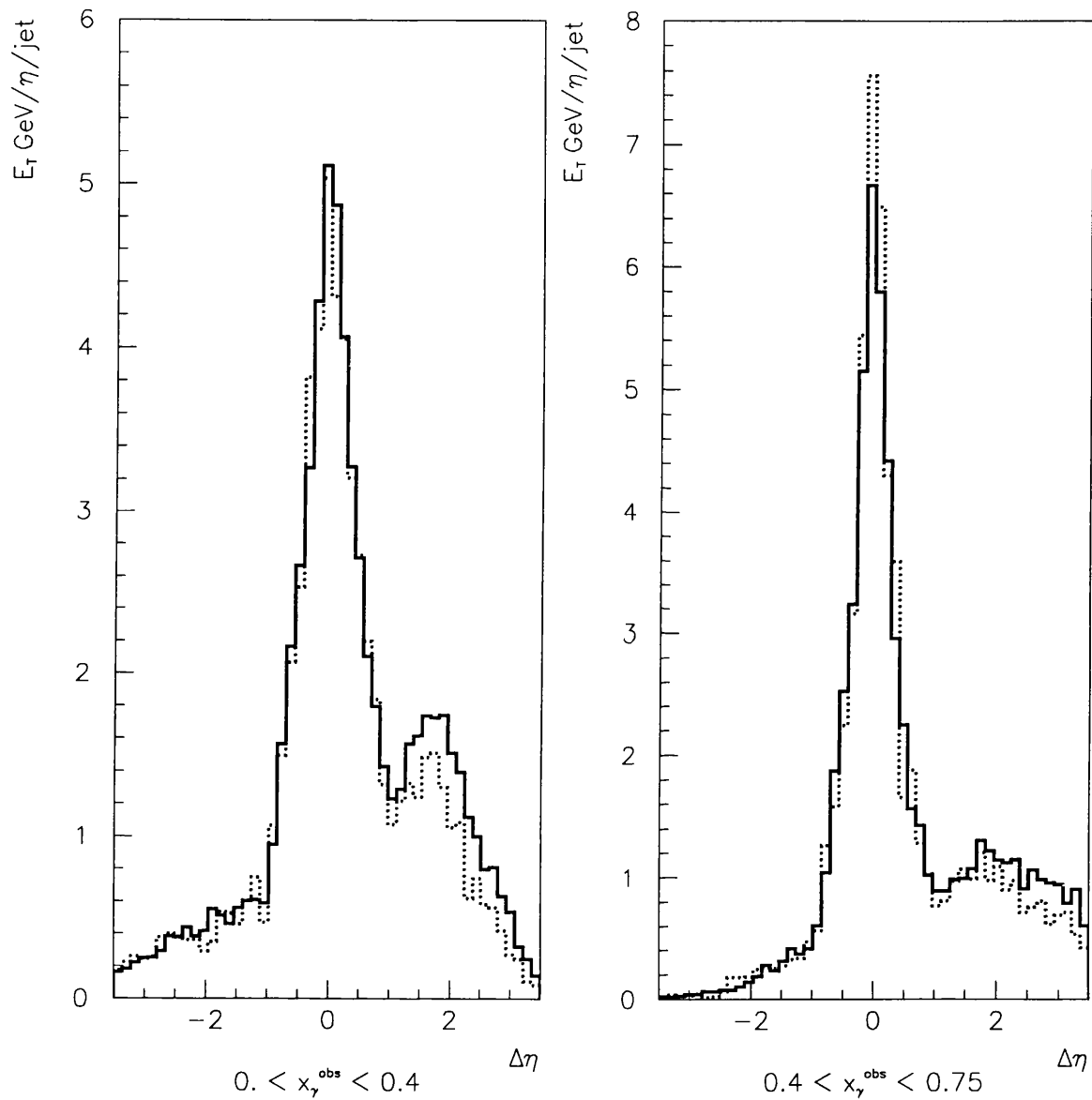


Figure 7.9: Jet profiles in  $\eta$  for both LUMI tagged (solid) and BPC tagged (dotted) events in the kinematic regimes defined by  $x_\gamma^{\text{obs}} < 0.4$  and  $0.4 < x_\gamma^{\text{obs}} < 0.75$ .

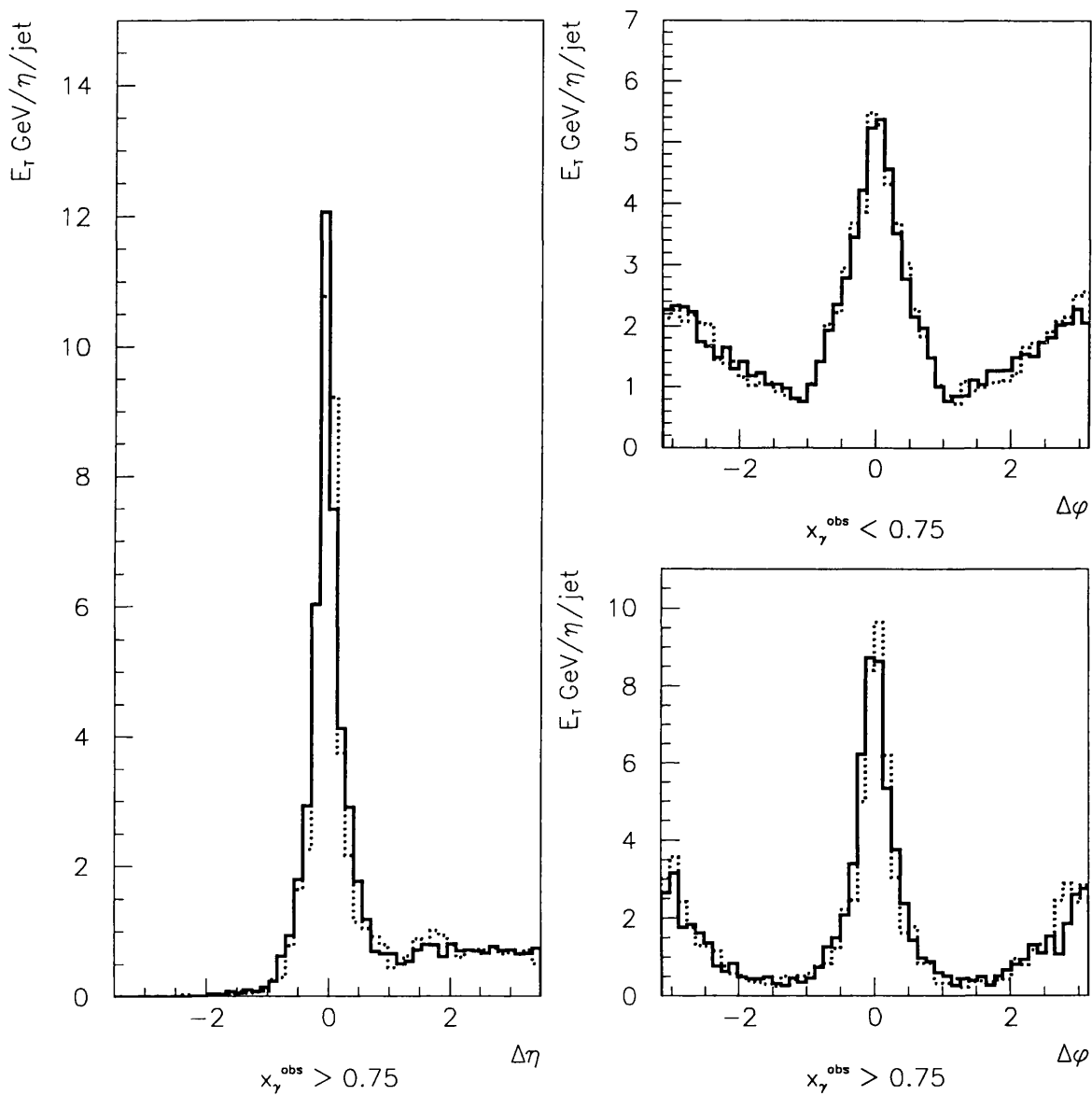


Figure 7.10: LUMI tagged (solid) and BPC tagged (dotted) jet profiles: in  $\eta$  for events with  $x_\gamma^{\text{obs}} > 0.75$  and in  $\phi$  for  $x_\gamma^{\text{obs}} < 0.75$  and  $x_\gamma^{\text{obs}} > 0.75$ .

### 7.4.1 Preliminary Considerations

To draw conclusions based upon the different  $P^2$  ranges of the two data samples, it is important to ensure that other differences between the samples that could “fake” a  $P^2$  dependence are understood and accounted for.

Of particular importance is the  $y$  (and hence the  $E_\gamma$ ) distribution of the two samples. The intrinsic  $y$  distribution of  $e^\pm p$  events is described by the Weizsäcker Williams equivalent photon approximation given in equation 5.1.  $y$  governs the centre of mass energy available for the production of jets. Requiring two jets above a certain  $E_T^{jet}$  in the final state preferentially rejects low  $y(E_\gamma)$  events. This kinematic constraint is harsher for low  $x_\gamma^{obs}$  than for high  $x_\gamma^{obs}$  events as, at a given  $y$  and  $x_p$ , the parton-parton c.m energy decreases with decreasing  $x_\gamma^{obs}$ . As  $y$  increases, lower values of  $x_\gamma^{obs}$  are sufficient for the production of the required jets and the contribution from resolved photon processes hence increases relative to the contribution from direct processes.

The two electron taggers differ in their  $y$  acceptance. This results in the LUMI sample having a higher mean value of  $y$  than the BPC sample. This will act to give the LUMI sample a higher value of  $N_{res}/N_{dir}$  regardless of any effect due to the evolution of the photon structure.

To separate the  $P^2$  and  $y$  dependences in the uncorrected data, the ratio  $N_{res}/N_{dir}$  has been measured as a function of  $y_e$ , as calculated from the energy of the scattered electron. Figure 7.12 shows the uncorrected ratio  $N_{res}/N_{dir}$  plotted against  $y_e$  for both  $P^2$  ranges.

## 7.5 Bin Purities

For each  $P^2$  and  $x_\gamma^{obs}$  bin the purity, defined as the fraction of events in that bin at reconstructed level that were in that bin at hadron level, was obtained. Table 7.5 presents the purity of the LUMI tagged Monte Carlo sample for resolved and direct events. The impurity is mainly due to events migrating from below

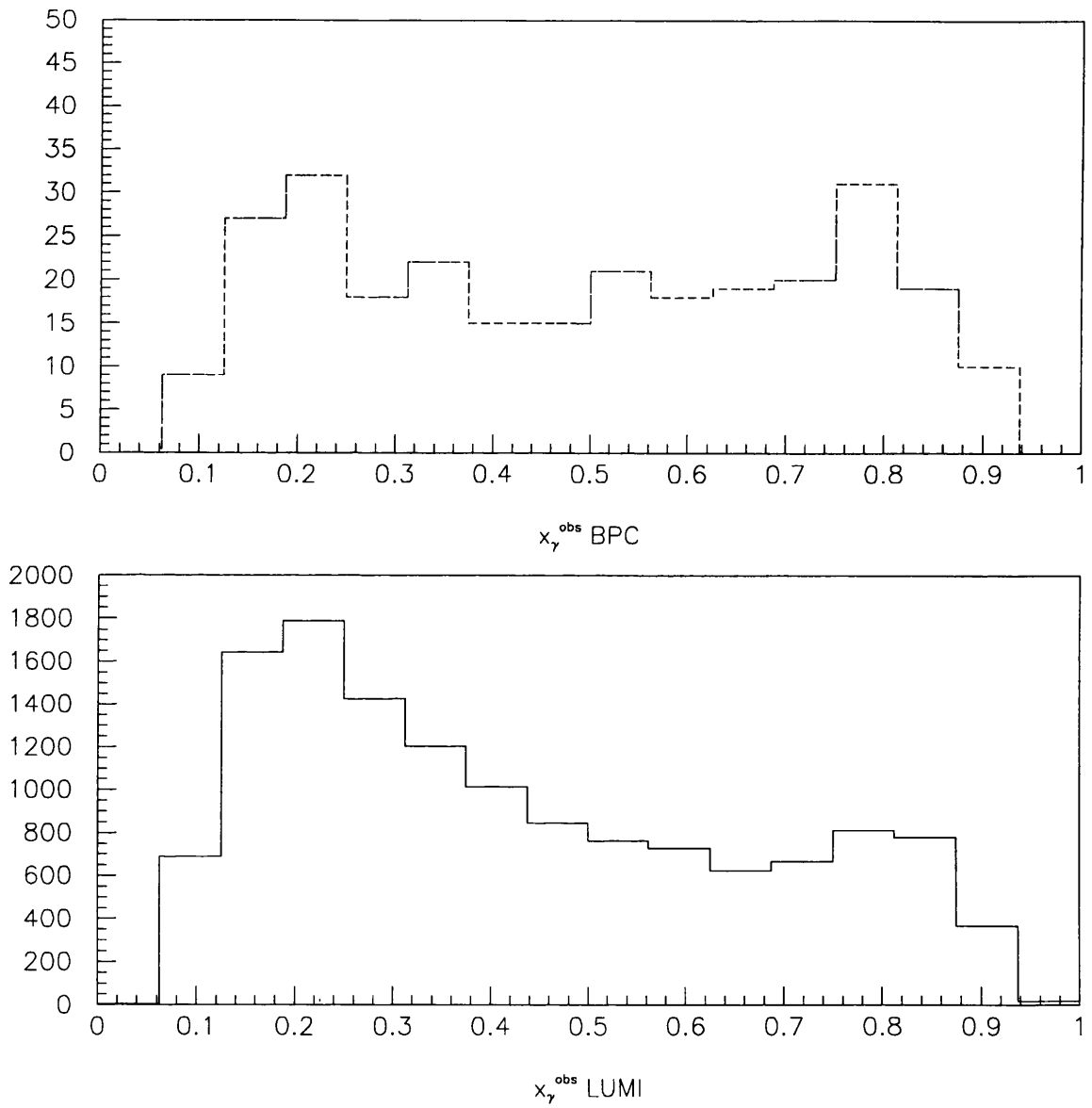


Figure 7.11: The uncorrected  $x_\gamma^{\text{obs}}$  distribution for the BPC tagged sample (above) and the LUMI tagged sample (below).

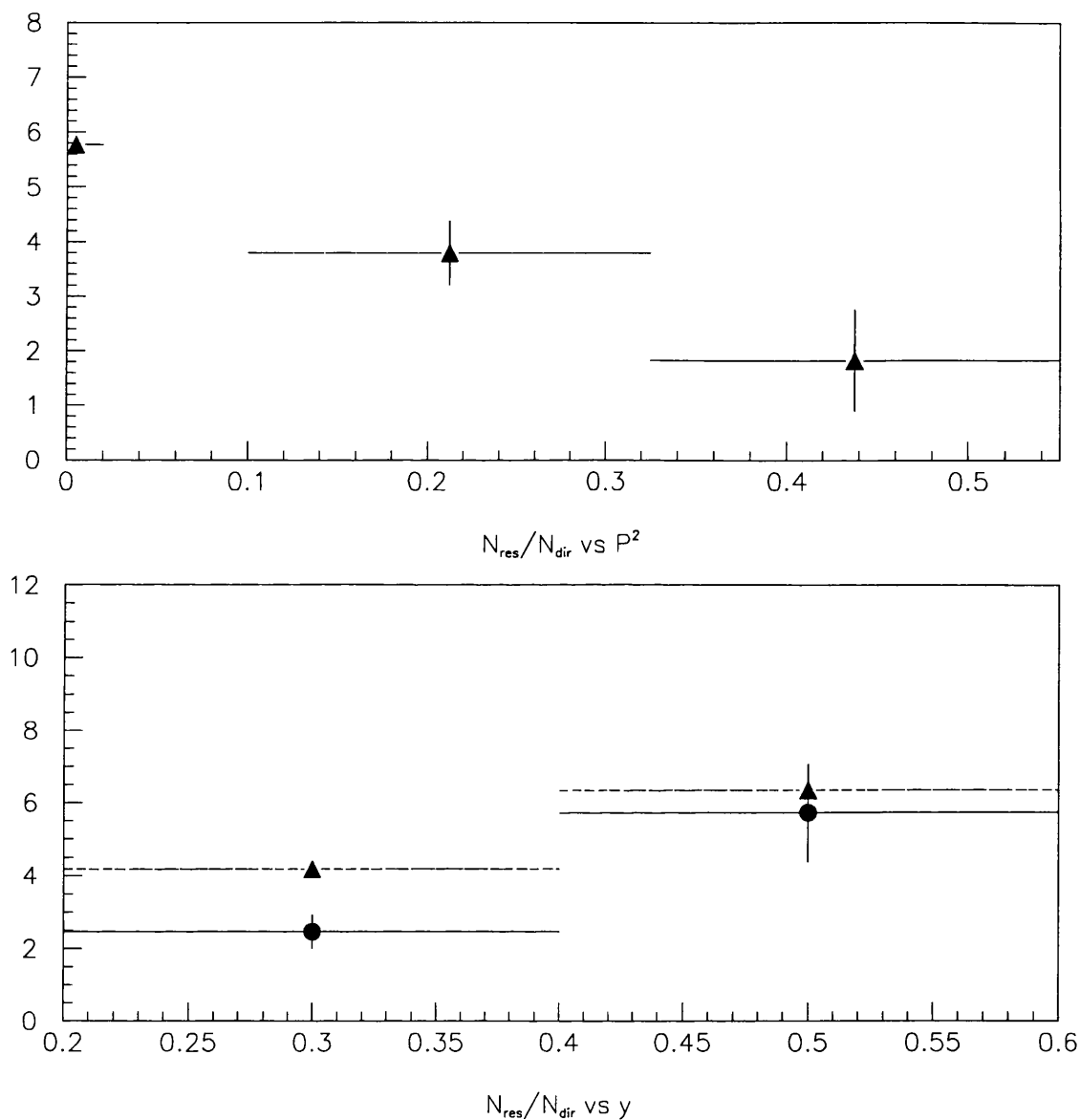


Figure 7.12: The uncorrected ratio  $N_{res}/N_{dir}$  plotted as a function of  $P^2$  (GeV<sup>2</sup>) (above) and as a function of  $y$  for both LUMI (triangles) and BPC (circles) data (below). In the lower plot it should be mentioned that the error on the LUMI point (obscured by the error bar on the BPC point) is negligible.

the  $E_T^{jet}$  cut (see section 7.6). If more than one  $P^2$  bin is used for the range  $0.1 < P^2 < 0.55$ , the additional impurity from  $P^2$  migrations introduces doubt into the validity of the corrections. The migrant events introduced to the higher  $P^2$  bin come from lower  $P^2$  and hence have a higher value of  $N_{res}/N_{dir}$  than the indigenous population of that bin (see figure 7.12). Other things being equal, this suggests that the  $P^2$  migrations act such that the true  $P^2$  dependence is more severe than is observed in the uncorrected BPC data.

Bin	Purity
LUMI Resolved	58%±1%
LUMI Direct	75%±2%
BPC Resolved	55%±2%
BPC Direct	66%±4%

Table 7.1: The purities of the analysis bins used to obtain the corrected results presented in this chapter.

## 7.6 Correction Techniques

In obtaining the corrected ratio of the direct and resolved contributions to the hadron level dijet cross section defined by  $E_T^{jet} > 5$  GeV,  $-1.125 < \eta^{jet} < 1.875$  within  $0.2 < y < 0.6$  from the uncorrected data presented in section 7.4, several effects of the detector response, resolution and acceptance were studied. These are discussed below. For each  $P^2$  bin  $i$ , a correction factor  $C_i$ , defined by equation 7.2, was obtained and applied to the uncorrected data.

$$C_i = \frac{(\sigma_{res}/\sigma_{dir})_i^{HAD}}{(N_{res}/N_{dir})_i^{REC}} \quad (7.2)$$

### 7.6.1 Migrations from Below $E_T^{jet}$ Cut

A hadron level jet is reconstructed in the calorimeter as having an  $E_{Trec}^{jet}(20 \pm 20)\%$  lower than  $E_{Thad}^{jet}$  (see figure 7.6 (d)). The 20% offset shown in figure 7.6 motivates the use of the cut of 4 GeV on  $E_T^{jet}$  applied to the data; the width of the distribution has implications for the correction of the raw data.

Many jets of  $E_T^{jet} > 5$  GeV will be reconstructed as having  $E_T^{jet} < 4$  GeV; many jets of  $E_T^{jet} < 5$  GeV will be reconstructed as having  $E_T^{jet} > 4$  GeV. One might think that as the distribution describing the smearing of  $E_T^{jet}$  is reasonably symmetric, these “migrations” across the  $E_T$  cut would negate each other. This is not the case, however, as there are significantly more hadron jets with  $E_T^{jet}$  below 5 GeV that could pass the 4 GeV cut at reconstructed level than hadron jets with  $E_T^{jet}$  above 5 GeV that could fail the 4 GeV cut (see figure 7.1). There is hence a net migration into the data sample of events with  $E_{Thad}^{jet} < 5$  GeV. Crucially, the level of this migration differs for the resolved and direct subsamples; resolved events have a softer  $E_T^{jet}$  spectrum than direct events as shown in figure 7.13. This disparity has the effect of making the reconstructed value of the ratio  $N_{res}/N_{dir}$  larger than the hadron level value.

### 7.6.2 Migrations Across $x_\gamma^{obs}$ Cut

Events that are “direct” at hadron level may be reconstructed as “resolved” and vice versa. Such migrations obviously affect the ratio  $N_{res}/N_{dir}$  and should be corrected for. The level of these migrations in the data can be ascertained from the Monte Carlo sample only if the shape of the  $x_\gamma^{obs}$  distribution is well described around the region of the cut at 0.75. Figure 7.14 (a) shows the hadron level value of  $x_\gamma^{obs}$  for migrant events where the direct/resolved classification differs at hadron and reconstructed level. The Monte Carlo and data  $x_\gamma^{obs}$  distributions are in fair agreement over the limited range required to describe migrations across the 0.75 cut as can be seen in figure 7.14 (b).

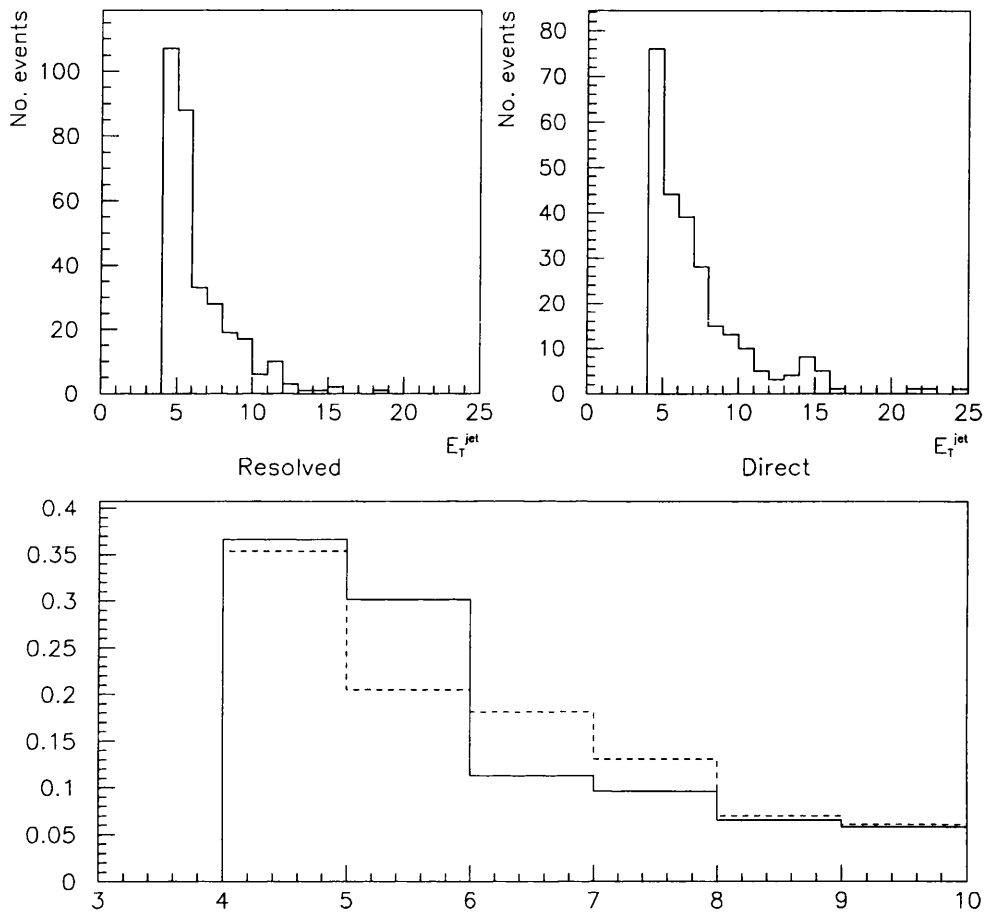


Figure 7.13: The  $E_T^{jet}$  spectrum for events generated as (a) resolved and (b) direct. To show that the resolved sample has a softer  $E_T^{jet}$  spectrum, the two have been area normalized and superimposed in (c) where the solid line is the resolved sample and the dashed line is the direct sample.

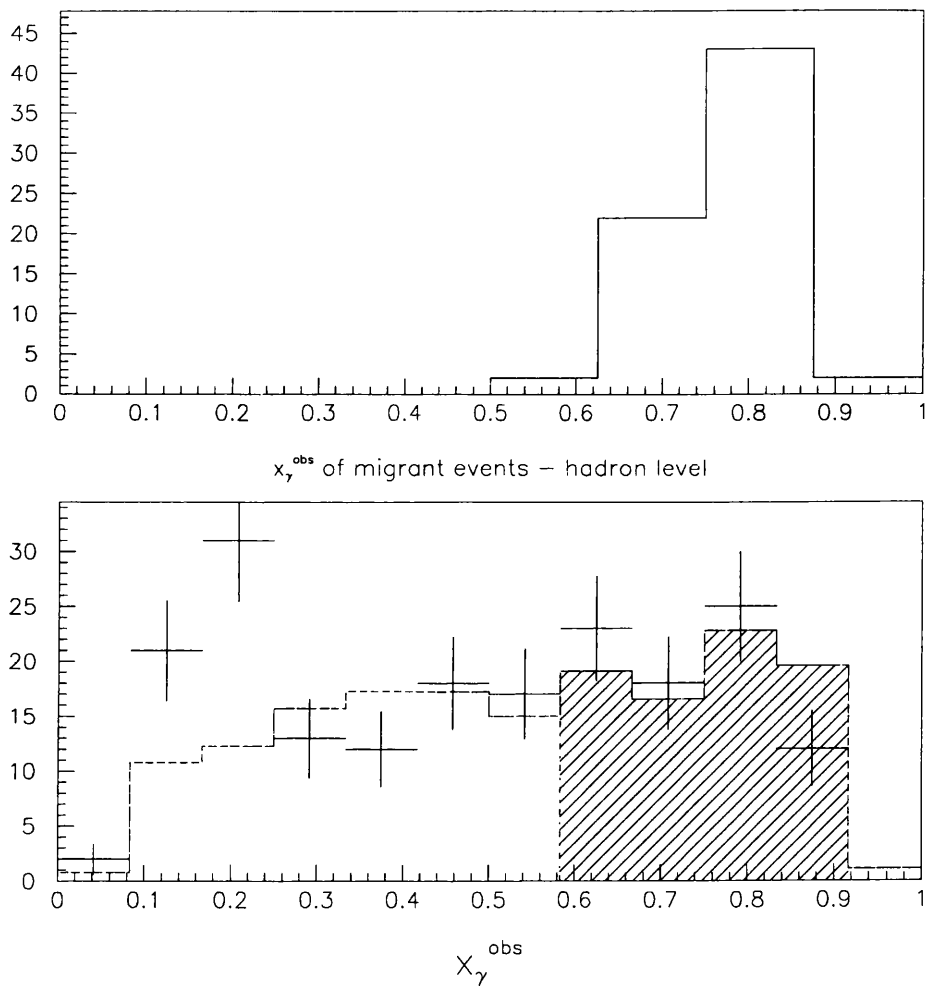


Figure 7.14: The  $x_\gamma^{\text{obs}}$  distribution for Monte Carlo events where the hadron level and reconstructed level classification of the event as direct or resolved differs (a) and a comparison of the Monte Carlo (hatched histogram) and BPC data  $x_\gamma^{\text{obs}}$  distributions (b). To compare the shapes of the data and Monte Carlo distributions near the cut of 0.75, the histograms are area normalized in the shaded region. The agreement is adequate to correct the ratio  $N_{res}/N_{dir}$  for migrations in  $x_\gamma^{\text{obs}}$ .

## 7.7 $y$ Acceptance

The ratio of the resolved and direct contributions to the dijet cross-section is dependent on  $y$  as discussed in section 7.4.1. This  $y$  dependence is shown in figure 7.15 for the Monte Carlo (truth and reconstructed levels) and the uncorrected data.

In measuring the ratio of the resolved and direct dijet cross-sections over a range in  $y$  it is important to account for the  $y$  dependence of the acceptance of the two electron taggers. Figures 7.16 (a) and (b) show the truth level  $y$  distributions for dijet events with  $P_{tru}^2$  in the ranges covered by the LUMI tagger and the BPC respectively.

The  $y_e$  distribution for LUMI tagged dijet events is presented in figure 7.16 (c), the reconstructed level Monte Carlo represented by the shaded histogram. The acceptance of the LUMI tagger increases with  $y$ . This means that the high  $y$ , high  $\sigma_{res}/\sigma_{dir}$  portion of the cross-section dominates the mean uncorrected ratio  $N_{res}/N_{dir}$ . This feature necessitates the application of a large correction to the LUMI tagged data. The agreement between the reconstructed level Monte Carlo and data  $y_e$  distributions for both the LUMI tagger and the BPC (figure 7.16 (d)) validates the truth level  $y$  distribution (figures 7.16 (a) and (b)) and hence allows this effect of the LUMI acceptance to be corrected for.

## 7.8 The Correction Factors and the Corrected Data

The correction factors, defined by equation 7.2, are presented in table 7.8. The correction factor for the LUMI tagged data is significantly lower than that for the BPC tagged data due to the  $y$  acceptance of the LUMI tagger as discussed in section 7.6.

The raw data presented in figure 7.12 were multiplied by the corresponding

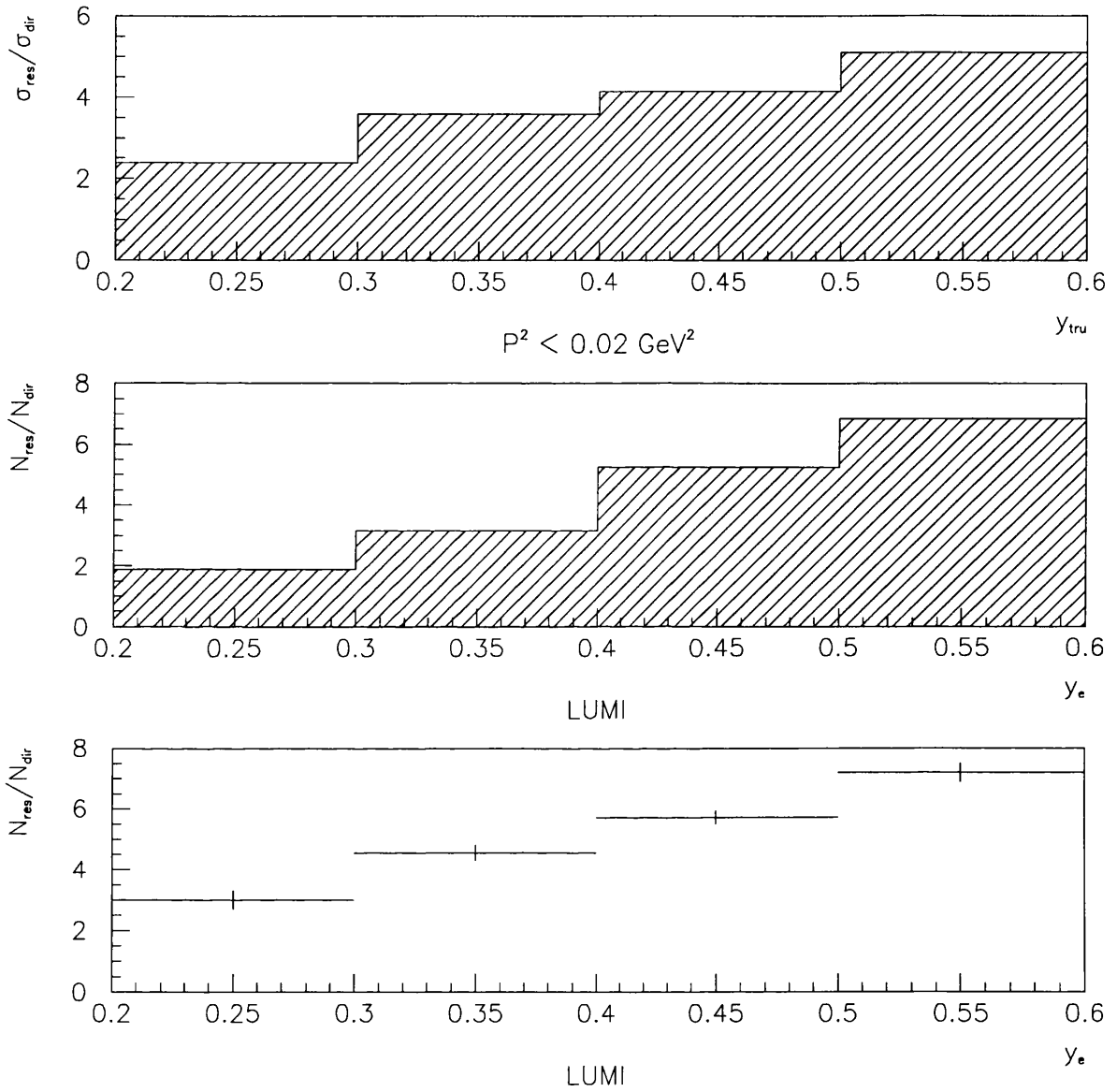


Figure 7.15: The ratio of the resolved and direct contributions at: (a) hadron level Monte Carlo, (b) reconstructed level Monte Carlo and (c) in the LUMI tagged data.

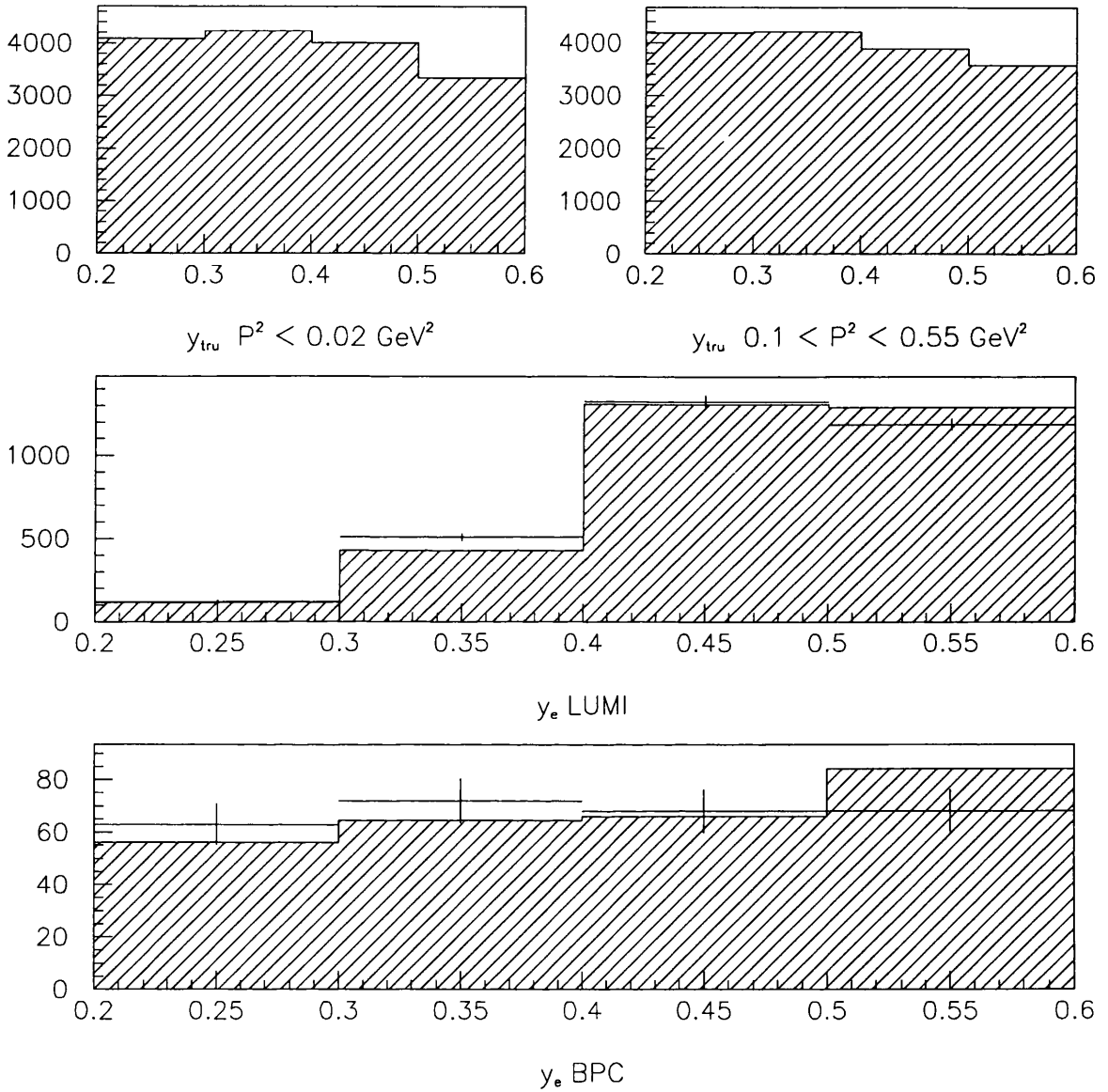


Figure 7.16: The  $y$  distributions for dijet events at hadron level ((a) and (b)). (c) and (d) show the agreement between the reconstructed level Monte Carlo (shaded histogram) and the data points for both LUMI tagged and BPC tagged. The data and Monte Carlo presented in figures (c) and (d) are area normalized.

Bin	Correction Factor
LUMI	$0.70 \pm 0.03$
BPC	$0.82 \pm 0.09$

Table 7.2: The correction factors applied to the uncorrected data as determined by the study of detector effects through the use of Monte Carlo events.

correction factor (the two  $P^2$  points of the BPC tagged data being combined) to give the corrected results presented in figure 7.17. The BPC point is plotted at the corrected mean  $P^2$  of the BPC tagged data, the correction applied to the mean  $P^2$  of the BPC data being obtained from the truth level and reconstructed level Monte Carlo  $P^2$  distributions of events satisfying the kinematic or reconstruction cuts respectively; the error bars on  $P^2$  reflect the range of the measured  $P^2$  values rather than the error on the corrected mean  $P^2$ . This result is discussed in the next chapter. The next section of this chapter is concerned with the evaluation of the systematic errors associated with the measurement.

## 7.9 Systematic Errors

The results in figure 7.17 refer to a cross-section defined by the “true” kinematic variables  $P^2$ ,  $y$ ,  $\eta^{jet}$ ,  $E_T^{jet}$ . Changes to the cuts applied to the data and to the reconstructed level will affect the uncorrected data and the correction factors respectively but ideally should not affect the corrected data. To determine the systematic error introduced to the measurement by the choice of cuts, the following changes to the cuts applied to both the raw data and the reconstructed level Monte Carlo were made, one at a time, and the effect on the central values of the corrected data ascertained.

As stated in chapter 5, the less than rigorous treatment of the kinematics of

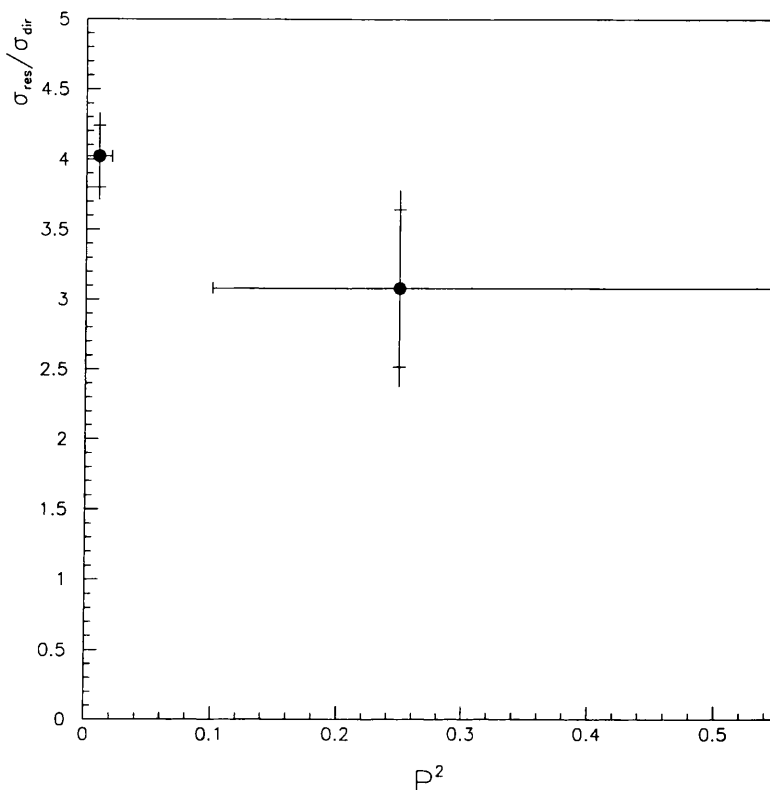


Figure 7.17: The corrected ratio of the resolved and direct contributions to the dijet cross-section as determined by a cut at 0.75 on the quantity  $x_{\gamma}^{obs}$  as a function of the photon virtuality  $P^2$  (GeV<sup>2</sup>). The vertical error bars show the statistical errors (inner) and the statistical and systematic errors added in quadrature (outer).

the  $e\gamma$  vertex within PYTHIA precludes the correction of the tagged data using a hadronization scheme different from that used in HERWIG. Studies of untagged hard photoproduction show, however, that the systematic error introduced by the choice of hadronization scheme is of the order of 5-10% for measurements of jet cross-sections [20][60].

The effect of these changes on the central values of the corrected result are shown in figure 7.18 where the changes from the central value are given as percentages and the statistical errors are shown as solid lines. It can be seen that none of the systematic errors for either  $P^2$  bin is as large as the corresponding

Cut	Value Used	Lower Systematic	Upper Systematic
$E_T^{jet}$	4.0 GeV	-	4.5 GeV
$\eta^{jet}$ max	1.875	1.800	1.950
$\eta^{jet}$ min	-1.125	-1.200	-1.050
$y_e$ max	0.60	0.58	0.62
$y_e$ min	0.20	0.18	0.22
$y_{jb}$ max	0.70	0.68	0.72
$y_{jb}$ min	0.15	0.13	0.17
$ z_{vertex} $ max	40cm	35cm	-

Table 7.3: The changes made to the cuts applied to the reconstructed level Monte Carlo and to the data in order to ascertain the systematic error introduced by the choice of cuts.

statistical error. It should also be noted that, in most cases, the systematic errors act in the same direction ( $\pm$ ) for both the LUMI and BPC bin.

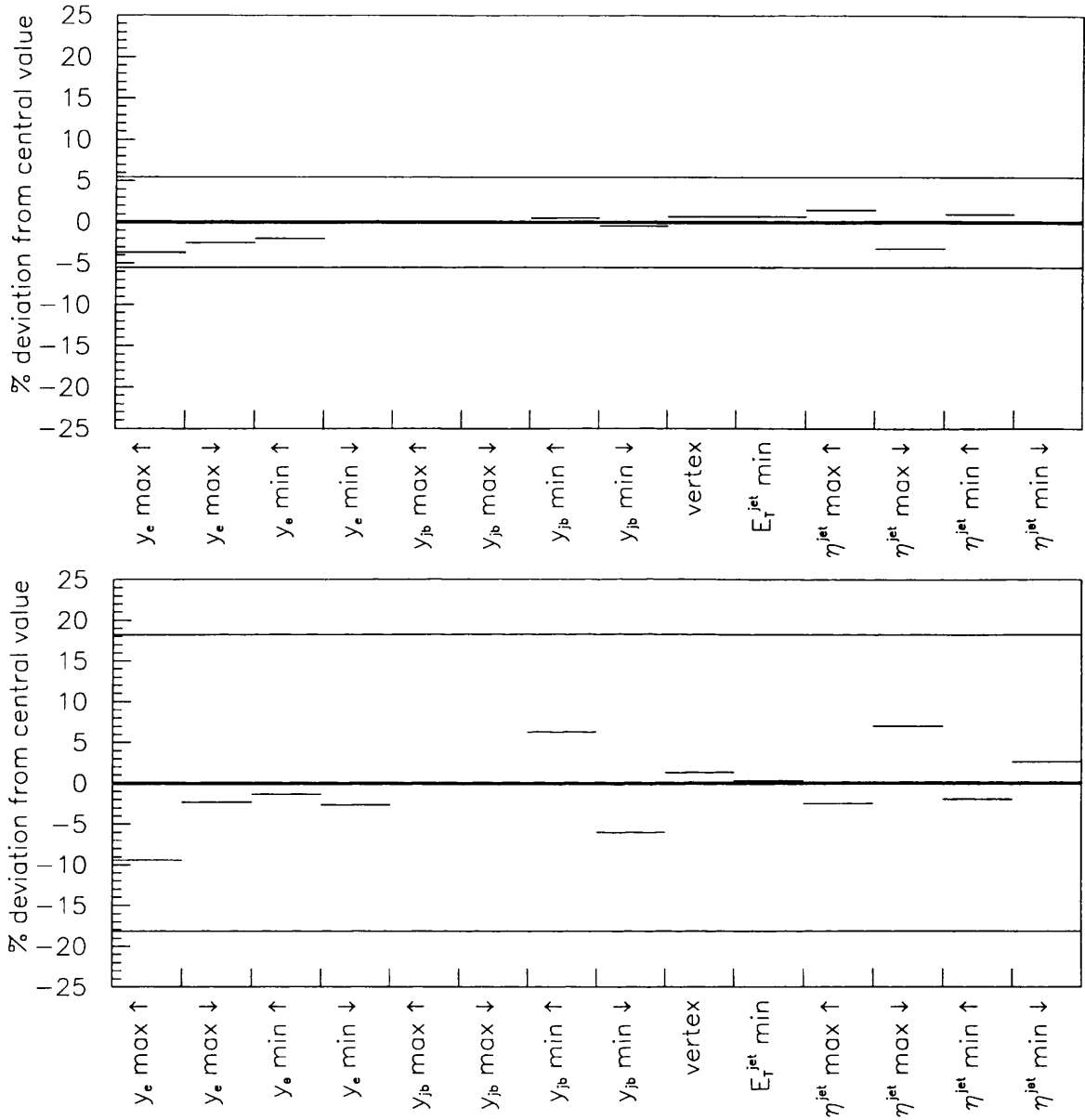


Figure 7.18: The systematic errors on the corrected result introduced by the choice of cuts applied to the data and reconstructed level Monte Carlo for real photons (above) and virtual photons (below). The continuous lines show the statistical errors associated with the central values of the corrected results.

# Chapter 8

## Interpretation of Results

### 8.1 Leading Order Calculations

As mentioned in chapter 5, the resolved and direct cross-sections for the production of two partons with  $E_T > 4\text{GeV}$  and  $-1.125 < \eta < 1.875$  for  $0.2 < y < 0.8$  have recently been calculated to leading order by de Florian *et al.* [54]. These calculations were done at parton level with no hadronization and hence no jet finding applied. As  $x_\gamma^{obs}$  is a final state observable and is not defined at parton level, the ratio of the resolved and direct cross-sections was calculated using a cut on the true  $x_\gamma$ , the fraction of the photon momentum entering the hard scatter. Events with  $x_\gamma \geq x_\gamma^{threshold}$  were classified as direct and events with  $x_\gamma < x_\gamma^{threshold}$  as resolved. The natural choice of  $x_\gamma^{threshold}$  is 1 as this is in keeping with the definition of direct and resolved processes at leading order.

Comparison of the calculated ratio with the available uncorrected data [61] showed, however, that a value of  $x_\gamma^{threshold} < 1$  gave better agreement. This comparison neglected the fact that the  $E_T^{jet}$  cut of 4 GeV applied to the uncorrected data corresponds to a cut of  $\approx 5$  GeV at hadron level.

These same calculations have since been done by the same authors using the  $E_T$ ,  $\eta^{jet}$  and  $y$  cuts used to obtain the results presented in this thesis[62]. Figure

8.1 shows the calculated ratio of the resolved and direct cross-sections for two outgoing partons with  $E_T > 5$  GeV and  $-1.125 < \eta < 1.875$  for events with  $0.2 < y < 0.6$  as a function of  $P^2$  for four parametrizations of the structure of the real and virtual photon. The  $P^2$  dependence of the SAS1D, SAS2D and GRS pdf's are intrinsic to the parametrizations whereas the  $P^2$  dependence of the WHIT2 [63] pdf has been generated according to the prescription given by equation 5.2.

The three curves (one solid and two dotted) show the results obtained at three separate values of  $x_\gamma^{threshold}$ . The upper dotted line is the result for  $x_\gamma^{threshold} = 1.0$ , the solid line is for  $x_\gamma^{threshold} = 0.85$  and the lower dotted line for  $x_\gamma^{threshold} = 0.75$ . A decrease in the contribution from resolved photon processes is predicted in all cases for each parametrization.

There is a general accord between the corrected results and the LO calculations. It is somewhat naïve to expect parton level calculations incorporating no hadronization to predict anything other than the shape of the data. That the absolute values of the calculated LO ratio are in fair agreement with the experimental results is hence of no great significance.

Studies of the 1995 data obtained with the improved BPC [64] will be less limited by statistics and hopefully will result in more quantitative comparison of experimental results and theoretical predictions. The calculation of jet cross-sections that incorporate hadronization effects as well as the  $P^2$  dependence of the structure of the photon are necessary for such comparisons to be valid.

## 8.2 Conclusions

This thesis constitutes the first observation of the evolution of the photon structure with photon virtuality using data from the HERA  $ep$  collider. The presence of a contribution from resolved photon processes to the two jet production cross-section for events with photons of virtuality  $P^2$  in the range  $0.1 < P^2 < 0.55$

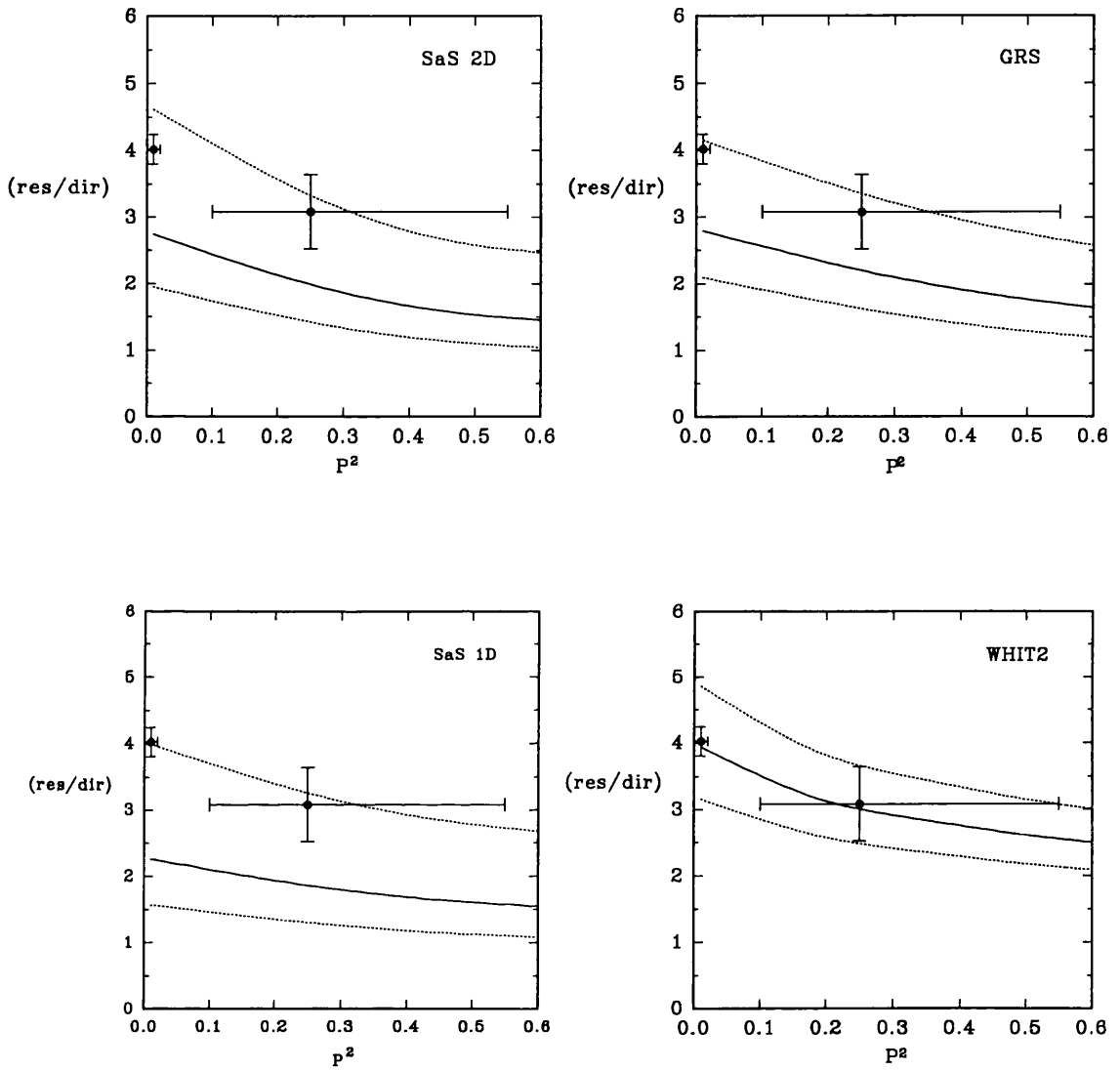


Figure 8.1: The corrected results obtained for this thesis compared to LO calculations by de Florian *et al.* using four different parametrizations of the structure of the virtual photon (see text).

$\text{GeV}^2$  has been observed. The data suggest the gentle fall off of the resolved contribution with increasing  $P^2$  predicted by each of the four parametrizations presented in figure 8.1.

The uncorrected jet profiles presented in chapter 7 provide some support for the hypothesis that the level of multiple interactions decreases with increasing virtuality due to the changing nature of the photon remnant.

Limited statistics preclude any stronger statement; whilst the data clearly favour a suppression of the resolved contribution with increasing  $P^2$  it should be noted that the corrected data are also statistically consistent with there being no such suppression whatsoever.

The parametrizations of the structure of the photon incorporating its  $P^2$  dependence all give predictions of the  $\sigma_{res}/\sigma_{dir}$  that show the same general trend as the corrected data (see figure 8.1). It is clear, however, that it is not possible to comment on the relative validity of these parametrizations based upon the results presented in this thesis. Future measurements by both the H1 and ZEUS collaborations will hopefully distinguish among different treatments of the  $P^2$  evolution of the structure of the photon.

# Appendix A

## Contribution to Brussels EPS Conference

Paper published in the Proceedings of the International Europhysics Conference on High Energy Physics held in Brussels, 27.7.95 - 2.8.95, eds J. Lemonne, C.

Van der Velde, F. Verbeure, p. 570.

### **Direct and resolved photoproduction at HERA with virtual and quasi-real photons**

M.L. Utley

Department of Physics and Astronomy, University of Glasgow, Glasgow,  
G12 8QQ, United Kingdom

on behalf of the ZEUS collaboration

(The results presented here are those of a parallel and independent study of the data performed by Costas Foudas of the University of Wisconsin)

### **A.1 Abstract**

Preliminary results are presented from a study of dijet photoproduction in ep collisions with both virtual and quasi-real photons at the ZEUS detector. Samples

of events with photons of virtuality  $P^2$  in the ranges  $0.1 < P^2 < 0.55 \text{ GeV}^2$  and  $P^2 < 0.02 \text{ GeV}^2$  having two jets of  $E_T^{jet} > 4 \text{ GeV}$  in the final state have been obtained.

For both quasi-real and virtual photons, uncorrected distributions of the quantity  $x_\gamma^{obs}$ , the fraction of the photon momentum manifest in the two highest  $E_T$  jets, are presented. These distributions are sensitive to the relative contributions of the direct and resolved processes. Resolved photon processes are evident in both data sets, with an apparent decrease in the relative contribution from resolved processes as photon virtuality increases.

## A.2 Introduction

Leading order (LO) QCD predicts photon interactions to have a two-component nature. In direct photon processes the whole of the photon takes part in the hard subprocess with a parton from the proton whereas in resolved photon processes, the photon acts as a source of partons and one of these enters the hard subprocess (see Figure A.1). Both LO processes are characterized by having two outgoing partons of large transverse energy. Previous studies of dijet photoproduction at HERA have shown that both classes of process are evident for the case of quasi-real photons (those of negligible virtuality  $P^2$ ) [18]. The parton content of photons is neither well constrained theoretically nor well known experimentally, particularly for photons with small but non-zero virtualities. Various theoretical predictions exist for the behaviour of the photon structure as a function of the photon virtuality [36][53][65]. The general expectation is that the contribution to the dijet cross section of resolved photon processes should decrease relative to the contribution from direct photon processes (*i.e.* that the partonic content of the photon is suppressed) as the virtuality of the photon increases.

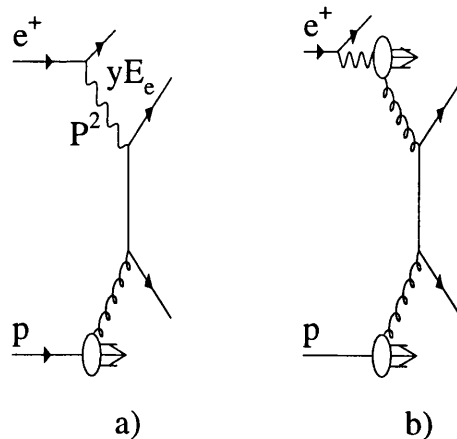


Figure A.1: Diagrams showing a) direct and b) resolved photon processes. In both cases the photon of virtuality  $P^2$  carries a fraction  $y$  of the positron momentum.

### A.3 The Data

The data used in this analysis were collected during the 1994 run when HERA collided 27.5 GeV positrons with 820 GeV protons. The ZEUS detector is described elsewhere[39]. A tungsten-silicon sampling calorimeter was installed for the 1994 running period. This 'beampipe' calorimeter tagged positrons scattered through small angles (17 - 35 mrad) and gave a sample of events with photon virtualities in the range  $0.1 < P^2 < 0.55 \text{ GeV}^2$ . A sample of events with quasi-real photons ( $P^2 < 0.02 \text{ GeV}^2$  with a median of  $10^{-5} \text{ GeV}^2$ ) was obtained by requiring that the scattered positron be detected in the downstream luminosity calorimeter[66]. Jets were found in the main uranium-scintillator[40] calorimeter using a cone algorithm [59] in  $\eta - \phi$  space, where  $\phi$  is azimuth and the pseudo rapidity  $\eta = -\ln(\tan(\theta/2))$ ,  $\theta$  being defined with respect to the proton direction. Only those events with two or more jets of transverse energy  $E_T^{jet} > 4 \text{ GeV}$  in the range  $-1.125 < \eta^{jet} < 1.875$  were selected as dijet events.

To reduce contamination from beam gas and deep inelastic scattering events, a cut of  $0.15 < y_{JB} = \sum(E - p_z)/2E_e < 0.70$  was applied, where the sum is over calorimeter cells with deposits of total and longitudinal energy  $E$  and  $p_z$  respectively and where  $E_e$  is the positron beam energy. In photoproduction,  $y$  is the fraction of the positron energy carried by the photon. These cuts left a sample of 375 events with virtual photons and a sample of 14181 events with quasi-real photons, corresponding to respective integrated luminosities of 2.07 pb<sup>-1</sup> and 2.19 pb<sup>-1</sup>.

## A.4 Results

For each dijet event the fraction of the photon momentum manifest in the two highest  $E_T$  jets,  $x_\gamma^{obs}$  was calculated.  $x_\gamma^{obs}$  is defined by

$$x_\gamma^{obs} = \frac{\sum_{jets} E_T^{jet} e^{-\eta^{jet}}}{2yE_e}$$

We measure  $E_T^{jet}$  and  $\eta^{jet}$  using the raw calorimeter energies and use the Jaquet-Blondel method,  $y_{JB}$  above, to measure  $y$ . No corrections are made for detector effects. Uncorrected distributions of  $x_\gamma^{obs}$  are shown in figure A.2 a) for events with virtual photons and figure A.2 b) for events with quasi-real photons. Events at high  $x_\gamma^{obs}$  are associated with direct photon processes while those at low  $x_\gamma^{obs}$  are associated with resolved photon processes. It is clear that both classes of event are present in both  $P^2$  ranges. To quantify the relative contributions of these classes of event, we have calculated the ratio  $N_{res}/N_{dir}$ , defined as the number of events at low  $x_\gamma^{obs}$  ( $x_\gamma^{obs} < 0.75$ ) divided by the number of events at high  $x_\gamma^{obs}$  ( $x_\gamma^{obs} > 0.75$ ). Figure A.3 shows  $N_{res}/N_{dir}$  as a function of  $P^2$ .  $N_{res}/N_{dir}$  is independent of  $y_{JB}$  for the sample of events with quasi-real photons passing all the cuts applied. This implies that the difference in the  $x_\gamma^{obs}$  distributions for the two samples is not due to the differing  $y_{JB}$  acceptances of the two positron detectors.

The acceptance corrections that will eventually be applied to these data are only weakly dependent on  $x_\gamma^{obs}$  and we therefore expect the corrections to  $N_{res}/N_{dir}$  to be small. More work is required to understand fully these corrections however. In conclusion we find the preliminary result that for events with photons of virtuality  $0.1 < P^2 < 0.55 \text{ GeV}^2$  there is a contribution from resolved photon processes. The size of this contribution relative to that from direct photon processes seems to decrease with increasing photon virtuality.

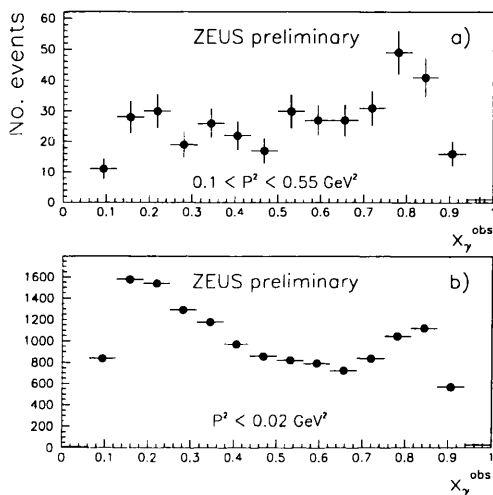


Figure A.2: Uncorrected  $x_\gamma^{obs}$  distributions for a) virtual and b) quasi-real photons

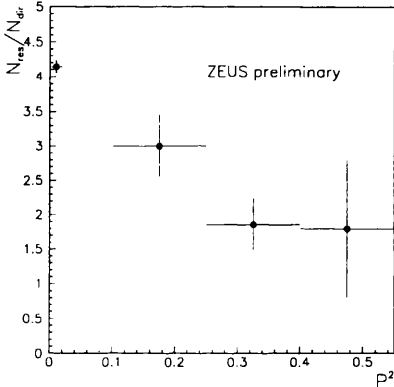


Figure A.3: The uncorrected ratio  $N_{res}/N_{dir}$  as a function of photon virtuality  $P^2$  (GeV<sup>2</sup>)

# Bibliography

- [1] F. Halzen A.D. Martin. *Quarks and Leptons*. John Wiley and Sons, 1984.
- [2] R.E. Taylor H.W. Kendall J.I. Friedman. *Rev. Mod. Phys.* **63**(1991):573.
- [3] ZEUS Collaboration M. Derrick et al. *Phys. Lett.* **B316**(1993):412.
- [4] J.D. Bjorken and E.A Paschos. *Phys. Rev.* **185**(1969):1975.
- [5] A.Martin. *Cont. Phys.* **36**(1995):335.
- [6] J.D. Bjorken. in *Proc. of the Enrico Fermi International School of Physics*, ed J. Steinberger, Course XLI, 1968.
- [7] A.D. Martin R.G. Roberts W.J. Stirling. *Phys. Rev.* **D50**(1994):6734.
- [8] CTEQ Collaboration. *Phys. Lett.* **B304**(1993):159.
- [9] M. Glück E. Reya A. Vogt. *Phys. Lett.* **B306**(1993):391.
- [10] ZEUS Collaboration M.Derrick et al. Measurement of the  $F_2$  Structure Function in Deep Inelastic  $ep$  Scattering using 1994 Data from the ZEUS detector at HERA. *DESY Preprint*, (DESY 96-076), 1996.
- [11] H1 Collaboration T.Ahmed et al. *Nucl. Phys.* **B470**(1996):101.
- [12] Yu. L. Dokshitzer et al. *Basics of Perturbative QCD*. Editions Frontieres, 1991.

- [13] ZEUS Collaboration M. Derrick et al. *Z. Phys.* **C67**(1995):93.
- [14] H1 Collaboration T. Ahmed et al. *Nucl. Phys.* **B445**(1995):3.
- [15] ZEUS Collaboration M. Derrick et al. *Phys. Lett.* **B363**(1995):201.
- [16] ZEUS Collaboration M. Derrick et al. Measurement of Fragmentation Functions in the Breit Frame at HERA. Paper submitted to ICHEP 1996 conference, Warsaw, Poland, July 1996 - ref. no. pa02-034.
- [17] H1 Collaboration T. Ahmed et al. Event Shape Variables in Deep Inelastic Scattering. Paper submitted to ICHEP 1996 conference, Warsaw, Poland, July 1996 - ref. no. pa02-077.
- [18] ZEUS Collaboration M. Derrick et al. *Phys. Lett.* **B322**(1994):287.
- [19] ZEUS Collaboration M. Derrick et al. *Phys. Lett.* **B348**(1995):665.
- [20] ZEUS Collaboration M. Derrick et al. *Phys. Lett.* **B342**(1995):417.
- [21] H1 Collaboration T. Ahmed et al. *Z. Phys.* **C70**(1996):17.
- [22] ZEUS Collaboration M. Derrick et al. Dijet Angular Distributions in Resolved and Direct Photoproduction at HERA. *DESY Preprint*, (DESY 96-094), 1996. accepted by *Phys. Lett.* **B**.
- [23] D.H. Perkins. *Introduction to High Energy Physics*. 4'th edition, Addison-Wesley, 1987.
- [24] V.M. Budnev et al. *Phys. Rep.* **15**(1975):181.
- [25] D.J. Miller. in *Proc of "Two-Photon Physics at LEP and HERA" workshop*, eds G. Jarlskog and L. Jönsson, Lund, Sweden, 1994 ,page 4.
- [26] M. Glück E. Reya A. Vogt. *Phys. Rev.* **D46**(1992):1973.
- [27] H. Abramowicz K. Charchula A. Levy. *Phys. Lett.* **B269**(1991):458.

- [28] L.E. Gordon J.K. Storrow. *Z. Phys.* **C56**(1992):307.
- [29] J.R. Forshaw M.H. Seymour. in *Proc. of Photon '95 - Incorporating the 10'th International Workshop on Gamma-Gamma Collisions and Related Processes* eds D.J. Miller S.L. Cartwright V. Khoze, page 3, 1995.
- [30] A. Vogt. in *Proc of "Two-Photon Physics at LEP and HERA" workshop*, eds G. Jarlskog and L. Jönnsen, Lund, Sweden, 1994 ,page 141.
- [31] M. Drees and R.M. Godbole. Resolved Photon Processes. *University of Wisconsin preprint series*, (MADPH-95-898, hep-ph/9508221), 1995.
- [32] J.J. Sakurai. *Ann. Phys.* **11**(1960):1.
- [33] E. Witten. *Nucl. Phys.* **B120**(1977):189.
- [34] F. Kapusta J.H. Field L. Poggioli. *DESY Preprint*, (DESY 86-046), 1986.
- [35] PLUTO Collaboration Ch. Berger et al. *Phys. Lett.* **B142**(1984):119.
- [36] M. Drees R.M. Godbole. *Phys. Rev.* **D50**(1994):3124.
- [37] G.A. Schuler T. Sjöstrand. Parton Distributions of the Virtual Photon. *CERN Preprint*, (CERN-TH/96-04 hep-ph/9601282), 1996.
- [38] M. Glück E. Reya M. Stratmann. Probing the parton densities of virtual photons at ep colliders. *Dortmund Preprint*, (DO-TH 96/08, hep-ph/9605297), 1996.
- [39] ZEUS Collaboration. *The ZEUS Detector Status Report 1993*, February 1993.
- [40] M. Derrick et al. *Nucl. Inst. and Meth.* **A309**(1991):77.
- [41] R. Fernow. *Introduction to Experimental Particle Physics*. Cambridge University Press, 1989.

- [42] ZEUS Collaboration. *The ZEUS Detector Status Report 1989*, March 1989.
- [43] M. Löewe. The hard- and software of the beampipe calorimeter. *Internal ZEUS Note*, (ZEUS-Note 94-32), 1994.
- [44] Boris Dolgoshein. *Nucl. Inst. and Meth.* **A326**(1993):434.
- [45] D. Haun. PhD thesis, University of Bonn, 1993.
- [46] F. Sauli. Principles of operation of multiwire proportional and drift chambers. *CERN Report*, (CERN 77-09), 1977.
- [47] C.F. von Weizsäcker. *Z. Phys.***88**(1934):612.
- [48] T. Sjöstrand. *Computer Physics Commun.***82**(1994):74.
- [49] T. Sjöstrand. private communication.
- [50] G. Marchesini et al. *Computer Physics Commun.***67**(1992):465.
- [51] B. Andersson et al. *Phys. Rep.***97**(1983):33.
- [52] B.R. Webber. *Nucl. Phys.***B238**(1984):492.
- [53] T. Uematsu T. Walsh. *Phys. Lett.* **B101**(1981):263.
- [54] D. de Florian C. García Canal R. Sassot. Photoproduction of jets and the virtual structure of the photon. *CERN Preprint*, (CERN-TH/96-234, hep-ph/9608438), 1996.
- [55] H1 Collaboration T. Ahmed et al. *Nucl. Phys.* **B445**(1995):195.
- [56] M. Drees. private communication to C. Foudas.
- [57] S. de Jong. PhD thesis, University of Amsterdam, 1990.
- [58] P.J. Bussey. EUCELL - cone based jet finding algorithm. Phantom Program Library - Internal to ZEUS.

- [59] J. Huth et al. in *Proc. of the 1990 DRPF Summer Study on High Energy Physics*, ed E. L. Berger, page 132, 1992.
- [60] J.M. Butterworth et al. Measurement of Dijet Cross Sections in Photoproduction at Hera. *Internal ZEUS note*, (ZEUS-Note 95-010), 1995.
- [61] M.L. Utley. in *Proc. of the International Europhysics Conference on High Energy Physics, Brussels, Belgium*, eds J. Lemonne C. Vander Velde F. Verbeure, page 570, 1995. included as appendix A.
- [62] D. de Florian. private communication.
- [63] K. Hagiwara et al. *KEK Preprint*, (KEK 93-160), 1994.
- [64] A. Caldwell et al. On the New Beam Pipe Calorimeter. *Internal ZEUS Note*, (ZEUS-Note 94-129), 1994.
- [65] F. Borzumati and G. Schuler. *Z. Phys.* **C58**(1993):139.
- [66] J. Andrusków. *DESY Preprint*, (DESY 92-066), 1992.